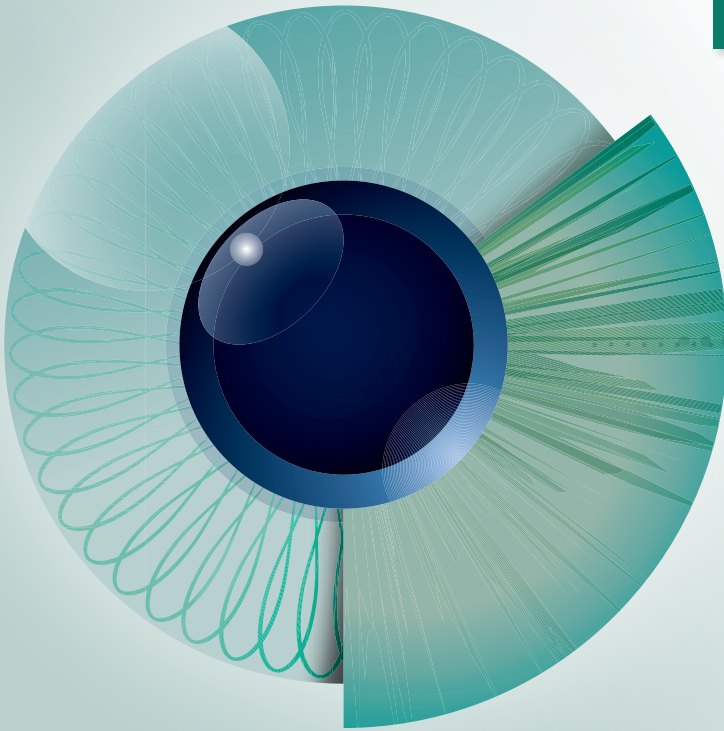
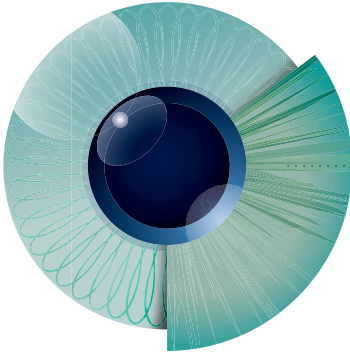


Issue 1-3



Journal for Modeling in Ophthalmology





JMO

Journal for
Modeling in
Ophthalmology

Journal for Modeling in Ophthalmology (JMO) was created in 2014 with the aim of providing a forum for interdisciplinary approaches integrating mathematical and computational modeling techniques to address open problems in ophthalmology.

The Editorial Board members include experts in ophthalmology, physiology, mathematics, and engineering, and strive to ensure the highest scientific level of the contributions selected for publication. JMO aims to be the voice for this rapidly growing interdisciplinary research and we hope you will join us on this exciting journey.

JMO welcomes articles that use modeling techniques to investigate questions related to the anatomy, physiology, and function of the eye in health and disease.

For further information on JMO's focus and scope as well as manuscript submissions:

www.modeling-ophthalmology.com
info@modeling-ophthalmology.com

Copyright

Authors who publish in JMO agree to the following terms:
a. Authors retain copyright and grant the journal JMO right of first publication, with the work twelve (12) months after publication simultaneously licensed under a Creative Commons Attribution License that allows others to share the work with an acknowledgement of the work's authorship and initial publication in JMO.

Chief editors

Alon Harris
Giovanna Guidoboni

Managing editor

Giovanna Guidoboni

Editorial board

Makoto Araie
Fabio Benfenati
Richard J. Braun
Thomas Ciulla
Vital Paulino Costa
Ahmed Elsheikh
Jean-Frederic Gerbeau
Rafael Grytz
Michaël Girard
Gabor Hollo
Ingrida Januleviciene
Jost Jonas
Larry Kagemann
Fabian Lerner
Anat Loewenstein
Toru Nakazawa
Colm O'Brien
Anna Pandolfi
Peter Pinsky
Rodolfo Repetto
Riccardo Sacco
Einar Stefansson
Fotis Topouzis
Emanuele Trucco
Zoran Vatauvuk
Joanna Wierzbowska

Publisher

Kugler Publications
P.O. Box 20538
1001 NM Amsterdam
The Netherlands
info@kuglerpublications.com
www.kuglerpublications.com

ISSN

Online: 2468-3930

Print: 2468-3922

Manuscript submissions

Author guidelines and templates are available via the website, through which all manuscripts should be submitted. For inquiries please contact us via e-mail.

Publication frequency

JMO is published four issues per year (quarterly) electronically. A selection is published in print twice a year and distributed free of charge at congresses through Kugler Publications or partners.

Advertising inquiries

JMO offers online and in print sponsorship and advertising opportunities. Please contact Kugler Publications to for inquiries.

b. After 12 months from the date of publication, authors are able to enter into separate, additional contractual arrangements for the non-exclusive distribution of JMO's published version of the work, with an acknowledgement of its initial publication in JMO.

Open access policy

The first volume of JMO is fully open access (after registration) without requiring any publication fee from the authors. However, we are currently evaluating various models to cover the publications costs while keeping knowledge as accessible as possible, which remains our first priority. Possible models include subscription fees, publication fees, and advertisement venues, or a combination. Please share your thoughts with us on this hot topic via e-mail.

Disclaimers

All articles published, including editorials and letters, represent the opinions of the authors and do not reflect the official policy of JMO, its sponsors, the publisher or the institution with which the author is affiliated, unless this is clearly specified. Although every effort has been made to ensure the technical accuracy of the contents of JMO, no responsibility for errors or omissions is accepted. JMO and the publisher do not endorse or guarantee, directly or indirectly, the quality or efficacy of any product or service described the advertisements or other material that is commercial in nature in any issue. All advertising is expected to conform to ethical and medical standards. No responsibility is assumed by JMO or the publisher for any injury and/or damage to persons or property as a matter of products liability, negligence or otherwise, or from any use or operation of any methods, products, instructions, or ideas contained in the material herein. Because of rapid advances in the medical sciences, independent verification of diagnoses and drug dosages should be made.



Table of contents

Editorial 4

Diya Yang, Ningli Wang

Original article

Electrophysiological evaluation in normal-tension glaucoma suspects: a pilot study 9

Dario Messenio, Giuseppe Marano, Elia Biganzoli

Equilibrium shape of the aqueous humor-vitreous substitute interface in vitrectomized eyes 31

Krystyna Isakova, Jan O. Pralits, Mario R. Romano, Jan-Willem M. Beenakker, Denis P. Shamonin, Rodolfo Repetto

Correlation and agreement between the 24-hour diurnal tension curve, the water-drinking test, and the postural-change test in glaucoma patients 47

Fauze A. Goncalves, Fernando Henrique R. Amorim, Camila S. Zangalli, José Paulo C. Vasconcellos, Vital P. Costa

Blink characterization using curve fitting and clustering algorithms 60

Joseph K. Brosh, ZiweiWu, Carolyn G. Begley, Tobin A. Driscoll, Richard J. Braun

Selective fusion of structural and functional data for improved glaucoma detection 82

Paul Y. Kim, Khan M. Iftekharuddin, Pinakin G. Davey, Martha Tóth, Anita Garas, Gabor Holló, Edward A. Essock

An imaged-based inverse finite element method to determine in-vivo mechanical properties of the human trabecular meshwork 100

Anup D. Pant, Larry Kagemann, Joel S. Schuman, Ian A. Sigal, Rouzbeh Amini

Cerebrospinal fluid pressure and glaucoma

Diya Yang^{1,2}, Ningli Wang^{1,2}

¹Beijing Tongren Eye Center, Beijing Tongren Hospital, Capital Medical University, Beijing Ophthalmology and Visual Sciences Key Laboratory, Beijing, China; ²Beijing Institute of Ophthalmology, Beijing Tongren Hospital, Capital Medical University, Beijing, China

The relationship between cerebrospinal fluid pressure (CSF-P) and glaucoma has aroused great interest in recent years. Before this development, elevated intraocular pressure (IOP) had long been considered as the major risk factor for the development and progression of glaucomatous optic nerve damage.¹ However, numerous studies have shown that there is a relatively large number of patients with typical glaucomatous optic neuropathy (normal-tension glaucoma, NTG) in whom IOP measurements have always been in the normal range (<21mmHg).² Thus, several questions arise. Why do NTG patients develop glaucoma in the absence of high IOP? Are factors other than IOP contributing to the pathogenesis of NTG?

As early as the 1970s, Volkov³ pointed out that CSF-P could be a counter-pressure to IOP as well as pathogenically associated with glaucomatous optic neuropathy. In a similar manner, Yablonsky *et al.*⁴ postulated that an abnormally low CSF-P around the optic nerve could be the reason for barotraumatically-induced optic nerve damage in primary open-angle glaucoma (POAG) with normal IOP. However, it was not until recently that retrospective studies by Berdahl *et al.*^{5,6} and prospective studies by us^{7,8} both found that CSF-P is lower in POAG patients. Moreover, the CSF-P data in POAG with normal IOP from another study done by Jaggi *et al.*⁹ also reviewed a lower CSF-P.

Although the studies mentioned above providing evidence of low CSF-P in NTG seemingly resolved the better part of the IOP dilemma, the following questions remain:

Correspondence: Ningli Wang, Beijing Tongren Eye Center, Beijing Tongren Hospital, Capital Medical University, Beijing Ophthalmology and Visual Sciences Key Laboratory, No. 1 Dongjiaominxiang Street, Dongcheng District, Beijing, China.
E-mail: wningli@vip.163.com

1. Although lumbar CSF-P is low in NTG patients, is their optic nerve subarachnoid space CSF-P low?

The assessment of CSF-P in clinical studies was based on single lumbar CSF-P measurements, but not on a measurement of the CSF-P in the subarachnoid space (SAS) of the optic nerve. Whether lumbar CSF-P can represent CSF-P in the optic nerve SAS remains unknown. Since a direct measurement of orbital CSF-P is invasive and not acceptable in clinical practice, a 3T-MRI-based imaging technology was developed to measure optic nerve SAS width as a surrogate for optic nerve subarachnoid CSF-P. A study of 39 POAG patients, in which 21 patients had normal pressure (IOP < 21 mmHg), 18 patients had high pressure (IOP > 21 mmHg), and 21 subjects comprised the control group, found that optic nerve SAS width was significantly narrower in the normal-pressure group than in the high-pressure group or the control group.¹⁰ This result demonstrated that patients with glaucomatous optic nerve damage and normal IOP had an abnormally narrow subarachnoid CSF space around the post-laminar optic nerve suggesting a low CSF-P or, as a corollary, a high trans-laminar cribrosa pressure difference (TLPD).

In addition to the clinical evidence, it remains important to illustrate the relationship among lumbar CSF-P (LCP), brain CSF-P (ICP), and optic nerve subarachnoid CSF-P (ONSP). Eight dogs were used to measure these pressures simultaneously. The results found that the pressures were different with $ICP > LCP > ONSP$, but correlated with each other ($P < 0.001$). The trans-lamina cribrosa pressure gradient (TLPG) was highest for IOP-ONSP, lower for IOP-LCP, and lowest for IOP-ICP ($P < 0.001$). During CSF shunting, ICP gradually decreased in a linear fashion together with ONSP (“ICP-dependent zone”). However, when ICP fell below a critical breakpoint, ICP and ONSP became uncoupled and ONSP remained constant despite further ICP decline (“ICP-independent zone”).¹¹ We interpret this as a sign of CSF communication arrest between the intracranial and optic nerve SAS. This may be caused by obstructions of either CSF inflow through the optic canal or outflow into the intra-orbital cavity.

2. Can low CSF-P induce glaucomatous optic neuropathy?

Yang *et al.*¹² conducted an experimental investigation in monkeys to further explore the potential association between an abnormally low CSF-P and glaucomatous optic nerve damage. Four monkeys received a lumbar-peritoneal shunt to reduce CSF-P, while five control monkeys underwent the same procedure but with the shunt remaining closed. Follow-up examinations included regular measurements of IOP and CSF-P, confocal laser scanning tomography of the optic nerve head and retinal nerve fiber layer, and fundus photography. Four eyes of two study-group monkeys developed a continuous loss of retinal nerve fiber layer, and one eye of a third monkey showed a splinter-like disc hemorrhage during the follow-up. The

other three eyes in the study group and all eyes of the monkeys in the control group remained unchanged. It was concluded that the chronic reduction of CSF-P led to optic nerve damage in some monkeys with experimental and chronic reduction in CSF-P. Whether optic nerve damage corresponded to glaucoma remained unclear.

3. Can we measure CSF-P for glaucoma patients clinically?

In the context of an increased TLPD in the pathogenesis of POAG, one may infer that the diagnostic and therapeutic pattern for POAG patients may be changed. Therefore, it seems essential to examine TLPD in POAG patients. However, lumbar puncture for POAG patients is currently controversial and not applicable in a clinical setting. Although some non-invasive ways of measuring ICP have been developed, the accuracy and efficacy of these methods remains dim. More importantly, orbital CSF-P is the key to TLPD, but ethical concerns regarding the invasiveness of the procedure required for direct measurement has stopped us from conducting this type of research. Finding a non-invasive way to measure orbital CSF-P seems essential and applicable.

Based on 3.0T MRI, the Intracranial and Intraocular Pressure Study Group (iCOP) developed an algorithm for a non-invasive measurement of intracranial CSF-P with MRI-assisted optic nerve SAS measuring with intraclass correlation coefficients (ICCs) of 0.87.¹³ Subsequently, an easier formula to estimate CSF-P without measuring optic nerve SAS was established by means of multivariate analysis ($\text{CSF-P [mmHg]} = 0.44 \times \text{BMI [kg/m}^2] + 0.16 \times \text{Diastolic Blood Pressure [mmHg]} - 0.18 \times \text{Age [Years]} - 1.91$). It confirmed previous investigations that had also reported on associations between higher BMI and higher CSF-P.^{14,15} Applying the formula in an independent test group revealed that the measured CSF-P (12.6 ± 4.8 mmHg) did not differ significantly ($P=0.29$) from the calculated CSF-P (13.3 ± 3.2 mmHg). We then applied this formula to the population-based Beijing Eye Study, which included 3468 individuals, and Central India Eye and Medical Study, which included 4711 individuals; the results showed that in POAG, but not in angle-closure glaucoma, calculated TLPD versus IOP showed a better association with glaucoma presence and amount of glaucomatous optic neuropathy.^{16,17} These results support the notion of the potential role of low CSF-P in the pathogenesis of POAG.

TLPD imbalance may play an important role in the pathogenesis of glaucomatous optic nerve damage. Mathematical model research is vital and must be continued to elucidate the downstream mechanisms of increased TLPD in glaucomatous optic neuropathy. Given that a rational and precise procedure for diagnosing and managing POAG based on TLPD is not currently applicable, obstacles and problems should be conquered and intensive investigations should be continuous. Clinically, IOP reduction still seems the most applicable way of decreasing TLPD and treating POAG patients. It may be of interest to find a way to increase CSF-P non-invasively.

Moreover, it is also important to estimate the target TLPD, which may be more reasonable than IOP alone.

References

1. Leske MC, Heijl A, Hussein M, et al. Factors for glaucoma progression and the effect of treatment: the Early Manifest Glaucoma Trial. *Arch Ophthalmol* 2003;121(1):48-56. Available from: <http://archophth.jamanetwork.com/article.aspx?doi=10.1001/archophth.121.1.48> doi: 10.1001/archophth.121.1.48.
2. Drance SM. Some factors in the production of low tension glaucoma. *British Journal of Ophthalmology* 1972 Mar;56(3):229-242. Available from: <http://bj.o.bmj.com/cgi/doi/10.1136/bjo.56.3.229> doi: 10.1136/bjo.56.3.229.
3. Volkov VV. Essential element of the glaucomatous process neglected in clinical practice [in Russian]. *Oftalmol Zh* 1976;31:500.
4. Yablonski M, Ritch R, Pokorny KS. Effect of decreased intracranial pressure on optic disc. *Invest Ophthalmol Vis Sci* 1979;18[Suppl]:165
5. Berdahl JP, Allingham RR, Johnson DH. Cerebrospinal fluid pressure is decreased in primary open-angle glaucoma. *Ophthalmology* 2008;115(5):763-8. Available from: <http://linkinghub.elsevier.com/retrieve/pii/S016164200800064X> doi: 10.1016/j.ophtha.2008.01.013.
6. Berdahl JP, Fautsch MP, Stinnett SS, Allingham RR. Intracranial pressure in primary open angle glaucoma, normal tension glaucoma, and ocular hypertension: a case-control study. *Invest Ophthalmol Vis Sci* 2008;49(12):5412-8. Available from: <http://iovs.arvojournals.org/article.aspx?doi=10.1167/iovs.08-2228> doi: 10.1167/iovs.08-2228.
7. Ren R, Jonas JB, Tian G, et al. Cerebrospinal fluid pressure in glaucoma. A prospective study. *Ophthalmology* 2010;117(2):259-66. Available from: <http://linkinghub.elsevier.com/retrieve/pii/S0161642009007337> doi: 10.1016/j.ophtha.2009.06.058.
8. Ren R, Zhang X, Wang N, Li B, Tian G, Jonas JB. Cerebrospinal fluid pressure in ocular hypertension. *Acta Ophthalmol*:2011-89.
9. Jaggi GP, Miller NR, Flammer J, Weinreb RN, Remonda L, Killer HE. Optic nerve sheath diameter in normal-tension glaucoma patients. *Br J Ophthalmol* 2011 Mar;11.
10. Wang NL, Xie XB, Yang DY, et al. "Orbital Cerebrospinal Fluid Space in Glaucoma: The Beijing iCOP Study". *Ophthalmology* 2012;119(10):2065-2073. Available from: <http://linkinghub.elsevier.com/retrieve/pii/S0161642012003223> doi: 10.1016/j.ophtha.2012.03.054.
11. Hou R, Zhang Z, Yang D, Wang H, Chen W, Li Z, et al. . Intracranial pressure (ICP) and optic nerve subarachnoid space pressure (ONSP) correlation in the optic nerve chamber: the Beijing Intracranial and Intraocular Pressure (iCOP) study. *Brain Res*. 2016 Mar 15; 1635.
12. Yang D, Fu J, Hou R, Liu K, Jonas JB, Wang H, et al. Optic neuropathy induced by experimentally reduced cerebrospinal fluid pressure in monkeys. *Invest Ophthalmol Vis Sci* 2014 Apr;55(5):3067-73. Available from: <http://iovs.arvojournals.org/article.aspx?doi=10.1167/iovs.13-13657> doi: 10.1167/iovs.13-13657.
13. Xie X, Zhang X, Fu J. Noninvasive intracranial pressure estimation by orbital subarachnoid space measurement: the Beijing Intracranial and Intraocular Pressure (iCOP) study[J. *Critical Care*;2013(17).
14. Berdahl JP, Fleischman D, Zaydlarova J, Stinnett S, Allingham RR, et al. Body mass index has a linear relationship with cerebrospinal fluid pressure. *Invest Ophthalmol Vis Sci* 2012;53(3):1422. Available from: <http://iovs.arvojournals.org/article.aspx?doi=10.1167/iovs.11-8220> doi: 10.1167/iovs.11-8220.
15. Ren R, Wang N, Zhang X, Tian G, Jonas JB. Cerebrospinal fluid pressure correlated with body mass index. *Graefes Arch Clin Exp Ophthalmol* 2012;250(3):445-446. Available from: <http://link.springer.com/10.1007/s00417-011-1746-1> doi: 10.1007/s00417-011-1746-1.

16. Jonas JB, Wang N, Wang YX, You QS, Xie X, Yang D, Xu L. Body height, estimated cerebrospinal fluid pressure and open-angle glaucoma. The Beijing Eye Study 2011. *PloS one*. 2014 Jan 29;9(1):e86678.
17. Jonas JB, Nangia V, Wang N, Bhate K, Nangia P, Nangia P, Yang D, Xie X, Panda-Jonas S. Trans-lamina cribrosa pressure difference and open-angle glaucoma. The central India eye and medical study. *PloS one*. 2013 Dec 6;8(12):e82284.



Electrophysiological evaluation in normal-tension glaucoma suspects: a pilot study

Dario Messenio¹, Giuseppe Marano², Elia Biganzoli^{2,3}

¹Eye Clinic, Department of Clinical Science, Luigi Sacco Hospital, University of Milan, Milan, Italy; ²Unit of Medical Statistics and Biometry, Fondazione IRCCS Istituto Nazionale dei Tumori, Milan, Italy; ³Department of Clinical Sciences and Community Health, University of Milan, Italy

Abstract

Purpose: To evaluate the variations of intraocular pressure (IOP), morphometric papillary characteristics, perimetric indices, and electrophysiological parameters, *i.e.*, pattern electroretinogram (PERG) and visual evoked potentials (VEPs), before and after topic hypotonization therapy in normal-tension glaucoma (NTG) suspects.

Methods: We evaluated 38 eyes of 20 patients with intraocular pressure of < 21 mmHg (measured with Goldmann applanation tonometry), initial glaucomatous optic neuropathy (assessed with Heidelberg Retina Tomograph (HRT): retinal fiber layer (RNFL) and/or linear cup/disk (linear C/D), minimal visual defects (Octopus 101: G2 program), visual acuity of more than 15/20 with best correction, and pathological electrophysiological parameters (valued with pattern electroretinogram and visual evoked potentials), free of systemic or other ocular diseases. All parameters were evaluated at the beginning of the study (T_0) and after 12 months from the start of the therapy (T_{12}). A randomized normal control group (27 eyes of 14 subjects) with apparent larger disc cupping underwent all exams at the start of the study and after 12 months.

Results: Among electrophysiological parameters, at the beginning of the study P100 VEPs latency was slightly increased and P100 amplitude was reduced in NTG compared to normal subjects, with no significant variation after 12 months. P50 PERG latency was quite similar between the NTG and normal groups, and showed no modification after therapy. Compared to normal subjects, P50N95 complex

Correspondence: Dario Messenio, via Domenichino 49, Milano 20149, Italy.
E-mail: dmessenio@virgilio.it

PERG amplitude in NTG was reduced and showed a slight increase after 12 months (1.8 vs 1.5; 2.4 vs 1.9 microvolts, with different checkerboard spatial frequency). Cortical-retinal time (CRT) was slightly delayed in NTG and showed no modification after therapy. Among visual field indices, mean defect (MD) and corrected loss variance (CLV) were slightly higher in NTG, and showed no significant modification after therapy. Among morphometric optic nerve head characteristics, linear C/D and RNFL thickness were quite similar between the NTG and normal groups, and showed no modification after therapy. IOP was also similar between NTG and normal subjects, and decreased after therapy in the NTG group.

Conclusion: From the perspective of an integrated diagnostic, electrophysiological tests (VEPs and PERG) may provide a more sensitive measure of retinal ganglion cell (RGC) integrity and help to distinguish between normal-tension glaucoma suspects before perimetric alterations are evident, and normal subjects with apparent larger disc cupping.

Keywords: pattern electroretinogram (PERG), visual evoked potentials (VEPs), normal-tension glaucoma (NTG) suspects, minimal visual defects, initial glaucomatous optic neuropathy

A short guide to read electrophysiological parameters

1. Pattern electroretinogram (PERG)

The pattern electroretinogram (PERG) represents an objective and direct measure of retinal ganglion cell (RGC) function. It is a retinal biopotential evoked by a temporally modulated patterned stimulus (checkerboard or grating) of constant mean luminance. The PERG waveform depends on the temporal frequency of the stimulus. At low temporal frequencies (<6 reversals per second (rps), equivalent to 3 Hz), transient PERGs are obtained: the PERG waveform in normal subjects usually consists of a small initial negative component with a peak time (i.e., latency) of 35 msec (N35), followed at 45–60 msec by a much larger positive component (P50), and a large negative component at about 95 msec (N95). In glaucoma analysis, P50N95 complex amplitude (in microvolt) — calculated from P50 peak to N95 peak — and P50 implicit time (or latency) (in msec) are measured with different spatial frequencies: either with checkerboard subtending 30' of arc of visual angle or 15' (smaller).

2. Visual evoked potentials (VEPs)

Visual evoked potentials (VEPs) characterize the state of the whole visual pathway. The waveform of the VEPs evoked by contrast reversal of pattern stimuli depends on the temporal frequency of the stimulus. Considerations

are the same as those for PERG. At low temporal frequencies (< 6 reversals per second (rps), equivalent to 3 Hz), transient VEPs are obtained: VEPs waveforms consist of an initial negative component with a peak time of approximately 75 msec (N75), followed by a larger positive component (P100) at 100-110 msec, and by a large negative component at 120-140 msec (N135). P100 latency (in msec) and amplitude (in micronvolt) are measured with different spatial frequencies: either with checkerboard subtending 30' of arc of visual angle or 15' (smaller).

Cortical-retinal time (CRT) is an electrophysiological index that analyzes neural conduction in post-retinal visual pathways; it is derived from simultaneous recordings of VEPs and PERGs and represents the latency difference between P50 PERG and P100 VEPs.

1. Introduction

Glaucoma is a multifactorial optic neuropathy characterized by progressive loss of retinal ganglion cells (RGC), changes in optic disk morphology, and visual field defects. Intraocular pressure (IOP) is a recognized risk factor for the development and progression of glaucomatous damage: multicenter studies have found that a 1 mmHg reduction decreased the risk of damage progression by 10%, and that conversion from ocular hypertension to manifest glaucoma is decreased by reducing IOP.^{1,2} A particular type of open-angle glaucoma, normal-tension glaucoma (NTG), has a typical glaucomatous optic neuropathy evolution with untreated IOP below 21 mmHg.³⁻⁵ Several population studies have suggested an incidence of NTG between 20% and 40% for all open-angle glaucomas.^{6,7} IOP is recognized as the most important risk factor for the development or progression of glaucomatous damage, even if pressure reduction does not necessarily slow or halt disease progression.^{8,9} In fact, in NTG other IOP-independent factors concur to the progression of the disease, including migraine, disk haemorrhage, occlusive vascular diseases, abnormal ocular blood flow, systemic hypotension, and sleep apnoea,¹⁰⁻¹² even if there still are individual responses between diagnostic exams. Specifically, patients with NTG show a greater reduction in nocturnal blood pressure compared to healthy subjects, which is correlated to a more rapid progression of glaucoma.¹³⁻¹⁵

In addition to damaging RGC, glaucoma can also damage the post-retinal mechanism at the level of the lateral geniculate nucleus (LGN) of the thalamus and the primary visual cortex (V1).¹⁶ Hence, glaucoma can be associated with profound degenerative effects in the visual brain. Studies on experimental glaucoma in primates show neural degeneration of the LGN¹⁷⁻²⁰ and activity changes in the visual cortex.¹⁹ Degeneration of the LGN and visual cortex has also been demonstrated in human glaucoma.¹⁶

Among diagnostic exams for glaucoma, the pattern electroretinogram (PERG) stands as a direct indicator of RGC function.^{21,22} PERG amplitude decreases with increasing age in normal subjects, which may be due to neural loss as well as to reduced retinal illuminance resulting from retinal miosis and reduced image contrast due to cataract or other opacities of optical media; therefore, response must be normalized for age.^{23,24}

PERG reflects ganglion-diffuse rather than focal damage,^{25,26} so correlations between altered PERGs and visual fields are not necessarily found.^{27,28} RGC loss above 30% is associated with statistically significant changes in visual field sensitivity²⁹, so the visual field is not impaired in ocular hypertension or early manifest glaucoma.³⁰ Caprioli identified two distinct types of glaucoma field defects: a more diffuse loss of visual field sensitivity, correlated to IOP, and a less pressure-dependent, localized type. The first type may be due to diffuse dysfunction leading to progressive concentric enlargement of the optic nerve cup; as it is a mass response reflecting diffuse RGC dysfunction, PERG is often impaired in this type of glaucoma.³¹ Caprioli believes that the second type, *i.e.*, glaucoma with focal visual field defects, is more correlated with vascular factors. In this type of glaucoma, PERG may still be normal until the majority of RGC are affected.³²

PERG is altered in glaucoma as well as in many cases of ocular hypertension (OHT).³³⁻³⁶ Several authors who have performed human studies find PERG to be a predictive value to identify those patients with elevated IOP who develop glaucoma before visual field changes occur;³⁷⁻⁴⁰ given that none of the eyes with initially normal PERG develop glaucomatous field defects;⁴¹ moreover Philippin, in a ten-year longitudinal study, found that 8% of eyes develop manifest glaucoma (defined by visual field defect) with high sensitivity and specificity.^{40,42} In experimental glaucoma studies in monkeys, Marx found a reduction of PERG amplitude without evidence of cupping;⁴³ in mice, Saleh and Porciatti show a progressive reduction of inner retina function with retinal fiber layer (RNFL) relatively spared: PERG amplitude reaches the noise level in many eyes when RNFL thickness decreases by 50%.^{44,45}

Some authors have emphasized the correlation between PERG and progress of vertical cup-to-disc ratio,⁴⁶ optic disk RNFL thickness loss measured by optical coherence tomography (OCT),^{47,48} and cup shape measure of the Heidelberg Retina Tomograph (HRT).^{49,50}

PERG has a higher sensibility to detect glaucomatous defects^{39,51,40} and is abnormal in most patients with manifest disease.^{49,52,47,51} PERG impairment always precedes visual field defects.⁵³ As it reflects diffuse ganglion damage, there is a strong correlation between PERG and mean defect (MD) visual field index and a weak correlation with correct pattern standard deviation (CPSD) or corrected loss variance (CLV), both of which analyze local defects.^{48,53} There is no linear relationship between P50N95 amplitude and visual field loss and, in some cases, PERG changes can precede detectable field loss because PERG is particularly sensitive to early damage.⁵⁴

As referred above, PERG reflects the total amount of electrophysiological activity of RGC, *i.e.*, represents an objective and direct measure of RGC function. Analysing the structure-function relationship in experimental and human studies, Marx,⁴⁶ Ventura,⁵⁵ and North⁵⁶ suggested the hypothesis that there may be a stage of reversible dysfunction prior to RGC death. This period of dysfunction may happen long before ganglion cell loss. In glaucoma suspects or in early glaucoma, a reduction in PERG amplitude may be due to early RGC dysfunction. This dysfunction is potentially reversible and may be restored after IOP reduction.⁵⁵ This improvement occurred not only in ocular hypertension (OHT) or hypertensive glaucoma (primary open-angle glaucoma, POAG),⁴⁶ but also in NTG.⁵⁶ Particularly in early glaucoma, after lowering IOP Ventura found a positive change in slope steepness that may indicate that the progressive degradation of RGC function has slowed down.⁵⁷ Compared to POAG, PERG improvements in NTG were associated with smaller reductions of IOP;⁵⁵ perhaps RGC dysfunction in NTG occurs at a lower IOP and, in turn, PERG improvements occur after smaller IOP reductions. However, small improvements in eyes with advanced visual field defects may be explained by fewer quantities of surviving RGC in the advanced stages of NTG.

Visual evoked potentials (VEPs) characterize the state of the whole visual pathway. In glaucomatous patients, there is a delay of P100 latency and/or P100 amplitude reduction.^{58,59,51} Parisi found a high specificity of VEPs in identifying normal subjects.⁵¹ VEPs show reduced amplitude in OHT and manifest glaucoma.⁶⁰ Cortical-retinal time (CRT) is an electrophysiological index that analyzes neural conduction in post-retinal visual pathways; it is derived from simultaneous recordings of VEPs and PERGs⁶¹ and represents the latency difference between P50 PERG and P100 VEPs. Cortical-retinal time is unchanged in OHT, but increases as the disease progresses,⁴⁷ and is correlated with a reduction in PERG amplitude so that signal transmission is progressively slower (revealed by a greater increase of P100 latency). Moreover, there is a correlation with optic nerve fiber thinning, measured by OCT.⁴⁷ VEPs reflect the activity of the later stages in the visual processing chain, and are less affected by glaucoma than PERG.

In this study, we tested the hypothesis that electrophysiological dysfunctions are present in NTG suspects with early structural damage and no perimetric defect. Additionally, any structural or functional variations were assessed twelve months after starting therapy.

2. Methods

The study was approved by the Hospital Medical Ethics Committee, and informed consent was obtained from the subjects following an explanation of the nature and possible consequences of the study. Healthy control subjects and early-stage glaucoma patients were recruited at the Sacco Hospital eye clinic in Milan, Italy.

2.1. Patients with suspected NTG

Twenty subjects (38 eyes) with suspected normal-tension glaucoma were recruited. All patients underwent a complete clinical examination including best-corrected visual acuity, Goldmann applanation tonometry, optic nerve head assessment by slit lamp binocular indirect ophthalmoscopy, scanning laser tomography (Heidelberg Retina Tomograph (HRT), Germany), perimetry (Octopus 101: G2 program for glaucoma; Interzeag, Schlieren, Switzerland), VEPs and PERG recording (Biomedica Mangoni, Pisa, Italy).

Inclusion criteria were:

1. visual acuity of more than 15/20 with best correction;
2. untreated IOP (measured with Goldmann applanation tonometry) on a diurnal pressure curve inferior to 21 mmHg;
3. initial glaucomatous optic neuropathy evaluated with HRT in conjunction with the following inclusion criteria: 1) one sector measurement labelled “borderline” or “outside of normal” at Moorfield Regression Analysis; 2) retinal nerve fibre layer (RNFL) less than 200; 3) linear cup-disk (linear C/D) more than 600;
4. alteration of electrophysiological parameters, namely, decreased P50N95 PERG complex amplitude or/and decreased VEPs P100 wave amplitude. Values differing by less than two standard deviations from the correct normative value for age were considered non-pathological;
5. visual field indices: mean defect (MD) and correct loss variance (CLV), considering values “borderline” or “1st Stage” according to Glaucoma Staging System 2 perimetric stadiation.^{62,63}

Exclusion criteria were:

1. history of refractive surgery;
2. high myopia;
3. other ocular or systemic diseases;
4. patients already in therapy or with other ocular or systemic diseases.

2.2. Healthy subjects

An age-matched control group of 14 healthy subjects (27 eyes) with the same morphological alterations (RNFL less than 200 and linear cup-disk (linear C/D) more than 600) but normal PERG, VEPs, and visual field indices; no ophthalmic diseases and no family history of glaucoma.

We analyzed these two groups at the start of the study (T_0) and after 12 months (T_{12}). Glaucomatous patients underwent hypotonizing therapy with prostaglandin eye drops, one drop a day; the controls did not undergo therapy.

2.3. Electroretinography

Electrophysiological tests (VEPs and PERG) were recorded monocularly and simultaneously.

2.4. PERG technique

A small silver chloride skin (active and reference) electrode was positioned on the lower eyelids. A skin electrode at the midfrontal position (in Fpz scalp) served as ground. PERG were recorded simultaneously with VEPs, with 30-minute and 15-minute black-and-white checkerboard pattern stimulus, 45 cd/m² mean luminance, reversing two times per second (square wave reversal) or counter phased at 1 Hz (thus evoking transient responses) at 98% contrast between black-and-white squares. Signals were amplified (50000 times) and filtered (pass band 1-100 Hz). The stimuli were generated on a cathode-ray tube monitor subtending 24° at a viewing distance of 114 cm.

At low temporal frequencies (< 6 rps), transient PERGs were obtained. The PERG waveform consists of a small initial negative component with a peak time of approximately 35 ms (N35), followed at 45-60 ms by a larger positive component (P50). The following wave is a large negative component at 90-100 ms (N95). P50 peak time (or latency) and P50N95 complex amplitude (*i.e.*, from the peak of P50 to the peak of N95) were measured.

2.5. Visual evoked potentials (VEPs) technique

The scalp electrodes were placed according to the International 10/20 System. The active electrode was placed on the scalp over the visual cortex at Oz with the reference electrode at Fz. A skin electrode at the midfrontal position (in Fpz scalp) served as ground electrode.

VEPs were recorded simultaneously with PERG, with 30-minute and 15-minute black-and-white checkerboard pattern stimulus with 45 cd/m² mean luminance, reversing two times per second (square wave reversal) or counter phased at 1 Hz (thus evoking transient responses) at 98% contrast between black and white squares. Signals were amplified (50000 times) and filtered (pass band 1-100 Hz). The stimuli were generated on a cathode-ray tube monitor subtending 24° at a viewing distance of 114 cm.

At low temporal frequencies (< 6 rps), the pattern-reversal VEP waveform consists of N75, P100, and N135 peaks. P100 peak time (or latency) and P100 amplitude were measured.

2.6. Perimetry and visual field criteria

Octopus 101: G2 program for glaucoma; Interzeag, Schlieren, Switzerland
Glaucoma Staging System 2 (GSS2) perimetric stadiation was used, which considers visual field defects by analyzing perimetric indices: MD and CLV.^{62,63} We included in this study no defect or initial defects: “borderline” (MD between 2,5 and 3; CLV between 3 and 4) or “1st stage” (MD between 3 and 6; CLV between 4 and 6) in two consecutive visual fields.^{62,63}

2.7. HRT technique

The HRT is a confocal scanning laser imaging device for the analysis of glaucomatous optic disk topography.^{64,65} With Moorfield Regression Analysis (MRA) for each sector of the optic nerve head (ONH), patients were included with at least a “borderline” global rim area, *i.e.*, at least one measure outside the norm between 95% and 99% confidence interval (CI), linear cup disc (linear C/D) more than 0.55, and mean retinal nerve fiber layer thickness (RNFL thickness) less than 200.⁶⁶

2.8. Statistics

The main aim of the statistical analysis was to describe and quantify the diagnostic parameters for two groups, NTG suspects and healthy subjects, respectively. The analysis was performed on a sample of 38 eyes of patients ($n = 20$) with suspected NTG, and 27 eyes of healthy subjects ($n = 14$). For each eye, the following variables were available, both at T_0 (start of the study) and T_{12} (twelve months later), except for pachymetry, which was recorded only at T_0 :

1. electrophysiological measurements: latency and amplitude of the P50 PERG wave and P100 VEP wave, with 30-minutes and 15-minutes checkerboard pattern stimulus;
2. visual field indices: mean defect (MD), correct loss variance (CLV);
3. morphometric parameters: RNFL thickness, linear C/D;
4. intraocular pressure (IOP);
5. pachymetry.

Furthermore, CRT was defined as the difference between P100 VEPs wave latency and P50 PERG wave latency.

The variables above were summarized using means and standard deviations. A multivariate descriptive analysis was performed, using principal component analysis (PCA) methods,⁶⁷ in order to identify possible patterns of electrophysiological measurements and other parameters in the two groups (NTG and healthy subjects), and to evaluate the correlation among such features. A brief sketch of such methods is reported in the following box.

The strategy of analysis was the following one:

1. In a preliminary step, the assumption of linear correlation among the variables under examination was checked by examining correlation coefficients (Pearson's r and Spearman's ρ) and scatterplots for each couple of variables.
2. Two separate PCAs were performed, for electrophysiological measurements and the remaining variables, respectively. In each one, measurements at T_0 of each variable were used as active variables. This allowed to focus attention on the relationships among the elements that could be potentially used for an early diagnosis. The association among measurements at T_0 and T_{12} was evaluated by including the latter ones in the PCA as supplementary variables. The number of relevant principal components was determined

by examining the scree-plot. Both variables and individuals (*i.e.*, eyes) were represented through principal component biplots.⁶⁸

A further aim was to estimate the average values of the measurements of all the variables and respective differences:

1. between eyes of NTG patients and healthy subjects, at T_0 and T_{12} ;
2. between T_{12} and T_0 for each of the two groups.

To such end, the standard statistical methods based on the assumption of independent and identically distributed (i.i.d.) observations were not adequate. In fact, the i.i.d. assumption was violated by the presence of both repeated measurements for each eye and the correlation between measurements of fellow eyes. Therefore, the estimates were obtained by mixed effects ANOVA methods.⁶⁹ In each ANOVA model:

1. each variable was included as a response variable;
2. the time of measurement (start of study; 12 months later) and group (NTG; healthy) were included as categorical predictors, with both simple effects and interaction effect;
3. to account for the above-mentioned sources of correlation, two random effects, corresponding to subjects and eyes, respectively, were also included.

The results were reported in terms of estimated averages with respective 95% CI. The CI for the four differences indicated above were corrected with the Bonferroni rule.

The statistical analysis was performed using the r software⁷⁰ with additional nlme⁷¹ and multcomp⁷² packages.

Principal component analysis: brief methodological notes

PCA belongs to a wide class of statistical analyses targeted at describing the main features of the distribution of a large set of inter-related variables by reducing the dimensionality of the data. In PCA, this reduction is achieved by transforming the variables into a new set of variables, called principal components, which are ordered in such a way that the first few — most frequently the first one or two — retain most of the variation present in all the original variables. Thus, the principal components may synthesize the main patterns of correlation among the original variables (as measured by the linear correlation coefficient, Pearson's r) and, according to such patterns, identify groups (clusters) of subjects provided of the homogeneous features of the original variables.

PCA techniques allow to plot all the original variables and/or individuals within a few plots, thus giving a straightforward visual representation of the features under examination. Usually, variables are represented by vectors, and individuals by points. The interpretation of the plots follows conventional rules

based on the relative positions among such elements:

1. For each couple of variables: if the corresponding vectors point in the same direction (the angle is close to 0 degrees), the variables are positively correlated. If two vectors point in opposite directions (the angle is close to 180 degrees), the variables are negatively correlated. If two vectors are orthogonal (the angle is close to 90 degrees), there is a low correlation between the variables.
2. For each couple of individuals, the distance between the corresponding points indicates their similarity: a short distance indicates individuals with comparable values of the original variables, whereas a long distance indicates 'heterogeneous' individuals.
3. For each point (individual), the patterns of the original variable are derived by projecting the point onto the vectors. Considering each vector as an axis, the distances between the origin and the projections of the points indicate the magnitude of the corresponding variables.

For further details, see the cited monography by Jolliffe.⁶⁷

3. Results

Means and standard deviations of the variables of interest are reported in Table 1. In the multivariate analysis, no complex, *i.e.*, non-linear relationship emerged from the examination of correlation coefficients and scatterplots. In the first PCA (electrophysiological characteristics), according to the scree-plot the first principal component provides an adequate synthesis of the variables under examination. The proportion of total variability of data explained by the first principal component is 48.6%. The patterns emerging from the biplot (Fig. 1a) are quite clear:

1. A global positive correlation emerged among measurements of P100 VEP and P50 PERG amplitudes at T_0 (the vectors corresponding to such variables are overall directed toward the same direction) of moderate or moderate/high amount. In agreement with this, the values of Pearson's index of correlation (Pearson's r) vary from 0.46 to 0.88.
2. Similarly, a positive correlation emerged among latency measurements at T_0 , more pronounced between the two measurements of the P100 VEP wave ($r = 0.83$), whereas the correlation of the latency of the P50 PERG wave with 30-minutes checkerboard pattern (P50/30') with the other variables is low (r ranging from 0.13 to 0.23) (the angles between the vector corresponding to P50/30' and the vectors representing the other variables are overall nearly 90°).

Table 1. Descriptive synthesis of diagnostic parameters

Data were reported as mean and standard deviations. NTG = eyes of patients with suspected normal tension glaucoma; Healthy = eyes of healthy subjects. Electrophysiological parameters: L100 and L50 = latency of P100 VEP and P50 PERG waves, respectively; A100 and A50 = amplitude of P100 VEP and P50N95 complex PERG waves, respectively. Text: /15' and /30' indicate measurements taken with 15-minutes and 30-minutes checkerboard pattern stimulus, respectively. Visual field indices: MD = mean defect; CLV = correct loss variance. Morphometric parameters: RNFL = RNFL thickness; Lin.C/D = linear C/D. IOP = intraocular pressure. PAC = pachimetry.

VEP and PERG measurements	NTG		Healthy	
	Left eye Mean (SD)	Right eye Mean (SD)	Left eye Mean (SD)	Right eye Mean (SD)
L100/15': at T ₀ at T ₁₂	124.0 (9.1)	123.9 (11.6)	111.2 (6.2)	111.5 (5.0)
	122.4 (10.6)	122.0 (10.4)	113.3 (7.2)	110.7 (4.8)
L100/30': at T ₀ at T ₁₂	114.9 (8.3)	114.0 (8.6)	105.2 (6.0)	105.6 (6.9)
	115.9 (6.8)	114.0 (8.8)	106.3 (8.9)	105.6 (6.1)
A100/15': at T ₀ at T ₁₂	8.3 (3.2)	8.0 (3.8)	14.5 (4.6)	14.9 (5.5)
	9.2 (3.4)	8.8 (3.4)	13.9 (4.6)	15.3 (5.7)
A100/30': at T ₀ at T ₁₂	7.7 (3.0)	8.5 (3.3)	13.1 (5.0)	14.4 (4.2)
	7.7 (2.5)	8.8 (3.4)	13.8 (6.4)	15.3 (5.6)
L50/15': at T ₀ at T ₁₂	63.1 (8.1)	61.0 (9.4)	61.5 (6.5)	58.9 (5.8)
	61.6 (7.5)	59.8 (6.6)	59.0 (6.1)	57.1 (4.7)
L50/30': at T ₀ at T ₁₂	58.9 (8.3)	56.7 (7.8)	57.5 (4.0)	55.7 (5.2)
	58.2 (7.2)	54.7 (4.8)	56.1 (5.6)	55.6 (5.3)
A50/15': at T ₀ at T ₁₂	1.5 (0.6)	1.5 (0.6)	2.5 (0.7)	2.2 (0.4)
	1.8 (0.6)	1.8 (0.8)	2.6 (0.7)	2.4 (0.8)
A50/30': at T ₀ at T ₁₂	1.9 (0.6)	1.9 (0.6)	2.7 (0.4)	2.7 (0.4)
	2.6 (0.9)	2.2 (0.7)	2.9 (0.9)	3.0 (0.9)
CRT/15': at T ₀ at T ₁₂	60.9 (13.7)	62.9 (10.9)	49.6 (5.9)	52.6 (7.0)
	60.8 (9.2)	62.2 (12.6)	54.3 (4.1)	53.6 (5.9)
CRT/30': at T ₀ at T ₁₂	56.0 (11.8)	57.2 (11.0)	47.8 (6.3)	49.9 (6.0)
	57.8 (9.8)	59.2 (9.6)	50.2 (9.3)	50.0 (7.9)

Other characteristics	NTG		Healthy		
	Left eye Mean (SD)	Right eye Mean (SD)	Left eye Mean (SD)	Right eye Mean (SD)	
MD:	at T_0	3.1 (1.6)	3.3 (1.5)	1.3 (1.2)	1.7 (1.4)
	at T_{12}	2.8 (1.8)	3.4 (1.7)	2.0 (1.9)	2.3 (1.8)
CLV:	at T_0	4.0 (2.8)	3.8 (2.7)	1.7 (1.0)	2.2 (1.3)
	at T_{12}	4.4 (3.2)	5.1 (4.9)	2.1 (1.3)	2.1 (1.1)
Lin.C\ D:	at T_0	639.8 (107.5)	640.5 (122.5)	688.5 (105.4)	718.7 (53.9)
	at T_{12}	637.8 (101.7)	642.0 (94.9)	687.7 (101.0)	717.9 (56.2)
RNFL:	at T_0	182.9 (55.2)	192.7 (47.3)	200.5 (79.5)	205.2 (57.3)
	at T_{12}	176.1 (59.3)	186.5 (43.6)	203.1 (67.4)	195.0 (36.3)
IOP:	at T_0	17.5 (2.6)	17.5 (2.2)	15.1 (2.8)	16.1 (3.3)
	at T_{12}	12.7 (1.2)	12.0 (1.7)	15.0 (2.4)	15.8 (3.0)
PAC:	at T_0	570.9 (39.1)	575.1 (38.8)	553 (43.8)	547.3 (42.3)

3. Furthermore, a global negative correlation emerged between amplitude measurements on one side, and latency measurements on the other, except for P50/30' PERG latency (vectors corresponding to amplitudes and latencies, respectively, point toward opposite directions). In this case, the values of Pearson's r vary from -0.58 to -0.18.

In Figure 1a, the points representing the eyes of NTG patients and healthy subjects show a considerable degree of separation. The latter ones (healthy subjects) are characterized by higher values of P100 VEP and P50N95 complex PERG amplitudes, and lower values of P100 VEP and P50 PERG latencies (overall, they stand on the right side of the figure), while the former (NTG) show just the opposite pattern (standing on the left side of the figure).

The measurements at T_{12} showed similar patterns of correlation (Fig. 1b) as those previously illustrated: that is, a positive correlation among amplitude measurements, most pronounced between the P100 VEP waves (P100/30' and P100/15'); a positive correlation among latency measurements, also most pronounced between the P100 VEP waves; and a negative correlation among latency and amplitude measurements (same as before). No other relevant relationships between variables emerged.

In the second PCA, according to the scree-plot three principal components were retained, with proportions of explained variability of data equal to 30.1%, 27.5%, and 21.5%, respectively. Given that a sound clinical interpretation was provided

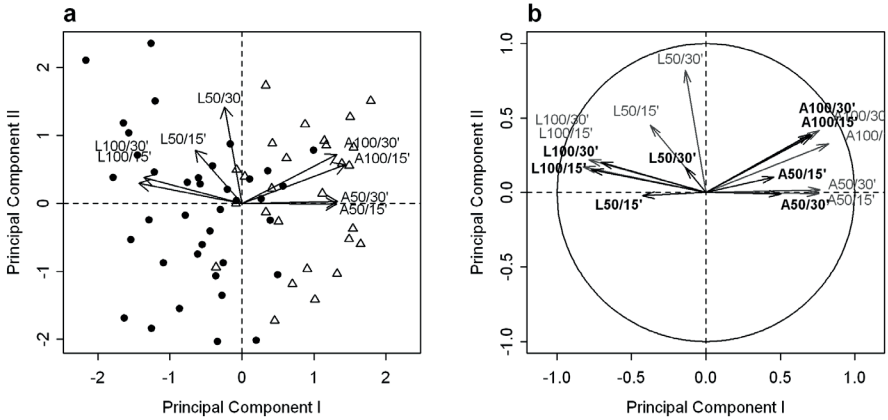


Fig. 1. Principal components of electrophysiological measurements
 (a) Principal component biplot. Vectors represent the active variables: P100 VEP latencies and amplitudes at T_0 , with 15-minutes and 30-minutes checkerboard pattern stimulus (L100/15', L100/30', A100/15', A100/30', respectively); P50 PERG latencies and amplitudes at T_0 (L50/15', L50/30', A50/15', A50/30'). Dots represent eyes of NTG patients; triangles represent eyes of healthy subjects. (b) Variables map, with active variables (gray) and passive variables (black). The passive variables were P100 VEP and P50 PERG latencies and amplitudes at T_{12} (labels: same as above).

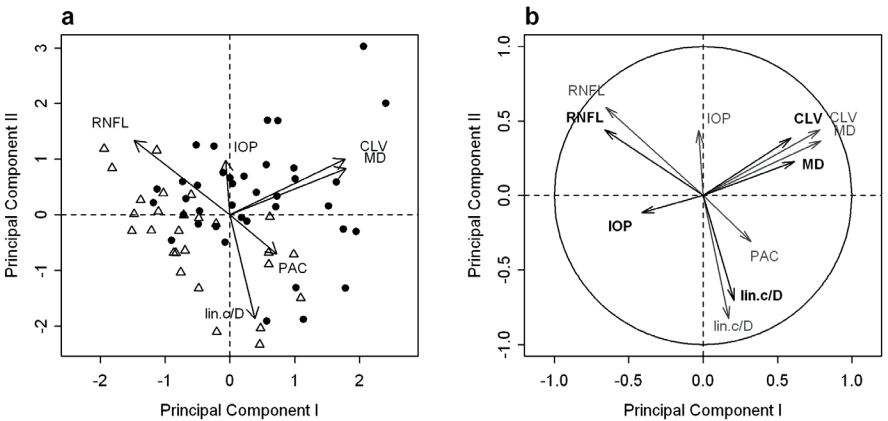


Fig. 2. Principal components of other diagnostic parameters
 (a) Principal component biplot. Vectors represent the active variables: Linear C/D (lin.C/D), RNFL thickness (RNFL), mean defect (MD), correct loss variance (CLV), intraocular pressure (IOP), pachymetry (PAC); Dots represent eyes of NTG patients; triangles represent eyes of healthy subjects. (b) Variables map, with active variables (gray) and passive variables (black). The passive variables were measurements at T_{12} of the variables above, except pachymetry

Table 2. Estimated average values and differences of diagnostic parameters

NTG = eyes of patients with suspected normal tension glaucoma; Healthy = eyes of healthy subjects. Electrophysiological parameters: L100 and L50 = latency of P100 VEP and P50 PERG waves, respectively; A100 and A50 = amplitude of P100 VEP and P50N95 complex PERG waves, respectively. The text: /15' and /30' indicate measurements taken with 15-minutes and 30-minutes checkerboard pattern stimulus, respectively. Visual field indices: MD = mean defect; CLV = correct loss variance. Morphometric parameters: RNFL = RNFL thickness; Lin.C/D = linear C/D. IOP = intraocular pressure. PAC = pachimetry.

VEP and PERG measurements	Estimated average values		Estimated average differences	
	NTG Est (95% CI)	Healthy Est (95% CI)	NTG vs Healthy: Est (95% corr. CI)	T ₁₂ vs T ₀ : Est (95% corr. CI)
L100/15': at T₀ at T₁₂	124.1 (120.4, 127.8) 122.3 (118.7, 126.0)	111.2 (106.8, 115.6) 111.9 (107.5, 116.3)	at T ₀ :12.9 (5.5, 20.2) at T ₁₂ : 10.5 (3.2, 17.8)	NTG:-1.7 (-4.0, 0.5) Healthy: 0.6 (-0.4, 1.7)
L100/30': at T₀ at T₁₂	114.3 (111.2, 117.5) 114.8 (111.6, 117.9)	105.4 (101.7, 109.2) 106.0 (102.2, 109.8)	at T ₀ : 8.9 (2.6, 15.1) at T ₁₂ : 8.8 (2.5, 15.0)	LNG:0.5 (-1.5, 2.5) Healthy:0.6 (-1.8, 3.0)
A100/15': at T₀ at T₁₂	8.2 (6.5, 9.9) 9.0 (7.3, 10.8)	14.6 (12.6, 16.7) 14.5 (12.5, 16.6)	at T ₀ : -6.4 (-9.8, -3.0) at T ₁₂ : -5.5 (-8.9, -2.1)	NTG:0.9 (-0.1, 1.8) Healthy: -0.1 (-1.2, 1.1)
A100/30': at T₀ at T₁₂	8.2 (6.5, 10.0) 8.4 (6.7, 10.1)	13.6 (11.6, 15.7) 14.5 (12.4, 16.5)	at T ₀ : -5.4 (-8.9, -2.0) at T ₁₂ : -6.1 (-9.5, -2.6)	NTG:0.2 (-0.8, 1.2) Healthy:0.8 (-0.3, 2.0)
L50/15': at T₀ at T₁₂	62.1 (59.7, 64.4) 60.7 (58.3, 63.0)	60.1 (57.4, 62.9) 58.0 (55.2, 60.8)	at T ₀ : 1.9 (-2.7, 6.5) at T ₁₂ : 2.7 (-1.9, 7.3)	NTG: -1.4 (-5.3, 2.5) Healthy: -2.1 (-6.7, 2.5)
L50/30': at T₀ at T₁₂	57.8 (55.7, 59.9) 56.4 (54.2, 58.5)	56.5 (54.0, 59.1) 55.8 (53.3, 58.4)	at T ₀ : 1.2 (-3.0, 5.5) at T ₁₂ : 0.5 (-3.7, 4.7)	NTG: -1.4 (-4.6, 1.8) Healthy: -0.7 (-4.5, 3.1)
A50/15': at T₀ at T₁₂	1.5 (1.2, 1.7) 1.8 (1.6, 2.1)	2.4 (2.1, 2.6) 2.5 (2.2, 2.8)	at T ₀ : -0.9 (-1.4, -0.4) at T ₁₂ : -0.7 (-1.1, -0.2)	NTG:0.3 (0.1, 0.6) Healthy:0.1 (-0.2, 0.5)
A50/30': at T₀ at T₁₂	1.9 (1.6, 2.2) 2.4 (2.1, 2.6)	2.7 (2.4, 3.0) 2.9 (2.6, 3.3)	at T ₀ : -0.8 (-1.3, -0.3) at T ₁₂ : -0.6 (-1.1, 0.0)	NTG:0.5 (0.2, 0.8) Healthy:0.3 (-0.1, 0.6)
CRT/15': at T₀ at T₁₂	61.8 (58.2, 65.4) 61.5 (57.9, 65.1)	51.1 (46.8, 55.4) 53.9 (49.6, 58.2)	at T ₀ : 10.7 (3.5, 17.9) at T ₁₂ : 7.6 (0.4, 14.8)	NTG: -0.3 (-4.6, 3.9) Healthy:2.8 (-2.3, 7.9)
CRT/30': at T₀ at T₁₂	61.8 (58.2, 65.4) 61.5 (57.9, 65.1)	51.1 (46.8, 55.4) 53.9 (49.6, 58.2)	at T ₀ :7.6 (0.6, 14.6) at T ₁₂ :8.2 (1.2, 15.2)	NTG:1.9 (-2.0, 5.8) Healthy:1.3 (-3.3, 5.8)

	Estimated average values		Estimated average differences	
Other characteristics	NTG Est (95% CI)	Healthy Est (95% CI)	NTG vs Healthy : Est (95% corr. CI)	T12 vs T0: Est (95% corr. CI)
MD : at T ₀ at T ₁₂	3.3 (2.7, 3.9) 3.2 (2.6, 3.9)	1.5 (0.8, 2.3) 2.2 (1.4, 2.9)	at T ₀ :1.7 (0.5, 3.0) at T ₁₂ :1.1 (-0.2, 2.3)	NTG:-0.1 (-0.6, 0.5) Healthy: 0.6 (0.0, 1.2)
CLV: at T ₀ at T ₁₂	3.9 (2.8, 5.0) 4.8 (3.8, 5.9)	2.0 (0.7, 3.3) 2.1 (0.8, 3.3)	at T ₀ : 1.9 (-0.2, 4.0) at T ₁₂ : 2.8 (0.6, 4.9)	NTG:0.9 (-0.1, 1.9) Healthy:0.1 (-1.1, 1.3)
Lin.C\D: at T ₀ at T ₁₂	641.1 (601.7, 680.5) 640.9 (601.5, 680.4)	703.8 (656.8, 750.8) 702.9 (655.9, 749.9)	at T ₀ : -62.7 (-140.9, 15.5) at T ₁₂ : -62.0 (-140.2, 16.2)	NTG:-0.2 (-21.2, 20.8) Healthy:-0.9 (-25.8, 24.1)
RNFL: at T ₀ at T ₁₂	188.2 (167.9, 208.4) 181.7 (161.4, 202.0)	202.8 (178.7, 227.0) 198.8 (174.6, 222.9)	at T ₀ : -14.7 (-54.9, 25.5) at T ₁₂ : -17.1 (-57.3, 23.1)	NTG:-6.5 (-19.2, 6.3) Healthy:-4.1 (-19.2, 11.0)
IOP: at T ₀ at T ₁₂	17.5 (16.5, 18.5) 12.3 (11.3, 13.3)	15.7 (14.5, 16.9) 15.5 (14.3, 16.7)	at T ₀ :1.8 (-0.2, 3.7) at T ₁₂ : -3.2 (-5.2, -1.3)	NTG:-5.2 (-5.9, -4.4) Healthy:-0.2 (-1.1, 0.7)
PAC: at T ₀	572.5 (555.2, 589.9)	549.6 (528.8, 570.3)	at T ₀ : 23.0 (-4.0, 50.0)	-

only for the first two components, the third one was excluded from the analysis. From the configuration of the vectors in Figure 2a, two major features emerge: a positive correlation between visual field defects (correlation between MD and CLV: $r = 0.67$) and a negative correlation between morphometric parameters (correlation between RNFL and lin C/D: $r = -0.43$)

In Figure 2a, the eyes of NTG patients and healthy subjects show a considerable degree of separation. The former are characterized by higher values of MD and CLV at T₀ (since overall they stand in the same direction of the MD and CLV vectors), while the latter are characterized by lower values of the same variables. The measurements at T₁₂ show, overall, similar patterns of correlation (Fig. 2b).

The estimates of the average values and differences are reported in Table 2. The average differences between eyes of NTG patients and healthy subjects of P100/15' VEP latencies are: 12.9 msec (95% CI: (5.5, 20.2) msec) at T₀, and 10.5 msec (95% CI: (3.2, 17.8) msec) at T₁₂, suggesting that the average values in the first group (NTG) were higher. Smaller differences, also indicating a higher positive difference between the two groups, emerged for P100/30' latencies: 8.9 msec (95% CI: (2.6, 15.1) msec) at T₀, and 8.8 msec (95% CI: (2.5, 15.0) msec) at T₁₂. For amplitude measurements, lower average values for the NTG group emerged, at T₀ and T₁₂, both for the P100 VEP wave and P50N95 complex PERG amplitudes. For example, the estimated differences at T₀ are: -6.4 μ V (95% CI: (-9.8, -3.0) μ V) for P100/15' VEP amplitude and -0.9 μ V (95% CI: (-1.4, -0.4) μ V) for P50/15' PERG amplitude. Furthermore, for P50 PERG amplitude, the average differences between T₁₂ and T₀ in the NTG group are: 0.3 μ V (95% CI: (0.1,

0.6) μV) for the P50/15' amplitude and 0.5 μV (95% CI: (0.2, 0.8) μV) for the P50/30' amplitude. Such values suggest an increase in amplitude after therapy (T_{12}), whereas no variation in time emerged from the remaining estimates for other electrophysiological measurements. For CRT, positive differences, indicating higher values in the NTG group, emerged both at T_0 and T_{12} .

Concerning the visual field indices: for MD, a positive average difference between NTG and healthy subjects emerged at T_0 : 1.7 dB (95% CI: (0.5, 3.0) dB), indicating that the average value in the NTG group was higher. Also, a positive difference between the groups is shown for CLV at T_{12} : 2.8 dB (95% CI: (0.6, 4.9) dB). For IOP, at T_0 no relevant difference emerged between NTG and healthy subjects; subsequently, the average difference between T_{12} and T_0 indicated a reduction of IOP in the NTG group only: -5.2 mmHg (95% CI: (-5.9, 4.4) mmHg). In agreement with this result, at T_{12} a negative difference between NTG and healthy subjects was found: -5.2 mmHg (95% CI: (-5.9, -4.4) mmHg). No sensible difference emerged for the remaining variables.

4. Discussion

The most important problem for the correct therapy of glaucoma is early diagnosis. The current opinion is that structural changes of the optic nerve fiber layer precede functional changes measured by automated perimetry.⁷³ However, sometimes a manifest optic nerve cupping is not correlated with visual defects, casting doubt as to whether these patients really have glaucomatous disease that can be prevented by therapy.⁷⁴⁻⁷⁶ In this respect, intraocular asymmetry of optic disk size can aid diagnosis.⁷⁷ Praecox diagnosis is more difficult in NTG because IOP values are apparently normal,⁷⁸ even if larger disks seem to be more susceptible to IOP-related stress because eyes with NTG have a significantly thinner lamina cribrosa and therefore undergo significant displacement due to IOP according to mathematical finite element modeling.^{79,5} Neuroretinal rim loss occurs before visual field loss,^{64,80} but there is a linear relationship comparing 1/lambert differential light threshold (not logarithmic (decibel) scaling) in visual field and temporal rim area.⁸¹

Among diagnostic exams, electrophysiological tests, such as VEPs and PERG, can be used to quantify RGC function. Retinal ganglion cells undergo a prolonged period of dysfunction and degeneration before cell loss. In fact, many authors have found impaired RGC function by means of electrophysiological measurement in both experimental^{82-84,44} and human glaucoma studies⁸⁵ in subjects with OHT and early POAG with no or minimal visual field defects.^{86,54} In NTG there has been only one electrophysiological study: Lestak found a remarkable P100 amplitude reduction while PERG was almost unaffected.⁸⁷

Likewise, some authors^{55,56} indicate that abnormal PERG recorded in eyes with early stages of glaucoma may often improve after IOP reduction. Therefore, this dysfunction may be partially restored after IOP reduction not only in OHT, but

also in glaucoma patients, as well as in NTG. In the case of NTG, improvement is seen even after smaller IOP reductions because NTG eyes have a lower functional threshold. However, in patients with advanced glaucoma PERG improvement is only slight given that the amount of RGC loss is greater, limiting functional recovery.

In our study of NTG suspects, P100 amplitude VEPs was reduced and P100 latency was slightly delayed. After IOP reduction, these parameters did not show significant modification: this is understandable, as topical therapy is unlikely to have an effect on the functionality (strictly neurological) of the visual pathways. In addition, P50N95 complex amplitude was found to be lower in the NTG group than in the control group.

IOP decreased significantly after therapy, even if the baseline IOP was slightly higher than 15.5 mmHg, demonstrating that these patients had, in fact, NTG, as explained above. Otherwise, P50N95 complex amplitude rose slightly; this is correlated to IOP lowering, also for slight values.⁸⁸ There is no inverse correlation between the amount of P50 amplitude increase and IOP reduction.

IOP reduction is correlated to the effective presence of glaucoma; in fact, IOP reduction in normal eyes does not modify P50N95 complex amplitude at all. Therefore, an increase in P50N95 complex PERG amplitude following a decrease in IOP is suggestive of dysfunction in suspected glaucoma (in this study, NTG); this dysfunction could be partially restored after hypotonizing.⁵⁶

Morphometric parameters, *i.e.*, RNFL and linear C/D showed no modification in the NTG suspect group one year after hypotonizing therapy, and neither did visual field indices (MD and CLV). If there is only RGC dysfunction, it is unlikely that optic nerve head changes would be apparent.⁸⁹ In this sense, electrophysiological tests could provide a more sensitive measure of RGC integrity.

This pilot study is the first to attempt to differentiate between normal patients with apparent larger disc cupping and NTG suspects with quite normal visual fields. This diagnostic approach may provide important information to avoid starting useless therapy, or, on the contrary, to start precociously hypotonizing therapy in NTG suspects before visual field loss occurs.

Finally, electrophysiological tests could also be used in a similar fashion to the visual field test, but with greater sensibility, allowing ophthalmologists to monitor personalized therapy and even change its course by providing functional information. Furthermore, these tests may provide an objective and indisputable assessment of the effectiveness of neuroprotective therapies.

References

1. Heijl A, Leske MC, Bengtsson B, Hyman L, Hussein M. Reduction of intraocular pressure and glaucoma progression: results from the early manifest glaucoma trial. *Arch Ophthalmol* 2002;120:1268-1279.

2. Kass MA, Heuer DK, Higginbotham EJ, Johnson CA, Keltner JL, Miller JP, et al. The ocular hypertension treatment study: a randomized trial determines that topical ocular hypotensive medication delays or prevents the onset of primary open-angle glaucoma. *Arch Ophthalmol* 2002;120:701-713.
3. Krupin T. Special considerations in low-tension glaucoma. *Can. J. Ophthalmol* 2007;42(3):414-417. Available from: <http://article.pubs.nrc-cnrc.gc.ca/RPAS/rpv?hm=HInit&calyLang=eng&journal=cjo&volume=42&afpf=i07-043.pdf> doi: 10.3129/i07-043.
4. Sowka J. New thoughts on normal tension glaucoma. *Optometry - Journal of the American Optometric Association* 2005;76(10):600-608. Available from: <http://linkinghub.elsevier.com/retrieve/pii/S1529183905001387> doi: 10.1016/j.optm.2005.08.020.
5. Hayamizu F, Yamazaki Y, Nakagami T, Mizuki K. Optic disc size and progression of visual field damage in patients with normal-tension glaucoma. *Clinical Ophthalmology* 2013;7:807-813.
6. Bonomi L, Marchini G, Marraffa M. et al Prevalence of glaucoma and intraocular distribution in a definite population. The Enge-Neumarkt Study. *Ophthalmology* 1998;105(2):209-215. Available from: <http://linkinghub.elsevier.com/retrieve/pii/S0161642098926653> doi: 10.1016/S0161-6420(98)92665-3.
7. Dielemans I, Vingerling JR, Wolfs RC, et al. The prevalence of primary open angle glaucoma in a population based study in the Netherlands. The Rotterdam Study. *Ophthalmology* 1994;101(11):1851-1855. Available from: <http://linkinghub.elsevier.com/retrieve/pii/S0161642094310906> doi: 10.1016/S0161-6420(94)31090-6.
8. group, n.t.g.s. (Collaborative) . Collaborative normal tension glaucoma study group. Comparison of glaucomatous progression between untreated patients with normal-tension glaucoma and patients with therapeutically reduced intraocular pressures. *Am J Ophthalmol* 1998;126:126-487.
9. group, n.t.g.s. (Collaborative) . Collaborative normal tension glaucoma study group. The effectiveness of intraocular pressure reduction in the treatment of normal tension glaucoma. *Am J Ophthalmol* 1998;126:126-498.
10. group, n.t.g.s. (Collaborative) . Collaborative normal tension glaucoma study group. Risk factors for progression of visual field abnormalities in normal tension glaucoma. *Am J Ophthalmol* 2001;131:699-708.
11. group, n.t.g.s. (Collaborative) . Collaborative normal tension glaucoma study group. Factors that predict the benefit of lowering intraocular pressure in normal tension glaucoma. *Am J Ophthalmol* 2003;2003:136-820.
12. Sergi M, Salerno DE, Rizzi M, Blini M, Andreoli A. Messenio D, pecis M, Bertoni G: Prevalence of normal tension glaucoma in obstructive sleep apnea syndrome patients. *J Glaucoma* 2007 2007;16:42-46.
13. Meyer JH, Brandi- Dohrn J, , Funk J. Twenty four hour blood pressure monitoring in normal tension glaucoma. *Br J Ophthalmol* 1996;80(10):864-867. Available from: <http://bjo.bmj.com/cgi/doi/10.1136/bjo.80.10.864> doi: 10.1136/bjo.80.10.864.
14. Collignon N, Dewe W, Guillaume S, Collignon-Brach J. Ambulatory blood pressure monitoring in glaucoma patients. The nocturnal systolic dip and its relationship with disease progression. *Int Ophthalmol* 1998;22:19-25.
15. Liu JH. Diurnal measurement of intraocular pressure. *J Glaucoma* 2001 2001;10:39-41.
16. Gupta N, Yucel YH. Glaucoma in the brain: a piece of the puzzle. *Can J Ophthalmol* 2006;41(5):541-542. Available from: <http://linkinghub.elsevier.com/retrieve/pii/S0008418206800220> doi: 10.1016/S0008-4182(06)80022-0.
17. Weber AJ, Harman C. Structure-function relations of parasol in the normal and glaucomatous primate retina. *Invest Ophthalmol Vis Sci* 2005;46:3197-3207.
18. Yucel YH, Zhand Q, Gupta N, Kaufman PL, Weinreb RN. Loss of neurons in magnocellular and parvocellular layers of the lateral geniculate nucleus in glaucoma. *Arch Ophthalmol* 2000;118(3):378-384. Available from: <http://archophth.jamanetwork.com/article.aspx?doi=10.1001/archophth.118.3.378> doi: 10.1001/archophth.118.3.378.
19. Yucel YH, Zhang Q, Weinreb RN, Kaufman PL, Gupta N. Effects of retinal ganglion cell loss on magno-, parvo-, koniocellular pathways in the lateral geniculate nucleus and visual cortex in glaucoma. *Prog*

- Retin Eye Res 2003;22(4):465-481. Available from: <http://linkinghub.elsevier.com/retrieve/pii/S1350946203000260> doi: 10.1016/S1350-9462(03)00026-0.
20. Gupta N, Glaucoma YH, brain t. . J Glaucoma 2001;10:28-29.
 21. Maffei L, Fiorentini A. Electroretinographic responses to alternating gratings before and after section of the optic nerve. Science 1981;211(4485):953-954. Available from: <http://www.sciencemag.org/cgi/doi/10.1126/science.7466369> doi: 10.1126/science.7466369.
 22. Bach M, Gerling J, Geiger . K: Optic atrophy reduces the pattern-electroretinogram for both fine and coarse stimulus pattern. Clin Vis Sci 1992;327-333.
 23. Trick GL, Neshe R, Cooper DG. et al: The human pattern ERG: alterations of response properties with aging. Optom Vis Sci 1992;69(2):122-128. Available from: <http://content.wkhealth.com/linkback/openurl?sid=WKPTLP:landingpage&an=00006324-199202000-00005> doi: 10.1097/00006324-199202000-00005.
 24. Porciatti V, Burr DC, Morrone MC, Fiorentini . A The effects of aging on the pattern electroretinogram and visual evoked potentials in humans: Vision Res. 1992;32:1199-1209.
 25. Bach M. Electrophysiological approaches for early detection of glaucoma. Eur J Ophthalmol 2001; 25. suppl 2001;2:41-49.
 26. Bach M, Hoffmann MB. Update on the Pattern Electroretinogram in Glaucoma. Optometry and Vision Science 2008;85(6):386-395. Available from: <http://content.wkhealth.com/linkback/openurl?sid=WKPTLP:landingpage&an=00006324-200806000-00009> doi: 10.1097/OPX.0b013e318177ebf3.
 27. Van_den_Berg TJ, Riemsdag FC, de Vos GW, Verduyn Lunel HF. Pattern ERG and glaucomatous visual field defects. Doc Ophthalmol 1986;61(3-4):335-341. Available from: <http://link.springer.com/10.1007/BF00142361> doi: 10.1007/BF00142361.
 28. Bach M, Sulimma F, Gerling J. Little correlation of the pattern electroretinogram (PERG) and visual field measures in early glaucoma. Doc Ophthalmol 1997;94(3):253-263. Available from: <http://link.springer.com/10.1007/BF02582983> doi: 10.1007/BF02582983.
 29. Quigley HA, Addicks EM, Green . WR: Optic nerve damage in human glaucoma. III Quantitative correlation of nerve fiber loss and visual field defect in glaucoma, ischemic neuropathy, papilledema and toxic neuropathy. Arch Ophthalmol 1982;100:100-135.
 30. Porciatti V, Falsini B, Brunori S, et al. Pattern electroretinogram as a function of spatial frequency in ocular hypertension and early glaucoma. Doc Ophthalmol 1987;65(3):349-355. Available from: <http://link.springer.com/10.1007/BF00149941> doi: 10.1007/BF00149941.
 31. Ventura LM, Porciatti DS. Restoration of retinal ganglion cell function in early glaucoma after intraocular pressure reduction. A pilot study. Ophthalmology 2005;112(1):20-27. Available from: <http://linkinghub.elsevier.com/retrieve/pii/S0161642004014630> doi: 10.1016/j.ophtha.2004.09.002.
 32. Caprioli J, Sears M, Miller JM. Patterns of early visual field loss in open-angle glaucoma. Am J Ophthalmol 1987;104(1):98-98. Available from: <http://linkinghub.elsevier.com/retrieve/pii/000293948790314X> doi: 10.1016/0002-9394(87)90314-X.
 33. Wanger P, Persson . HE: Pattern-reversal electroretinograms in unilateral glaucoma. Invest Ophthalmol Vis Sci. 1983;24:749-753.
 34. Papst N, Bopp M, Schnaudigel OE. The pattern evoked electroretinogram associated with elevated intraocular pressure. Graefe's archive for clinical and experimental ophthalmology 1984 Oct;222(1):34-7. Available from: <http://link.springer.com/10.1007/BF02133775> doi: 10.1007/BF02133775.
 35. Price MJ, Drance SM, Price M, Schulzer M, Douglas GR, Tansley B. The pattern electroretinogram and visual-evoked potential in glaucoma. Graefe's archive for clinical and experimental ophthalmology 1988 Nov;226(6):542-7. Available from: <http://link.springer.com/10.1007/BF02169202> doi: 10.1007/BF02169202.
 36. Weinstein GW, Arden GB, Hitchings RA. The pattern electroretinogram (PERG) in ocular hypertension and glaucoma. Arch Ophthalmol 1988;106(7):923-928. Available from: <http://archophth.jamanetwork.com/article.aspx?articleid=637346> doi: 10.1001/archophth.1988.01060140069027.

37. Arai M, Yoshimura N, Sakaue H, Chihara E, Honda Y. A 3-year follow-up study of ocular hypertension by pattern electroretinogram. *Ophthalmologica* 1993;207(4):187-95. Available from: <http://www.karger.com/doi/10.1159/000310431> doi: 10.1159/000310431.
38. Fj GI, Fj FT, Almarcegui Lafita C, , Polo Llorens V, , Sanches Perez A . Honrubia Lopez FM. Predictive value of the pattern-electroretinogram in glaucoma (in. Spanish). *Arch Soc Esp Oftalmol* 2001;76:485-491.
39. Unsoeld AS, Walter S, Meyer J, Funk J, Bach M. Pattern ERG as an early risk indicator in ocular hypertension – a 9-year prospective study. *Invest Ophthalmol Vis Sci (Suppl)*: S146.2001.
40. Bach M, Unsoeld AS, Philippin H, et al. Pattern ERG as an early indicator in ocular hypertension: a long-term prospective study. *Invest Ophthalmol Vis Sci* 2006;47(11):4881-4887. Available from: <http://iovs.arvojournals.org/article.aspx?doi=10.1167/iovs.05-0875> doi: 10.1167/iovs.05-0875.
41. Pfeiffer N, Tillmon B, Bach M. Predictive value of pattern electroretinogram in high-risk ocular hypertension. *Invest Ophthalmol Vis Sci* 1993;34:1710-1715.
42. Philippin H, Unsoeld A, Maier P, Walter S, Bach M, Funk J. Ten-year results: detection of long-term progressive optic disc changes with confocal laser tomography. *Graefes Arch Clin Exp Ophthalmol* 2005;244:1-5.
43. Marx MS, Podos SM, Bodis-Wollner I. et al: Signs of early damage in glaucomatous monkey eyes: low spatial frequency losses in the pattern. ERG and VEP. *Exp Eye Res* 1988;46-173.
44. Saleh M, Nagaraju M, Porciatti V. Longitudinal evaluation of retinal ganglion cell function and IOP in the DBA/2J mouse model of glaucoma. *Invest Ophthalmol Vis Sci* 2007;48(10):4564-4572. Available from: <http://iovs.arvojournals.org/article.aspx?doi=10.1167/iovs.07-0483> doi: 10.1167/iovs.07-0483.
45. Porciatti V, Saleh M, Nagaraju M. The pattern electroretinogram as a tool to monitor progressive retinal ganglion cell dysfunction in the DBA/2J mouse model of glaucoma. *Invest Ophthalmol Vis Sci* 2007;48(2):745-751. Available from: <http://iovs.arvojournals.org/article.aspx?doi=10.1167/iovs.06-0733> doi: 10.1167/iovs.06-0733.
46. Ventura LM, Porciatti V. Pattern electroretinogram and glaucoma. *Curr Opin Ophthalmol* 2006;17(2):196-202. Available from: <http://content.wkhealth.com/linkback/openurl?sid=WKPTLP:landingpage&an=00055735-200604000-00013> doi: 10.1097/01.icu.0000193082.44938.3c.
47. Parisi V, Manni G, Centofanti M, Gandolfi SA, Olzi D, Bucci MG. Correlation between optical coherence tomography, pattern electroretinogram, and visual evoked potentials in open-angle glaucoma patients. *Ophthalmology* 2001 May;108(5):905-12. Available from: <http://linkinghub.elsevier.com/retrieve/pii/S0161642000006448> doi: 10.1016/S0161-6420(00)00644-8.
48. Ventura LM, Sorokac N, De_Los Santos R, , Feuer WJ. Porciatti V: The relationship between retinal ganglion cell function and retinal nerve fiber thickness in early glaucoma. *Invest Ophthalmol Vis Sci* 2006;47:3904-3911.
49. Salgarello T, Colotto A, Falsini B. et al: Correlation of pattern electroretinogram with optic disc cup shape measure in ocular hypertension. *Invest Ophthalmol Vis Sci* 1999;40:1989-1997.
50. Salgarello T, Falsini B, Stifano G. et al: Morpho-functional follow-up of the optic nerve in treated ocular hypertension: disc morfometry and steady-state pattern electroretinogram. *Curr Eye Res* 2008;33(8):709-721. Available from: <http://www.tandfonline.com/doi/full/10.1080/02713680802277692> doi: 10.1080/02713680802277692.
51. Parisi V, Miglior S, Manni G, Centofanti M, Bucci . M: Clinical ability of pattern electroretinograms and visual evoked potentials in detecting visual dysfunction in ocular hypertension and glaucoma. *Ophthalmology*; 2006.
52. Bayer AU, Maag KP, Erb C, , Detection of optic neuropathy in glaucomatous eyes with normal standard visual fields using a test battery of short-wavelength automated perimetry and pattern electroretinography. 2002;109:1350-1361.
53. Ventura LM, Porciatti V, et al. Pattern electroretinogram abnormality and glaucoma. *Ophthalmology* 2005;112(1):10-19. Available from: <http://linkinghub.elsevier.com/retrieve/pii/S0161642004012606> doi: 10.1016/j.ophtha.2004.07.018.

54. Hood DC, Xu L, Thienprasiddhi P, Greenstein VC, Odel JG, Grippo TM, Liehmann JM, Rithc R: The pattern electroretinogram in glaucoma patients with confirmed visual field deficit. *Invest Ophthalmol Vis Sci* 2005;46:2411-2418.
55. Ventura LM, Porciatti DS. Restoration of retinal ganglion cell function in early glaucoma after intra-ocular pressure reduction. A pilot study. *Ophthalmology* 2005;112(1):20-27. Available from: <http://linkinghub.elsevier.com/retrieve/pii/S0161642004014630> doi: 10.1016/j.ophtha.2004.09.002.
56. North RV, Jones AL, Drasdo N, Wild JM, Morgan JE. Electrophysiological evidence of early functional damage in glaucoma and ocular hypertension. *Inv Ophthalmol Vis Sci* 2010;51(2):1216-1222. Available from: <http://iovs.arvojournals.org/article.aspx?doi=10.1167/iovs.09-3409> doi: 10.1167/iovs.09-3409.
57. Ventura LM, Feuer JW, Porciatti V. Progressive loss of retinal ganglion cell function is hindered with IOP-lowering treatment in early glaucoma. *Invest Ophthalmol Vis Sci* 2012;53(2):659-663. Available from: <http://iovs.arvojournals.org/article.aspx?doi=10.1167/iovs.11-8525> doi: 10.1167/iovs.11-8525.
58. Marx MS, Podos SM, et al. Flash and pattern electroretinograms in normal and laser-induced glaucomatous primate eyes. *Invest Ophthalmol Vis Sci* 1986;27:378-386.
59. Parisi V, Pernini C, Guinetti C, et al. Electrophysiological assesment of visual pathways in glaucoma. *Eur J Ophthalmol* 1997;7:229-235.
60. Horn FK, Jonas JB, Budde WM, Junemann AM, Mardin CY, Korth M. Monitoring glaucoma progression with visual evoked potentials of the blue-sensitive pathway. *Invest Ophthalmol Vis Sci* 2002;43:1828-1834.
61. Celesia GG, Kaufman D, Cone SB. Simultaneous recording of pattern electroretinography and visual evoked potentials in multiple sclerosis. A method to separate demyelination from axonal damage to the optic nerve. *Arch Neurol* 1986;43(12):1247-1247. Available from: <http://archneur.jamanetwork.com/article.aspx?doi=10.1001/archneur.1986.00520120031012> doi: 10.1001/archneur.1986.00520120031012.
62. Brusini P. Clinical use of a new method for visual field damage classification in glaucoma. *Eur J Ophthalmol* 1996;6:402-407.
63. Brusini P, Filacorda S. Enhanced Glaucoma Staging System (GSS 2) for Classifying Functional Damage in Glaucoma. *Journal of Glaucoma* 2006;15(1):40-46. Available from: <http://content.wkhealth.com/linkback/openurl?sid=WKPTLP:landingpage&an=00061198-200602000-00010> doi: 10.1097/01.ijg.0000195932.48288.97.
64. Garway-Heath DF, Wollstein G, Hitchings RA. Angong changes of the optic nerve head in relationship to open angle glaucoma. *Br J Ophthalmol* 1997;81(10):840-845. Available from: <http://bjo.bmj.com/cgi/doi/10.1136/bjo.81.10.840> doi: 10.1136/bjo.81.10.840.
65. Kamal DS, Viswanathan AC, Garway-Heath DF, et al. Detection of optic disc change in ocular hypertensives converting to early glaucoma. *Br J Ophthalmol* 1999;83(3):290-294. Available from: <http://bjo.bmj.com/cgi/doi/10.1136/bjo.83.3.290> doi: 10.1136/bjo.83.3.290.
66. Medvev N, Cvenkel B. Diagnostic accuracy of the Moorfields Regression Analysis using the Heidelberg Retina Tomography in glaucoma patients with visual field defects. *Eur J Ophthalmol* 2007;17(17):216-222.
67. Jolliffe I. *Principal component analysis*. John Wiley & Sons, Ltd; 2002.
68. Gabriel KR. The biplot graphic display of matrices with application to principal component analysis. *Biometrika* 1971;58-3.
69. Murdoch IE, Morris SS, Cousens SN. People and eyes: statistical approaches in ophthalmology. *British Journal of Ophthalmology* 1998 Aug;82(8):971-973. Available from: <http://bjo.bmj.com/cgi/doi/10.1136/bjo.82.8.971> doi: 10.1136/bjo.82.8.971.
70. Team RC R <http://www.R-project.org> . A Language and Environment for Statistical Computing (Version 3.1. 2): R Foundation for Statistical Computing. Vienna, Austria. Available from URL 2015.
71. Pinheiro J, Bates D, DebRoy S, Sarkar D, Core R. Team 2015. *nlme: Linear and Nonlinear Mixed Effects Models*. R package version 3.1. URL: <http://CRAN.R-project.org/package=nlme>; .
72. Hothorn T, Bretz F, Westfall P. Simultaneous Inference in General Parametric Models. *Biometrical Journal* 2008;50(3):346-363.

73. Sommer A, Tielsch JM, Katz J, et al. Clinically detectable nerve fiber atrophy precedes the onset of glaucomatous field loss. *Arch Ophthalmol* 1991;109(1):77-83. Available from: <http://archophth.jamanetwork.com/article.aspx?doi=10.1001/archophth.1991.01080010079037> doi: 10.1001/archophth.1991.01080010079037.
74. Burk RO, Rohrschneider K, Noack H, Volker HE. Are large optic nerve heads susceptible to glaucomatous damage at normal intraocular pressure? A three-dimensional study by laser scanning tomography. *Graefes Arch Clin Exp Ophthalmol* 1992;230(6):552-560. Available from: <http://link.springer.com/10.1007/BF00181778> doi: 10.1007/BF00181778.
75. Wang L, Damji KF, Munger R, et al. Increased disk size in glaucomatous eyes versus normal eyes in the Reykjavik eye study. *Am J Ophthalmol* 2003;135(2):226-228. Available from: <http://linkinghub.elsevier.com/retrieve/pii/S0002939402019281> doi: 10.1016/S0002-9394(02)01928-1.
76. Jb J, Xu L, Zhang L, Wang Y. Optic disc size in chronic glaucoma: the Beijing eye study. *Am J Ophthalmol* 2006;142(1):168-170. Available from: <http://linkinghub.elsevier.com/retrieve/pii/S0002939406001905> doi: 10.1016/j.ajo.2006.01.068.
77. Tomita G, Nyman K, Raitta C, Kawamura M. Intraocular asymmetry of optic disc size and its relevance to visual field loss in normal-tension glaucoma. *Graefes Arch Clin Exp Ophthalmol* 1994;232(5):290-296. Available from: <http://link.springer.com/10.1007/BF00194478> doi: 10.1007/BF00194478.
78. Jonas JB, Sturmer J, Papastathopoulos KI, Meier-Gibbons F, Dichtl A. Optic disc size and optic nerve damage in normal pressure glaucoma. *British Journal of Ophthalmology* 1995 Dec;79(12):1102-1105. Available from: <http://bjo.bmj.com/cgi/doi/10.1136/bjo.79.12.1102> doi: 10.1136/bjo.79.12.1102.
79. Bellezza AJ, Hart RT, Burgoyne CF. The optic nerve head as a biomechanical structure: initial finite element modeling. *Investigative ophthalmology & visual science* 2000.;41(10):2991-3000.
80. Tuulonen A, Lehtola J, Airaksinen PJ. Nerve fiber layer defects with normal visual field: do normal optic disc and normal visual field indicate absence of glaucomatous abnormality. *Ophthalmology* 1993;100(5):587-597. Available from: <http://linkinghub.elsevier.com/retrieve/pii/S0161642093315988> doi: 10.1016/S0161-6420(93)31598-8.
81. Garway-Heath DF, Holder GE, Fizke FW, et al. Relationship between electrophysiological, psychophysiological and anatomical measures in glaucoma. *Invest Ophthalmol Vis Sci* 2002;43:2213-2220.
82. Harwerth RS, Crawford M, Frishman LJ, et al. Visual field defects and neural losses from experimental glaucoma. *Prog Retin Eye Res* 2002;21(1):91-125. Available from: <http://linkinghub.elsevier.com/retrieve/pii/S1350946201000222> doi: 10.1016/S1350-9462(01)00022-2.
83. Swanson WH, Felius J, Pan F. Perimetric defects and ganglion cell damage: interpreting linear relations using a two-stage neural model. *Invest Ophthalmol Vis Sci* 2004;45(2):466-472. Available from: <http://iovs.arvojournals.org/article.aspx?doi=10.1167/iovs.03-0374> doi: 10.1167/iovs.03-0374.
84. Marx MS, Podos SM, Bodis-Wollner . pattern electroretinograms in normal and laser-induced glaucomatous primate eyes. *Invest Ophthalmol Vis Sci* 1986;27:378-386.
85. Kerrigan-Baumrind LA, Quigley HA, Pease ME, et al. Number of ganglion cells in glaucoma eyes compared with threshold visual field tests in the same persons. *Invest Ophthalmol Vis Sci* 2000;41:741-748.
86. Neoh C, Kaye SB, Brown M, et al. Pattern electroretinogram and automated perimetry in patients with glaucoma and ocular hypertension. *Br J Ophthalmol* 1994;78(5):359-362. Available from: <http://bjo.bmj.com/cgi/doi/10.1136/bjo.78.5.359> doi: 10.1136/bjo.78.5.359.
87. Lestak J, Elena N, Sarka P, Krejcova H, Bartosova L, High FV. tension versus normal tension glaucoma. A comparison of structural and function examinations. *J Clin Experiment Ophthalmol*;2012:1-4.
88. Karaskiewicz J, Drobek-Slowik M, Libinski W. Pattern electroretinogram (PERG) in the early diagnosis of normal-tension glaucoma: a case report. *Doc Ophthalmol* 2014;128(1):53-58. Available from: <http://link.springer.com/10.1007/s10633-013-9414-x> doi: 10.1007/s10633-013-9414-x.
89. Falsini B, Marangoni D, Salgarello T, et al. Structure-function relationship in ocular hypertension and glaucoma: interindividual and interocular analysis by OCT and pattern ERG. *Graefes Arch Clin Exp Ophthalmol* 2008;246(8):1153-1162. Available from: <http://link.springer.com/10.1007/s00417-008-0808-5> doi: 10.1007/s00417-008-0808-5.



Equilibrium shape of the aqueous humor-vitreous substitute interface in vitrectomized eyes

Krystyna Isakova¹, Jan O. Pralits², Mario R. Romano³, Jan-Willem M. Beenakker⁴, Denis P. Shamonin⁵, Rodolfo Repetto²

¹Department of Mechanical, Materials and Manufacturing Engineering, University of Nottingham, Nottingham, UK, ²Department of Civil, Chemical and Environmental Engineering, University of Genoa, Italy, ³Department of Neurosciences, University of Naples Federico II, Naples, Italy, ⁴Department of Radiology, C.J. Gorter Center for High-Field MRI, Leiden University Medical Center, Leiden, The Netherlands and Department of Ophthalmology, Leiden University Medical Center, Leiden, The Netherlands, ⁵Department of Radiology, Division of Image Processing, Leiden University Medical Center, Leiden, The Netherlands

Abstract

Purpose: To predict the shape of the interface between aqueous humor and a gas or silicone oil (SO) tamponade in vitrectomized eyes. To quantify the tamponated retinal surface for various eye shapes, from emmetropic to highly myopic eyes.

Methods: We use a mathematical model to determine the equilibrium shape of the interface between the two fluids. The model is based on the volume of fluids (VOF) method. The governing equations are solved numerically using the free software OpenFOAM. We apply the model to the case of idealized, yet realistic, geometries of emmetropic and myopic eyes, as well as to the real geometry of the vitreous chamber reconstructed from magnetic resonance imaging (MRI) images.

Results: The numerical model allows us to compute the equilibrium shape of the interface between the aqueous humor and the tamponade fluid. From this we can compute the portion of the retinal surface that is effectively tamponated by the fluid. We compare the tamponating ability of gases and SOs. We also compare the tamponating effect in emmetropic and myopic eyes by computing both tamponated area and angular coverage.

Correspondence: Department of Civil, Chemical and Environmental Engineering, University of Genoa, Via Montallegro 1, 16145 Genoa, Italy.

E-mail: rodolfo.repetto@unige.it

Conclusion: The numerical results show that gases have better tamponating properties than SOs. We also show that, in the case of SO, for a given filling ratio the percentage of tamponated retinal surface area is smaller in myopic eyes. The method is valuable for clinical purposes, especially in patients with pathological eye shapes, to predict the area of the retina that will be tamponated for a given amount of injected fluid.

Keywords: vitrectomy, tamponade fluids, surface tension, interface

1. Introduction

Rhegmatogenous retinal detachment (RRD) is the most common type of retinal detachment. It classically involves the presence of three factors: vitreous traction on the retinal surface, full-thickness retinal breaks, and liquefied vitreous allowing the passage of fluid from the preretinal space through the retinal breaks (RBs) into the subretinal space.¹ The intraocular surgical approach to RRD is vitrectomy, aimed at relieving vitreous traction on the edge of the RBs.² In order to close the passage between preretinal and subretinal spaces, it is necessary to induce reattachment between the retina and choroid. Intraocular tamponades, used during vitreoretinal surgery, aim at facilitating this reattachment, keeping in contact retina and choroid in correspondence of the RBs, until a chorio-retinal scar is well formed.³ In the early postoperative period, the patient has to maintain a precise head position as to maintain the tamponade fluid in contact with the RBs.⁴

Owing to the hydrophobic properties of tamponade fluids, after vitrectomy a pocket of aqueous humor is invariably present in the vitreous chamber. The maximum filling that the surgeon can normally obtain is approximately 90% of the volume of the vitreous chamber.⁵ For a given volume of tamponade fluid injected in the eye, the tamponated retinal surface is strongly affected by the shape of the interface between the tamponade fluid and the aqueous humor. The equilibrium configuration of the interface depends on the shape of the domain, on the physical properties of the two fluids (in particular on density difference, surface tension, and contact angle with the retina), and head orientation.

This problem was studied by Eames *et al.*,⁶ who modeled the vitreous chamber as a sphere filled with two different fluids, and determined the shape of the interface using a mathematical approach as well as experiments on a model. From their analysis, the authors obtained a relationship between retinal coverage and the volume of tamponade fluid. The main assumption underlying the work by Eames *et al.*⁶ is related to the use of a spherical eye model. In reality, the vitreous chamber is not spherical, in particular owing to the indentation produced in the front part by the lens. The concavity change of the domain in the anterior part is likely to significantly affect the shape of the interface; therefore, it is of clinical interest to study the equilibrium configuration of a tamponade fluid in a realistic eye geometry. In addition, understanding how the interface shape might change in myopic eyes, which are at a higher risk of developing

retinal detachment and whose shape is different with respect to that of emmetropic eyes, is highly relevant. To increase the success rate of the surgery, it is important to predict the surface of the retina that will be effectively tamponated, which depends on the shape of the interface between the aqueous and the tamponade.

In this paper, we compute the shape of such an interface for both emmetropic and myopic eyes. We first consider idealized but realistic shapes of the vitreous chamber and, subsequently, real eye geometry reconstructed from MR-measurements. We focus our attention on cases in which the patient maintains the upright position, but the method could be applied to other cases without additional difficulties.

2. Materials and methods

2.1 Mechanical properties of tamponade fluids

It is well known that the shape of the static equilibrium interface between two fluids can be obtained by solving the Laplace-Young equation, imposing the contact angle at the triple line given by the intersection between the interface and the wall. The solution depends on the fluid densities, the surface tension at the interface, and the static contact angle at the solid wall. We note that fluid viscosity does not affect the equilibrium configuration of the interface.⁷ In this paper we consider two tamponades that are commonly used in vitrectomy: SO and gas. In Table 1 we list the relevant mechanical properties of these fluids and the corresponding references. The properties of the SO are those of Oxane 1300. The surface tension and contact angle for the gas are taken from Eames *et al.*⁶, while the density is that of air. The density of a tamponade gas depends, in general, on its chemical compound (C2F6, C3F8, or SF6) and concentration, but is nevertheless much smaller than that of the aqueous humor. Therefore, we believe that our choice of gas density does not make any tangible difference in terms of interface shape.⁶ We note that the density of SO is much greater than that of gas. Also, the contact angle between SO, aqueous, and retina is significantly smaller than in the case of the interface between gas and aqueous. Thus, we expect the interface shape in the two cases to be substantially different.

Table 1. Mechanical properties of fluids. Density and surface tension properties are taken from Eames *et al.*⁶ The contact angle values were obtained by averaging the values proposed by Joussem, Wong⁸ and Fawcett *et al.*⁵ (See also Table 1 in Eames *et al.*⁶)

	Density (kg/m ³)	Surface tension with aqueous (N/m)	Contact angle with the retina (deg)
SO (Oxane 1300)	980	0.044	16.17 ± 1.23
Gas	1.225	0.07	30.74 ± 4.24
Aqueous humor	1000	-	-

2.2 Description of the model

The shape of the interface is computed numerically using the VOF method. The basic principle of this method is to introduce an additional function that provides the volume fraction of the tracked phase in the computational cell. This function is equal to one when the cell is entirely occupied by one fluid, vanishes when it is entirely occupied by the other fluid, and assumes an intermediate value when the cell contains the interface. An additional equation for such a function is introduced, which imposes that this function moves together with the fluid (its material derivative is equal to zero). The VOF method is known to provide a simple and economical way of tracking an interface between two fluids in 3D.^{9,10} Numerical simulations are performed using the free software OpenFOAM.¹¹ All meshes are generated using the *snappyHexMesh* tool by OpenFOAM, which produces unstructured meshes consisting of tetragonal and hexahedral volumes. We perform fully 3D simulations using meshes consisting on average of 1.7 million volumes, and run the code in parallel on a 32-processor computer and, for some cases, at the HPC center CINECA, in Italy. Careful mesh-independence tests have been carried out for all simulations. The numerical simulations are run by fixing the volume ratio (ratio of the volume of the injected tamponade fluid to the total volume of the domain) and setting an initially flat and horizontal shape of the interface. Advancing in time, the interface evolves towards its equilibrium shape; when a steady solution is obtained, the simulation ends. As noted in the previous section, viscosity does not affect the final configuration reached by the interface. However, it obviously affects the transient phase of the computation before a steady state is reached. If the viscosity of the two fluids is very large, convergence is obtained over long times. On the other hand, in the case of low viscosity, waves may form on the interface that can lead to numerical instabilities. In the course of the simulations, the values of the viscosity of the two fluids were tuned in order to optimize numerical efficiency.

2.3 Model geometry

2.3.1 Idealized realistic eye shapes

We first consider idealized, yet realistic shapes of the vitreous chamber in phakic eyes. The geometry is constructed on the basis of data from Atchison *et al.*¹² The resulting vitreous chamber domain for an emmetropic eye is shown in Figure 1a on a vertical cross-section of symmetry. The domain is axisymmetric with respect to the horizontal axis that passes through the center of the lens. Geometries representing myopic eyes are constructed using data reported by Atchison *et al.*¹³ (see Table 1 of their paper), by stretching the emmetropic eye shape in all directions. However, for simplicity, we maintain the domain axisymmetric, thus imposing that the inferior-superior and nasal-temporal lengths of the vitreous chamber are equal to each other (averaging the values reported by Atchison *et al.*¹³ for such lengths). In fact, according to Table 1 in the authors' paper, the differences between these two lengths are very small.

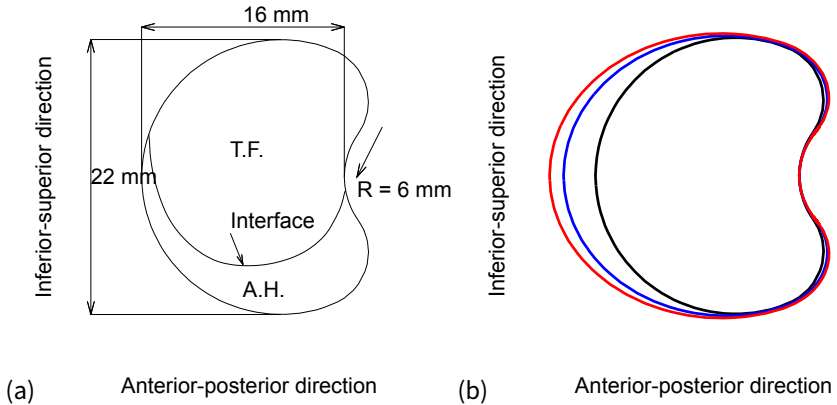


*Fig. 1. (a) Vertical symmetry cross-section of the domain for an emmetropic eye. The domain is filled with two immiscible fluids: the tamponade fluid (T.F.) and the aqueous humor (A.H.). All geometrical measurements are taken from Atchison *et al.*¹² (b) Vertical cross-sections of myopic eyes. The domains have been obtained by stretching the shape of the emmetropic eye in all directions, according to Atchison *et al.*¹³ In the figure, the black line corresponds to the normal eye; blue line refers to myopic eyes with an axial length of 25.5 mm, height and width of 22.3 mm; and red line to an axial length of 26.6 mm, height and width of 22.85 mm.*

Various myopic eye shapes reconstructed in this way are shown in Figure 1b, corresponding to different axial lengths of the eye, where, following Atchison *et al.*,¹³ the axial length is defined as the distance between the anterior cornea and retinal pole. Obviously, real eyes show far greater complexity in shapes than what is considered in this section. However, adopting idealized yet realistic geometries allows us to draw general conclusions. The case of a real eye shape is also considered in this work, with the purpose of showing that the present mathematical model is also applicable in such cases.

2.3.2 Real reconstructed eye shapes

Retinal contours of real eyes were obtained from high-resolution MR-images, which were semi-automatically segmented, as described by Beenakker *et al.*^{14,15} In short, ocular MR-measurements were performed on a Philips Achieva 7 Tesla (Best, The Netherlands) whole body magnet using a custom-made receive eye coil.¹⁴ The images were acquired using a 3D inversion recovery turbo gradient echo technique with an inversion time of 1280 ms, a shot interval of 3 s, and a turbo field echo factor of 92. The MR sequence parameters for repetition time (TR)/echo time (TE)/flip angles were: 2.5 ms/4.55 ms/16°. A cued-blinking protocol was used to minimize eye-motion artifacts.¹⁶ The scan resulted in a spatial resolution of $0.5 \times 1.0 \text{ mm}^3$ and the scan time was slightly less than three minutes.

The MR-images were subsequently segmented semi-automatically by in-house developed software, based on the rapid-prototyping platform MevisLab (Fraunhofer

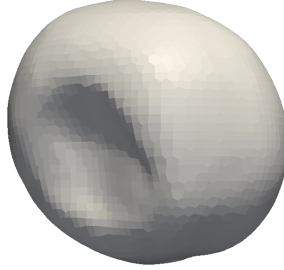


Fig. 2. Reconstructed shape of the vitreous body of an emmetropic eye from MR-images.

MeVis, Bremen, Germany). The central axis, the MR equivalent of the optical axis, was defined as the line from the center of the lens to the center of the vitreous body. A previous study on the reliability of the technique showed good agreement with partial coherence interferometry with a mean difference of 0.08 mm between the segmented MR-data and biometry.¹⁵ The study protocol was performed in accordance with the Declaration of Helsinki and was approved by the medical ethical committee of the Leiden University Medical Center. Informed consent was obtained from all participants.

2.4 Model validation

In order to validate the numerical model, we compared the numerical results with predictions of an in-house written code able to predict the shape of the interface between two fluids within a spherical domain. This is the problem considered in Eames *et al.*⁶ Owing to the axisymmetry of the sphere, the problem reduces to compute the shape of a curve, which is the intersection of the interface with a vertical plane across the axis of symmetry.

Mathematically this problem is governed by a system of ordinary differential equations derived from the Laplace-Young law.⁷ The Laplace-Young equation is given by:

$$2k_m = \frac{\Delta\rho g}{\gamma} x_I + B, \quad (1)$$

where k_m is the local mean curvature of the interface between the two fluids, $\Delta\rho = \rho_2 - \rho_1$ is the density difference, g is the acceleration of gravity, γ is the surface tension between two fluids, and $x_I(y)$ is the function describing the shape of the interface (see Fig. 3 for the coordinate system). Finally, B is a constant that, adopting the system of coordinates depicted in Figure 3, represents the mean curvature at the origin. The local mean curvature of the interface can be evaluated as:

$$2k_m = -\nabla \cdot \mathbf{n}, \quad (2)$$

where \mathbf{n} is the normal to the surface.

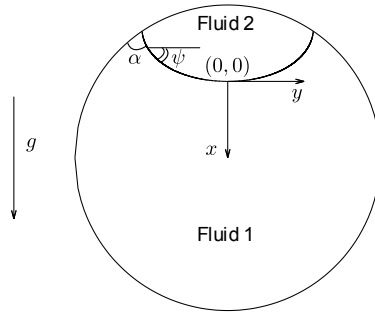


Fig. 3. Cross-section of the spherical domain with two superposed fluids. The origin is placed in the lowest point of the interface between fluids. The governing system of ordinary differential equations is given in terms of the slope angle ψ in the interval $[0, \alpha]$, with α being a contact angle.

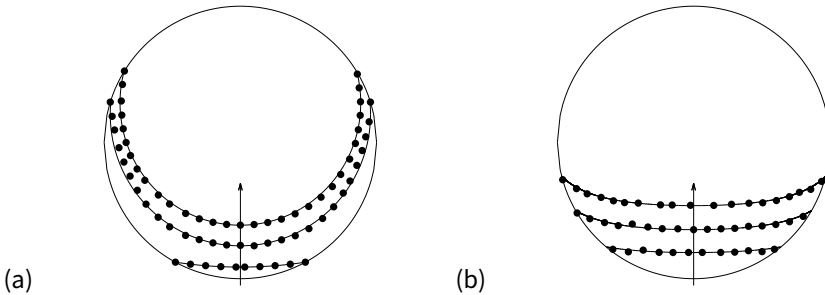


Fig. 4. Equilibrium shape of the interface in the spherical domain from the analytical solution (solid lines) and from the numerical model (dots) for different volume fractions of tamponade fluid ($V_{T.F.}/V = 0.65, 0.7, 0.8$). (a) SO, (b) gas. The arrow indicates decreasing values of $V_{T.F.}/V$.

Since the function $x_I(y)$ can assume two values for a given y , it is convenient to use a parametric representation of the function, defining the position of the interface in terms of the slope angle ψ shown in Figure 3, so that we can write:

$$x = x(\psi), \quad y = y(\psi). \quad (3)$$

It is easy to show that the problem is governed by the following system of two ordinary differential equations:

$$\frac{dx}{d\psi} = \frac{\sin \psi}{Q}, \quad (4a)$$

$$\frac{dy}{d\psi} = -\frac{\cos \psi}{Q}, \quad (4b)$$

with $Q = \frac{\sin \psi}{y} - \frac{\Delta \rho}{\gamma} x - B$, which we solve subjected to the boundary conditions:

$$x(0) = 0; \quad y(0) = 0. \quad (5)$$

The value of the mean curvature at the origin B is unknown; thus, we iterate the integration of the above equations until the value of ψ in correspondence of the wall equals the sought value of the contact angle. The iteration procedure is based on the bisection method.

In Figure 4 we plot the shape of the interface on a cross-section of the sphere. The radius of the sphere is equal to 0.01 m. The solid line is obtained with the axisymmetric numerical model described above, whereas dots are relative to the fully 3D numerical solution obtained with the VOF method. Figure 4a refers to the case of aqueous-SO interface and Figure 4b to the gas-aqueous interface. In both cases, the fluid below the interface is aqueous humor. The different curves correspond to different volume ratios of the tamponade fluid. In all cases the results from the two approaches are in very good agreement. The maximum difference between the fully 3D solution and the numerical model, normalized with the sphere radius, is $\approx 5 \times 10^{-5}$. This confirms the suitability of the VOF method for the purposes of this work.

3. Results

3.1 Emmetropic eyes

We first consider the case of emmetropic eyes and refer to the idealized eye shape reported in Figure 1a. Various equilibrium configurations of the interface are shown in Figure 5.

Each curve corresponds to a different degree of filling of the vitreous chamber by the tamponade fluid. Figures 5a and b are relative to the case of SO, while Figures 5c and d to the case of gas. In Figure 6 we also show 3D views of the interface, obtained with a filling ratio $V_{T.F.}/V = 0.85$, where $V_{T.F.}$ denotes the volume of the tamponade fluid and V the total volume of the vitreous chamber.

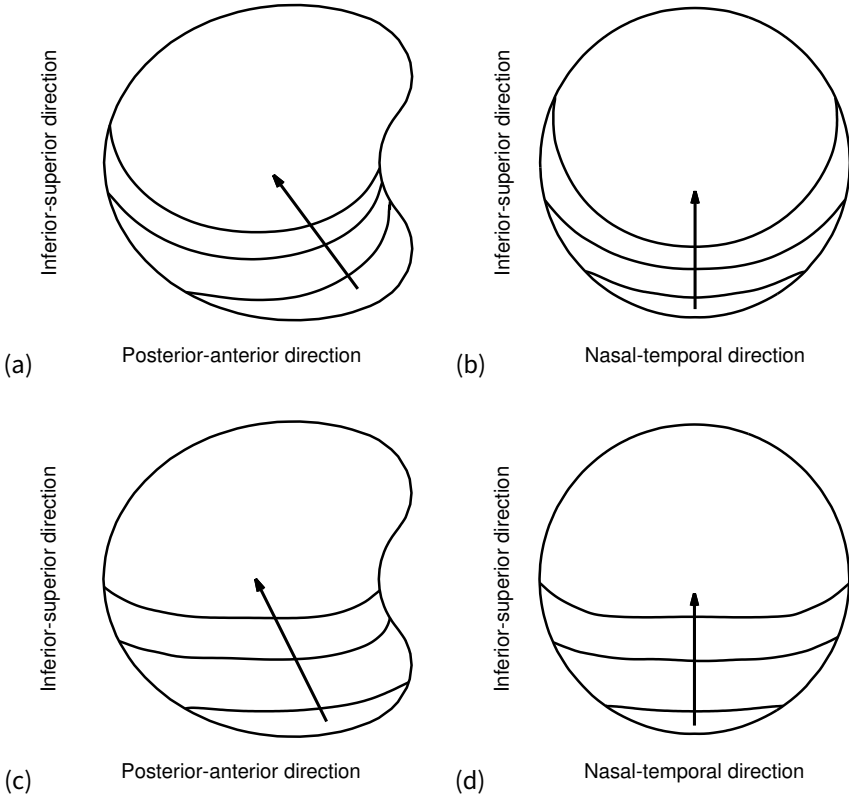


Fig. 5. Equilibrium shape of the interface in the normal eye for the SO (a,b) and gas (c,d). For both cases we consider three different degrees of filling ($V_{T.F.}/V = 0.60, 0.75, 0.90$). The arrows indicate decreasing values of $V_{T.F.}/V$.

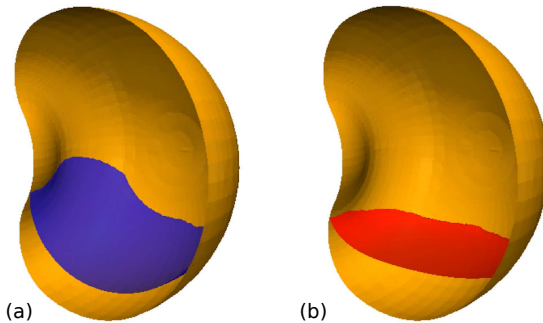


Fig. 6. Three-dimensional views of the interface shape: (a) SO and (b) gas. The degree of filling $V_{T.F.}/V$ is 0.85 in both cases.

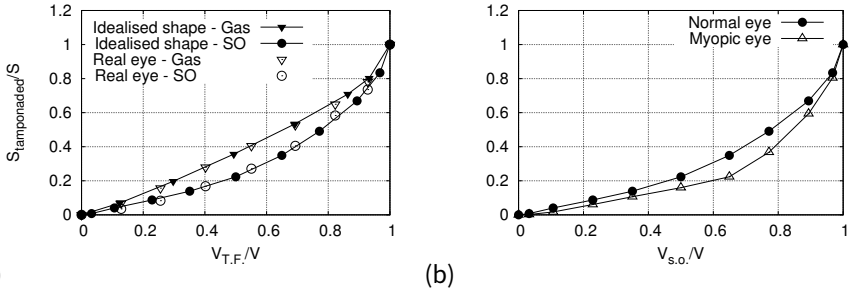


Fig. 7. (a) Relative tamponated surface as a function of the volume fraction for the case of SO and gas. Solid symbols refer to the idealized shapes of the vitreous chamber and open symbols to a real, reconstructed eye. (b) Relative tamponated surface as a function of the volume fraction for an emmetropic and a highly myopic eye, in the case of SO. The axial length of the myopic eye is equal to 24.6 mm.

In Figure 6 we report the equilibrium shape of the interface for both SO (a) and intraocular gas (b). The equilibrium shape of the interface is significantly different with respect to that in a sphere. This is most evident looking at the anterior-posterior cross-sections (Figs. 5a,c). The indentation produced by the lens induces a change in the concavity of the domain and has a strong effect on the interface shape. Specifically, the elevation reached by the interface in the front and back regions of the domain can be very different. Interestingly enough, the contact line is higher in the front of the eye than in the back for high degrees of filling, whereas the opposite happens when the filling degree is small (see in particular Fig. 5a). Comparing the case of SO to that of gas (Figs. 5a,b vs Figs. 5c,d), it appears that the interface is flatter in the case of gas; thus, gas has better tamponating properties than the SO. This is clearly shown in Figure 7a, where we plot the relative tamponated surface (*i.e.*, the ratio between the surface area in contact with the tamponade fluid $S_{tamponated}$ and the total bounding surface of the vitreous chamber S) as a function of the volume fraction $V_{T.F.}/V$.

The two curves refer to SO and gas, respectively. The curve corresponding to gas is invariably higher than that corresponding to SO. This implies that, for a given amount of tamponade fluid injected into the eye (a given ratio $V_{T.F.}/V$), the amount of surface tamponated by the gas is greater than that tamponated by the SO.

In Figure 8 we show the interface shape obtained in the case of a real emmetropic vitreous chamber reconstructed from MR-images, the geometry of which is shown in Figure 2. The degrees of filling correspond to those shown in Figure 5. In Figure 7a we also report, with open symbols, the results obtained for the case of the real eye. The model predictions for the idealized and real geometries are very close to one another. Also, in the case of the real geometry, the curves corresponding to SO and gas are clearly separated, with that relative to gas showing a larger amount of tamponated surface compared to SO. The results obviously depend on the specific eye chosen, and should be expected to change from subject to subject. However, the good match

between the real and idealized cases shown in Figure 8a indicates that the model is also robust when used in complex geometries.

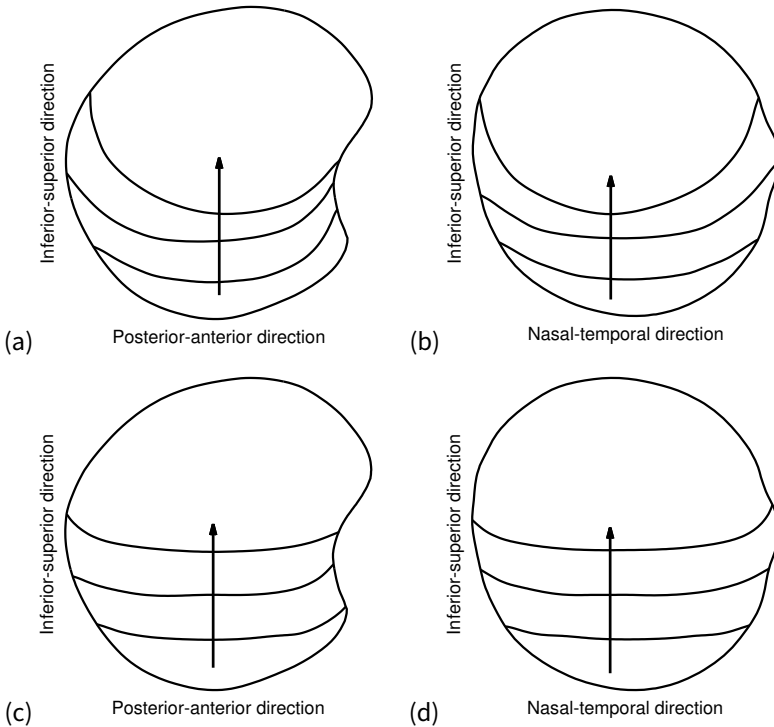


Fig. 8. Equilibrium shapes of the interface in the real eye domain for the SO (a,b) and gas (c,d). The degrees of filling are $V_{T.F.}/V = 0.6, 0.75, 0.9$. The arrows indicate decreasing values of $V_{T.F.}/V$.

In addition to the relative tamponated area, we also calculated the angular coverage of the retina. In this case we only considered the surface of the vitreous chamber covered by the retina. Following clinical practice, this is defined as the region posterior to a plane parallel to the equator of the eye and at a distance of 6 mm from the limbus in the antero-posterior direction (Figs. 1 and 9a). We then introduce the angles Ψ and Φ , shown in Figure 9, defined as follows: the angle Ψ is the angle of retinal coverage along an antero-posterior plane orthogonal to the equator (Fig. 9a); the angle Φ is the retinal coverage along the equatorial plane (Fig. 9b).

Comparisons of the tamponating properties of SOs and gases in terms of these angles are shown in Figure 10. Again, it appears that gas has better tamponating properties than SO.

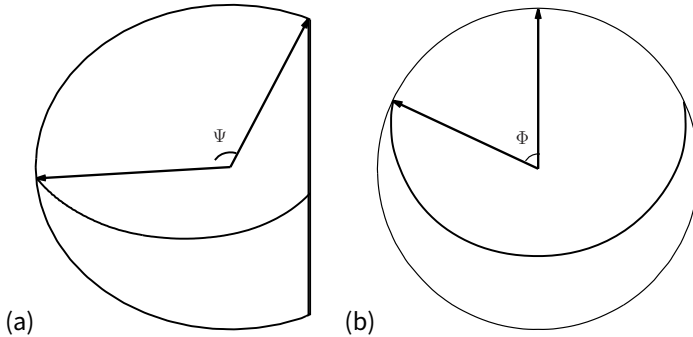


Fig. 9. Coverage angles Ψ and Φ . In (a) we show the way we measure the coverage angle Ψ on the antero-posterior cross-section; in (b), the angle Φ on the equatorial plane.

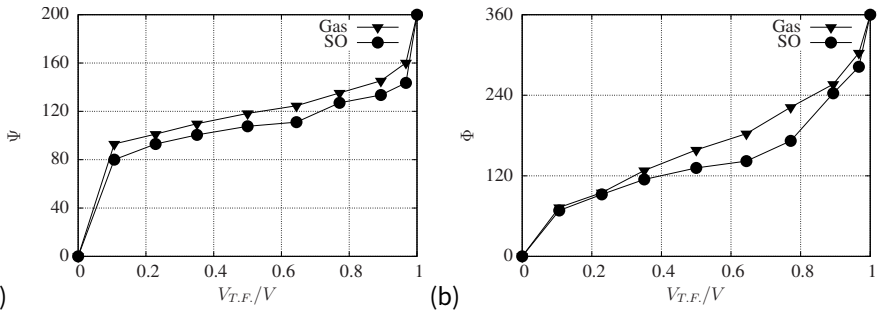


Fig. 10. Coverage angles Ψ (a) and Φ (b) in degrees vs the filling ratio $V_{T.F.}/V$ in the case of SO and gas.

3.2 Myopic eyes

We now show the results obtained in the case of myopic eyes and compare them to those found in emmetropic eyes. In Figure 11 we plot the equilibrium shape of the interface between SO and aqueous for the case of a myopic eye with an axial length of 26.6 mm. This figure is analogous to Figures 5a and b, *i.e.*, we consider three different volume fractions. In Figure 7b we plot the relative tamponated retinal area vs the filling ratio for the case of the emmetropic eye (same curve as in Fig. 7a for SO) and the corresponding curve for a highly myopic eye.

The figure shows that the tamponating effect of SO in the case of the myopic eye is smaller than in the emmetropic one. In fact, the relative tamponated surface $S_{tamponated}/S$ in the case of SO monotonically decreases with the axial length of the eye, as is shown in Figure 12 (solid circles). On the other hand, for the gas $S_{tamponated}/S$ remains approximately constant as the axial length of the eye is changed (open circles). This is also the case if a flat configuration of the interface between the tamponade fluid and the aqueous is assumed (solid squares in Fig. 12).

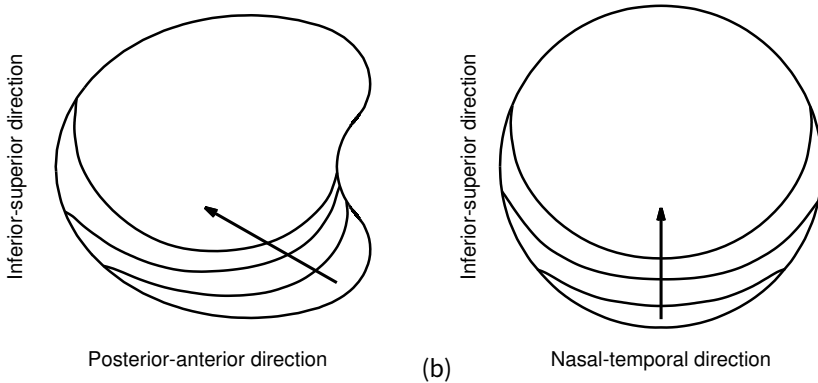


Fig. 11. Equilibrium shapes of the interface in a highly myopic eye for the case of SO. The axial length is 26.6 mm, the height and width are 22.75 mm. The arrows indicate decreasing values of $V_{T.F.}/V$ and the volume fractions are the same as in Fig. 4.

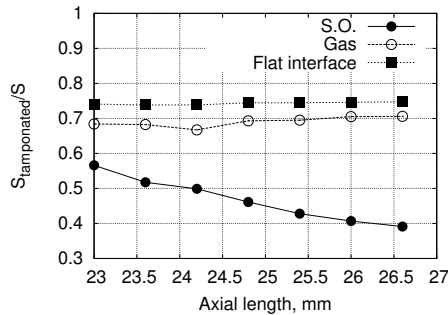


Fig. 12. Relative tamponated surface in the case of SO as a function of axial length. Filling ratio $V_{T.F.}/V = 0.81$.

4. Discussion

Tamponade compounds play an important role in the treatment of retinal detachment. In order to achieve the best possible tamponating effect, the surgeon attempts to fill the vitreous cavity completely with the endotamponades at the end of the surgery. However, under filling is always present due to the hydrophobic properties of the tamponade, which is also affected by the shape of the eyeball and the physical properties of the fluids (mainly their interfacial tension and density).¹⁷ Thus, the endotamponade is kept away from the retina in certain regions, leaving a variable angle of retina surface without any support. Considering that RBs are often multiple and localized in different quadrants of the retinal surface, it is important for the surgeon to have a better understanding of the shape of the vitreous substitute-aqueous interface, and hence, of its tamponating effect.

Hillier *et al.*¹⁸ investigated the influence of axial myopia on tamponade efficacy. The experiments were conducted *in vitro* using 19 mm and 25 mm spherical model chambers to mimic the vitreous cavity. The tamponating efficacy was estimated by measuring the maximum height of the bubble and the arc of contact subtended by the bubble. The authors reported no significant difference in tamponade efficacy according to the size of the eye chamber simulator. The limitation of such a remarkable experiment is mainly the assumption that the vitreous chamber is, in fact, spherical.

In our work, we employed a mathematical model and studied the tamponating effect of two different fluids used during vitrectomy: intraocular gas and SO. We note that the model is based on the solution of well-known equations and the results should be expected to be highly reliable. We considered idealized eye shapes and real eye geometries obtained from MR-images. In addition to this, we also considered idealized eyes with different degrees of myopia.

The results show that, for patients in the upright position, the geometry of the vitreous chamber has a significant impact on the final equilibrium configuration of the interface between the two fluids. This is because the interface intersects the anterior region of the vitreous chamber, where the indentation produced by the lens induces a significant change in the curvature of the vitreous chamber wall. Gas showed better tamponating properties than SO. This is due to two combined effects. First, the contact angle is smaller in the case of SO; second, the density difference is much higher in the case of gas (see Table 1). As a result, the interface with the aqueous is flatter in the case of gas than in the case of SO. The results obtained in the case of a real eye shape reconstructed from MR-images are very close to those obtained in the idealized case.

We also found that, for a given volume fraction of tamponade, the tamponating efficacy of SO is reduced in highly myopic eyes, whereas it remains approximately constant for a gas. This result for SO is interesting and counterintuitive, since one would expect that, in a larger domain (as is the case for a highly myopic eye), the interface should be flatter, thus providing a better tamponating effect. In fact, this is what happens in a spherical domain by increasing the radius, as we have verified with the in-house developed code described in section 2.4. For instance, in the case

of SO with a filling ratio of 0.80, the relative tamponated area grows almost linearly from ≈ 0.46 to ≈ 0.48 by increasing the sphere radius from 1.0 to 1.5 cm. The finding that, with SO in a myopic eye, the relative tamponated surface decreases with the axial length implies that, in this case, changes in eye shape play a more important role than changes in volume.

Patients who undergo vitrectomy for retinal detachment are asked to keep a certain head position for some time. Typically, after macular hole surgery they are asked to keep their face down because the hole is located in the posterior pole. Very often, however, retinal tears are located in the superior retina due to of gravitational traction forces induced by the vitreous body. In such cases, an upright position is required. In this paper we restricted our attention to this last case, but the method could be easily adopted to treat cases of different head orientations.

Finally, we note that this model can be a clinically valuable tool for eyes with pathological geometries, in which the resulting shape and position of the tamponade compound might differ significantly from the idealized eye shapes, whereby patient-specific evaluation is needed.

Acknowledgements

The present work was partially carried out at CINECA within the ISCR C project (HP10CSL8TA).

References

1. Scott JD. Prevention and perspective in retinal detachment. *Eye*, 1989;3(5): 491–515.
2. Romano MR, Das R, Groenwald C, Stappeler T, Marticorena J, Valldeperas X, et al. Primary 23-gauge sutureless vitrectomy for rhegmatogenous retinal detachment. *Indian journal of ophthalmology*, 2012;60(1): 29.
3. D'Amico DJ. Primary Retinal Detachment. *New England Journal of Medicine*, 2008;359(22): PMID: 19038880, 2346–2354. ISSN: 0028-4793. Visited on 02/14/2014, doi: 10.1056/NEJMcp0804591.
4. Oster SF, Mojana F, Bartsch D-UG, Goldbaum M, Freeman WR. Dynamics of the Macular Hole-Silicone Oil Tamponade Interface with Patient Positioning as Imaged by Spectral Domain Optical Coherence Tomography. *Retina (Philadelphia, Pa.)* 2010;30(6): 924.
5. Fawcett I, Williams R, Wong D. Contact angles of substances used for internal tamponade in retinal detachment surgery. *Graefe's archive for clinical and experimental ophthalmology*, 1994;232(7): 438–444.
6. Eames I, Angunawela RI, Aylward GW, Azarbadegan A. A theoretical model for predicting interfacial relationships of retinal tamponades. *Investigative ophthalmology & visual science*, Apr. 2010;51(4): PMID: 19933190, 2243–2247. ISSN: 1552-5783. doi: 10.1167/iovs.09-4442.
7. Pozrikidis C. *Fluid Dynamics: Theory, Computation, and Numerical Simulation*. Softcover reprint of hardcover 2nd ed. 2009. Springer, Nov. 2010; ISBN: 1441947191.
8. Jousen AM, Wong D. The concept of heavy tamponades—chances and limitations. *Graefe's Archive for Clinical and Experimental Ophthalmology*, 2008;246(9): 1217–1224.
9. Deshpande SS, Anumolu L, Trujillo MF. Evaluating the performance of the two-phase flow solver interFoam. *Computational science & discovery*, 2012;5(1): 014016.

10. Hirt CW, Nichols BD. Volume of fluid (VOF) method for the dynamics of free boundaries. *Journal of computational physics*, 1981;39(1): 201–225.
11. OpenFOAM, the Open Source CFD Toolbox by OpenCFD Ltd., Web site available at <http://openfoam.com>.
12. Atchison DA. *Optics of the Human Eye*. Elsevier, 2000;
13. Atchison DA, Jones CE, Schmid KL, Pritchard N, Pope JM, Strugnell WE, et al. Eye Shape in Emmetropia and Myopia. *Investigative Ophthalmology & Visual Science*, Oct. 2004;45(10): 3380–3386. doi: 10.1167/iov.04-0292.
14. Beenakker J, Rijn G, Luyten G, Webb A. High-resolution MRI of uveal melanoma using a microcoil phased array at 7 T. *NMR in Biomedicine*, 2013;26(12): 1864–1869.
15. Beenakker J-WM, Shamonin DP, Webb AG, Luyten GP, Stoel BC. Automated retinal topographic maps measured with magnetic resonance imaging retinal topographic maps measured with MRI. *Investigative ophthalmology & visual science*, 2015;56(2): 1033–1039.
16. Berkowitz BA. MRI of retinal and optic nerve physiology. *NMR in Biomedicine*, 2008;21(9): 927–927.
17. Wong D, Van Meurs J, Stappler T, Groenewald C, Pearce I, McGalliard J, et al. A pilot study on the use of a perfluorohexyloctane/silicone oil solution as a heavier than water internal tamponade agent. *British Journal of Ophthalmology*, 2005;89(6): 662–665.
18. Hillier RJ, Stappler T, Williams RL, Turner GS, Wong D. The impact of axial length on retinal tamponade for gas, silicone oil, and heavy silicone oil, using an in vitro model. *Graefes's Archive for Clinical and Experimental Ophthalmology*, 2011;249(5): 671–675.



Correlation and agreement between the 24-hour diurnal tension curve, the water-drinking test, and the postural-change test in glaucoma patients*

Fauze A. Goncalves, Fernando Henrique R. Amorim, Camila S. Zangalli, José Paulo C. Vasconcellos, Vital P. Costa

Department of Ophthalmology and Otorhinolaryngology, University of Campinas, Campinas, São Paulo, Brazil

Abstract

Aim: To investigate whether the water-drinking test (WDT) and the postural-change test (PCT) can predict the 24-hour diurnal tensional curve (DTC) intraocular pressure (IOP) peak and fluctuation by assessing the correlation and agreement between these three tests in medically treated primary open-angle glaucoma (POAG) patients.

Methods: 18 POAG patients underwent the DTC, WDT, and PCT. Pearson's correlation coefficient and Bland-Altman plots were used to assess the correlation and agreement between the results, respectively.

Results: Mean DTC IOP peak was 18.72 ± 4.31 mmHg and mean DTC IOP fluctuation was 7.00 ± 2.54 mmHg. The IOP peak was outside office hours in 50% of the subjects. We observed poor correlations between the DTC and WDT fluctuations, and the DTC and PCT fluctuations ($r = -0.125$, $P = 0.619$; $r = 0.349$, $P = 0.155$, respectively). There was a moderate positive correlation between the DTC and WDT peaks ($r = 0.493$, $P = 0.03$) and a strong positive correlation between the DTC and PCT peaks ($r = 0.722$, $P < 0.001$). However, Bland-Altman plots demonstrated poor agreement among IOP peaks and fluctuations between the three tests. WDT and DTC IOP peaks differed by

*The water-drinking test and the postural-change test should be used with caution to estimate peak IOP.

Correspondence: Vital P. Costa MD, Department of Ophthalmology and Otorhinolaryngology, University of Campinas, Av. Higienópolis, 1074 apto. 121, São Paulo, SP 01238-000, Brazil E-mail: vp.costa@uol.com.br

2 mmHg or more in 56% of the measurements. PCT and DTC IOP peaks showed that 83% of the measurements had differences greater than 2 mmHg.

Conclusions: Despite moderate to strong correlations between DCT and WDT peaks and DTC and PCT IOP peaks, the agreement was generally poor, suggesting that they should be used with caution to estimate peak IOP.

Keywords: intraocular pressure (IOP), water/drinking test (WDT), diurnal IOP, postural-change test (PCT)

1. Introduction

Intraocular pressure (IOP) is the main risk factor for the development and progression of glaucoma.¹ IOP is not constant throughout the day, with nocturnal IOP in the supine position being higher than diurnal IOP in the sitting position.²⁻⁵ Both peak IOP and diurnal IOP fluctuation have been reported to be risk factors for the development and progression of the disease.^{6,7}

IOP peaks have been related to the progression of visual field defects, but 30-50% of patients may not have their IOP peak detected during routine office hours,⁷⁻¹⁰ thus emphasizing the value of 24-hour IOP monitoring in the management of glaucoma patients.^{5,11} The 24-hour diurnal tensional curve (DTC) in the habitual position, which includes IOP measurements every three hours in the sitting (during the day) and supine positions (at night), is the gold standard method used to determine peak IOP and IOP fluctuation. However, the DTC may be inconvenient and troublesome for both patients and doctors, since it generally demands hospital admission.

Several methods have been designed to predict peak IOP and diurnal IOP fluctuation. The water-drinking test (WDT) is a provocative test designed to estimate the outflow facility reserve of the eye.^{10,12} It was first used as a tool for glaucoma diagnosis, and subsequently to estimate the severity and risk of progression in glaucoma patients.⁹ It has been suggested that the WDT is capable of predicting IOP peak during the DTC.^{5,8,9,12-15}

The postural-change test (PCT) evaluates the IOP increase that follows a shift from upright to horizontal position,^{5,16,17} possibly due to choroidal congestion and episcleral venous hypertension.^{16,17} It has been suggested that this test reproduces the physiological increase in IOP observed during the night in the supine position.^{17,18} The IOP increase in the PCT has been reported to be around 4.6 ± 2.6 mmHg.⁵

A number of previous studies have investigated the correlation between IOP peaks measured with the DTC, the WDT and the PCT,^{6,9,14} others have evaluated the agreement between modified DTCs and the alternative tests,^{11,16} but none have actually analyzed the agreement between these measurements and a complete 24-hour DTC. The purpose of this study was to investigate whether the WDT and PCT can in fact predict the 24-hour DTC peak and fluctuation by assessing the

agreement between these three tests in medically treated primary open-angle glaucoma (POAG) patients.

2. Methods

The study was approved by the Ethics Committee of the State University of Campinas and adhered to the tenets of the Declaration of Helsinki. Between September and November 2014, 18 consecutive medically treated POAG patients, who were followed at the Glaucoma Service of the University of Campinas, Brazil, were recruited. Written informed consent was obtained from each participant.

Individuals with POAG were defined as having a history of IOP ≥ 21 mmHg in three distinct visits before the onset of treatment, open angle at gonioscopy, abnormal optic discs with signs of glaucomatous neuropathy, and repeatable abnormal visual fields with typical glaucomatous defects, determined by Anderson's criteria.¹⁹ Glaucomatous optic neuropathy was defined as the presence of at least two of the following characteristics: a localized optic disc neuroretinal rim defect, cup-to-disc ratio (C/D) > 0.6 , disc hemorrhage, peripapillary nerve fiber layer defect, or cup asymmetry between the eyes of 0.2 or more. Patients with early glaucomatous changes, defined as mean deviation (MD) > -6 dB in at least one eye, and patients using up to two hypotensive medications were eligible for this study.

Individuals who had undergone previous intraocular surgery (except for uneventful phacoemulsification) or laser procedures, or those with a history of angle-closure glaucoma, secondary glaucoma, trauma, or eye inflammation were not included in this study. Women who were pregnant or breastfeeding were also excluded.

Each patient underwent a complete ophthalmologic examination, which included best-corrected visual acuity (BCVA), slit lamp biomicroscopy, Goldmann applanation tonometry, gonioscopy, dilated fundus examination, and automated achromatic perimetry (24-2 program, SITA Standard Strategy, Humphrey Field Analyzer 740, Zeiss, Dublin, CA, USA).

Patients were then admitted to the Ophthalmology Infirmary at the Hospital de Clinicas of the University of Campinas. They were told to keep using their medication drops at the same routine hours.

2.1. Diurnal tensional curve (DTC)

During the DTC, IOP measurements were recorded with a Goldmann applanation tonometer (GAT; Haag Streit, Koeniz, Switzerland) every three hours in the sitting position during daytime (from 9 AM to 9 PM), and in the supine position with a Perkins tonometer (Haag Streit, Koeniz, Switzerland) during the nocturnal period (from midnight to 6 AM). All measurements began at 3 PM. IOP was measured by one of two experienced ophthalmologists. Both the GAT and Perkins tonometers were

calibrated and tested to produce reliable measurements. Peak IOP was defined as the highest IOP measured over the 24-hour period, whereas IOP fluctuation was defined as the difference between the highest and lowest IOP measured over the 24-hour period.

2.2. Water-drinking test (WDT)

The WDT was performed while patients were hospitalized, beginning right after they had their last IOP measurement recorded for the DTC at noon. Subjects were asked to drink 1 L of water in 5 minutes, and IOP measurements were made every 15 minutes for 1 hour thereafter with GAT. The WDT peak was defined as the highest IOP measured during the test, and the WDT fluctuation was defined as the difference between the WDT peak and IOP at the beginning of the test. Patients were asked to fast for at least 4 hours before undergoing the WDT.

2.3. Postural-change test (PCT)

The PCT was also performed while patients were hospitalized. After the 9 AM measurement (in the sitting position), subjects were asked to go back to their room and remain in the supine position for 30 minutes. Measurements were then made with the Perkins tonometer. Postural IOP fluctuation was defined as the difference between IOP measurements in the sitting and supine positions.

2.4. Statistical analysis

The study was designed to have a power of 80% to detect an IOP difference of 2 mmHg between tests, considering a 2 mmHg standard deviation. The target sample size was 18 eyes (18 subjects). Only the right eye was selected for analysis. Statistical analysis was performed using platform R 3.0.1 (R Foundation for Statistical Computing, Vienna, Austria). Demographic and clinical data, including age, gender, height, weight, body mass index (BMI), central corneal thickness (CCT), mean deviation, and cup-to-disc ratio were tabulated.

IOP peak and IOP fluctuation in each test were compared using the paired Student's t-test. The Pearson correlation coefficient and Bland-Altman plot were used to determine the correlation and agreement between results, respectively. The Pearson correlation coefficient is a numerical value (r) that ranges from -1 (maximum negative correlation) to 1 (maximum positive correlation), where 0 represents no correlation. The correlation can be described as weak if r falls between 0.10 and 0.30, moderate if r is between 0.31 and 0.50, and strong if r is 0.51–1.00.²⁰ P values < 0.05 were considered statistically significant.

The Bland-Altman plot of agreement between two methods is determined using the differences between the values obtained by the two methods (y axis) vs the mean of the two measurements (x axis). The 95% limit of agreement, calculated as the mean difference \pm 1.96 standard deviation, provides an interval where 95% of the differences between measurements are expected to lie.²¹

Table 1. Baseline characteristics of all patients (n = 18)

Characteristic	Mean \pm SD
Age (years)	70.33 \pm 6.62
Sex	
Male	8
Female	10
BMI (Kg/m ²)	28.74 \pm 4.08
CCT (μ m)	537.33 \pm 12.47
MD (dB)	-5.6 \pm 4.67
Vert C/D	0.69 \pm 0.18
Baseline IOP (mmHg)	16.86 \pm 2.84
Medications (number)	1.22 \pm 0.80

MD: mean deviation BMI: body mass index C/D: cup-to-disc

3. Results

This was a prospective intervention study involving 18 POAG patients (18 eyes). Subject baseline characteristics are shown in Table 1. Baseline IOP was defined as the subjects' mean IOP in their last three visits.

3.1. DTC results

The mean DTC IOP was 14.88 \pm 3.34 mmHg, mean DTC IOP peak was 18.72 \pm 4.31 mmHg, and mean DTC fluctuation was 7.00 \pm 2.54 mmHg. The peak IOP occurred outside office hours (between 9 PM and 6 AM) in 50% (n = 9) of the subjects, with all of them occurring between midnight and 6 AM.

3.2. WDT results

The mean WDT peak was 19.0 \pm 4.56 mmHg and the mean WDT fluctuation was 5.11 \pm 2.76 mmHg. The mean DTC IOP peak and fluctuation were not significantly different from those measured by the WDT (P = 0.79 and P = 0.06, respectively).

3.3. PCT results

The mean PCT peak was 14.11 \pm 3.41 mmHg, and the mean PCT fluctuation was 0.61 \pm 1.72 mmHg. The mean DTC IOP peak and fluctuation were significantly different from those measured by the PCT (P < 0.001).

3.4. Interpretation

We observed poor correlations between the DTC and WDT fluctuations and the DTC and PCT fluctuations (r = -0.125, P = 0.619; and r = 0.349, P = 0.155, respectively).

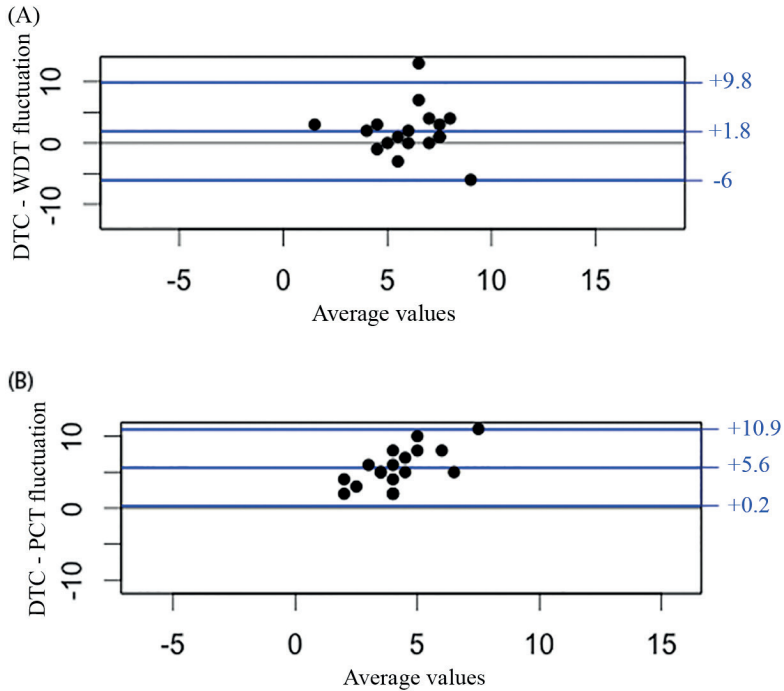


Fig. 1. Bland-Altman plots. Three lines are displayed. The thick line represents the mean difference of IOP fluctuation between the two tests. The upper and lower dash lines represent the 95% limit of agreement (± 1.96 SD). (A) Bland-Altman plot of DTC and WDT IOP fluctuation. (B) Bland-Altman plot of DTC and PCT IOP fluctuation.

The Bland-Altman plot comparing the WDT and PCT IOP fluctuations (Fig. 1A) shows that the mean IOP fluctuation difference between the two tests was 1.8 mmHg, and that the 95% limit of agreement between the two tests ranged from -6.0 to 9.8 mmHg. Fifty-percent of the eyes had IOP fluctuation differences greater than 2 mmHg. The Bland-Altman plot comparing the DTC and PCT IOP fluctuations (Fig. 1B) shows that the mean IOP fluctuation difference between the two tests was 5.6 mmHg, and that the 95% limit of agreement between the two tests ranged from 0.2 to 10.9 mmHg. IOP fluctuation differences were greater than 2 mmHg in 88.9% of the eyes.

There was a moderate positive correlation between the DTC and WDT peaks ($r=0.493$; $P = 0.03$, Fig. 2) and a strong positive correlation between the DTC and PCT peaks ($r = 0.722$; $P < 0.001$, Fig. 3). However, the Bland-Altman plots demonstrated poor agreement between the IOP peak measurements obtained with the three methods. The Bland-Altman plot comparing the DTC and WDT peaks (Fig. 4A) shows that the mean difference of peaks between the two tests was 0.2 mmHg,

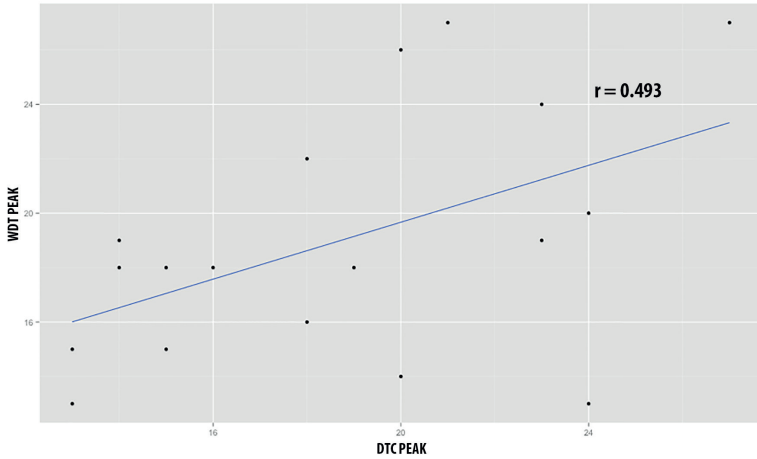


Fig. 2. Correlation between the DTC and WDT peaks.

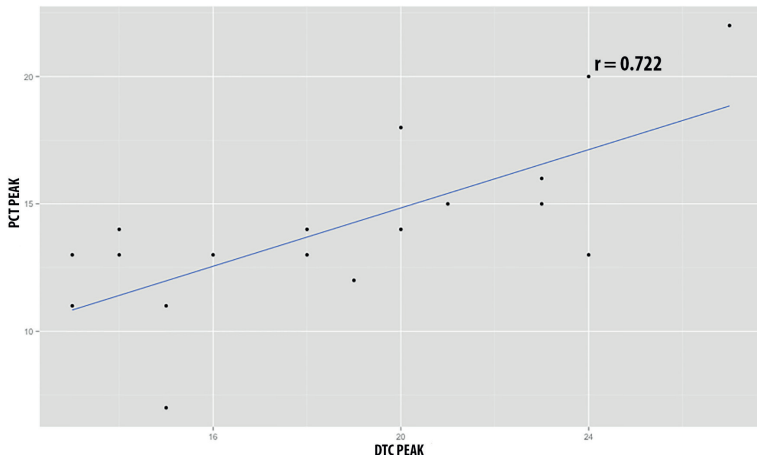


Fig. 3. Correlation between the DTC and PCT peaks.

and that the 95% limit of agreement between the two tests ranged from -9.2 to 8.6 mmHg. Furthermore, 56% of the measurements had IOP peak differences greater than 2 mmHg.

The Bland-Altman plot comparing the DTC and PCT IOP peaks (Fig. 4B) shows that the mean difference of peaks between the two tests was 4.61 mmHg, and that the 95% limit of agreement between the two tests ranged from -1.3 to 10.5 mmHg. Furthermore, 83% of the eyes had peak differences greater than 2 mmHg.

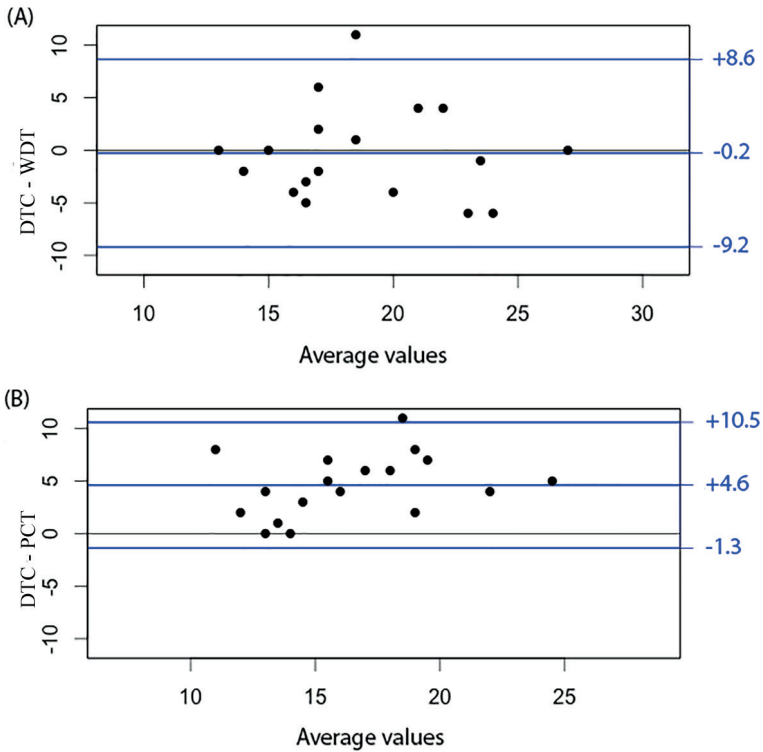


Fig. 4. (A) Bland-Altman plot of DTC and WDT IOP peaks. (B) Bland-Altman plot of the DTC and PCT IOP peaks.

4. Discussion

Mean IOP, peak IOP and IOP fluctuation are important risk factors for the development and progression of glaucoma.^{2,3,6} As mentioned before, the 24-hour DTC is the current gold standard to assess IOP characteristics throughout the day, but it is time-consuming and impractical. In fact, our study confirms that 50% of IOP peaks measured during the 24-hour DTC would not be detected during office hours. Attempts have been made to develop an alternative test capable of providing information regarding the behavior of IOP throughout the day, especially about IOP peak and fluctuations. However, most of the studies that compare IOP peak and fluctuation obtained with the DCT and the alternative methods rely on correlation, not agreement analysis.^{5,13,15,16}

The Pearson coefficient measures linear correlation rather than agreement. Methods can correlate well yet disagree greatly, as would occur if one method read

consistently higher than the other. Correlation typically depends on the range of the measures being assessed, with wider ranges often resulting in stronger correlations, but not as a consequence of better agreement between the methods.²¹

When the intention is to evaluate the agreement between two methods that measure the same quantity, it is important to properly use Bland-Altman plots, including the analysis of limits of agreement, and to comment on whether these limits are clinically acceptable. It is also important to assess two aspects of agreement: how well the methods agree on average and how well the measurements agree for individuals.²¹

The PCT is a provocative test that relies on the IOP change that occurs with modifications in both body and head positions. The majority of the available studies in the literature analyzed the difference in IOP values between the sitting and supine positions.^{4,18} It has been proposed that the immediate increase in IOP upon lying down may be due to a sudden increase in uveal blood flow, leading to increased aqueous production and also decreased trabecular outflow due to choroidal congestion and higher episcleral venous pressure.^{16,18} Few studies have attempted to evaluate the correlation and agreement between IOP peak and fluctuation measured during the DTC and PCT. Sakata *et al.*⁵ observed a moderate correlation between IOP peaks measured with the DCT and PCT ($r = 0.419$, $P = 0.001$), but no analysis of agreement was performed. Our study indicated a strong correlation between these measurements ($r = 0.722$), but poor agreement, evidenced by a mean difference of 4.61 mmHg between IOP peaks, a wide range of the 95% limit of agreement (11.8 mmHg), and 83% of the eyes showing IOP peak differences greater than 2 mmHg. Regarding IOP fluctuation, all tests showed poor correlation and agreement, which is probably due to the fact that baseline IOP measurements for the WDT and PCT do not correspond to the lowest IOP value of the DCT.

The WDT has clinical value as a stress test to evaluate the trabecular outflow facility. Previous studies have suggested that the WDT could be used in clinical practice to estimate 24-hour IOP behavior.^{5,8-10,12-15} Some have compared the mean IOP peaks obtained during the DTC and WDT.¹⁴ However, comparing means gives no information regarding individual values, which are essential to determine if there was agreement between the measurements. Other studies have shown strong correlations between the WDT and IOP peaks obtained with a modified DTC, which included IOP measurements during office hours.^{10,13,15} Vasconcelos-Moraes *et al.* found a strong correlation between the modified DCT and WDT IOP peaks ($r = 0.780$, $P < 0.0001$), but only 41% of these patients had IOP peak differences within 2 mmHg, which represents the repeatability coefficient for GAT.²² The Bland-Altman test confirmed a poor agreement, disclosing a wide 95% CI range (12.1 mmHg). However, it is well known that IOP measurements during office hours underestimate the IOP peak over 24 hours.^{11,23}

Finally, some authors have established strong correlations between the IOP peak obtained in the 24-hour DTC and the WDT,⁶ but none aimed at investigating the

agreement between the measurements. Sakata *et al.* performed a WDT and 24-hour DTC in 33 normal tension glaucoma patients, and found a moderate correlation ($r=0.422$) between the IOP peaks detected by both methods. Although the authors failed to perform a Bland-Altman analysis, they observed that 67% of the cases had IOP peak discrepancies that exceeded 2 mmHg, and suggested that “this rather disappointing ratio discourages estimating peak 24-hour DTC IOP by asking NTG patients to undergo a WDT”.⁵

In our study, we observed a moderate correlation ($r = 0.49$) between the IOP peaks obtained with the DTC and WDT. Although the mean DTC IOP peak was not significantly different from that measured by the WDT ($P = 0.79$), the Bland-Altman plot demonstrated wide limits of agreement (17.8 mmHg). Furthermore, peak IOP differences were larger than the clinically acceptable limit of 2 mmHg in 56% of the cases, confirming the findings described by Sakata *et al.*⁵ Another important feature of any test that intends to estimate peak IOP is its reproducibility. In a previous study, Medina *et al.* have demonstrated that the WDT performed at different times of the day shows poor reproducibility, which further limits its clinical use.²⁴

This study presents a few limitations. The sample size was relatively small, which can limit the generalization of some of our results. Although IOP measurements at night were made with the Perkins tonometer and daytime measurements were obtained with GAT, previous studies have demonstrated excellent agreement between their readings.²⁵ Finally, hospitalization may artificially modify IOP behavior in individuals. However, there is no objective method that allows measurement of IOP during the night without awakening patients. Furthermore, a newly developed 24-hour telemetric contact lens with an embedded sensor that allows undisturbed estimation of IOP in POAG patients at home corroborates the existing evidence regarding the circadian IOP pattern found in previous DTC studies.²⁶

To our knowledge, our study is the first to analyze not only the correlation, but also the agreement between a 24-hour DTC, the WDT and the PCT IOP peaks and fluctuations. Our findings suggest that while the DTC remains the gold standard method to assess IOP behavior, alternative tests such as the WDT and PCT, although more practical, should be used with caution to estimate peak IOP.

Funding Statement

This research received no specific grant from any funding agency in the public, commercial, or non-profit sectors.

Competing Interests Statement

The authors have no competing interests to disclose.

Contributorship Statement

Fauze Goncalves: Study conception and design; data acquisition and interpretation; article draft; final approval of the version to be published

Fernando Amorim: Study conception and design; data acquisition and interpretation; article draft; final approval of the version to be published

Camila Zangalli: Study design; data analysis and interpretation; article revision; final approval of the version to be published

Jose Vasconcellos: Study design; data analysis and interpretation; article revision; final approval of the version to be published

Vital Costa: Study design, data analysis and interpretation; article revision; final approval of the version to be published

References

1. Leske MC, Heijl A, Hyman L, et al. Factors for progression and glaucoma treatment: the Early Manifest Glaucoma Trial. *Curr Opin Ophthalmol* 2004;15(2):102-106. Available from: <http://content.wkhealth.com/linkback/openurl?sid=WKPTLP:landingpage&an=00055735-200404000-00008> doi: 10.1097/00055735-200404000-00008. [Google Scholar]
2. Gordon MO, Beiser JA, Brandt JD, et al. The Ocular Hypertension Treatment Study: baseline factors that predict the onset of primary open-angle glaucoma. *Arch Ophthalmol Chic Ill* 1960 2002;120(6):714. [Google Scholar]
3. The Advanced Glaucoma Intervention Study (AGIS), , 7 . The Advanced Glaucoma Intervention Study (AGIS): 7. The relationship between control of intraocular pressure and visual field deterioration.The AGIS Investigators.. *Am J Ophthalmol* 2000;130(4):429-440. Available from: <http://ClinicalTrials.gov/search/?term=11024415%20%5BPUBMED-IDS%5D> PubMed PMID: 11024415. [Google Scholar]
4. Krieglstein GK, Langham ME. Influence of Body Position on the Intraocular Pressure of Normal and Glaucomatous Eyes. *Ophthalmologica* 1975;171(2):132-145. Available from: <http://www.karger.com/doi/10.1159/000307479> PubMed PMID: 1153173. doi: 10.1159/000307479. [Google Scholar]
5. Sakata R, Aihara M, Murata H, Saito H, Iwase A, Yasuda N, et al. Intraocular pressure change over a habitual 24-hour period after changing posture or drinking water and related factors in normal tension glaucoma.. *Invest Ophthalmol Vis Sci* 2013 Aug;54(8):5313-5320. Available from: <http://www.diseaseinfosearch.org/result/3065> PubMed PMID: 23821194. doi: 10.1167/iovs.13-11792. [Google Scholar]
6. Gonzalez I, Pablo LE, Pueyo M, et al. Assessment of diurnal tensional curve in early glaucoma damage. *Int Ophthalmol*. 1996 1997;20(1-3):113-115. Available from: <http://www.diseaseinfosearch.org/result/3065> PubMed PMID: 9112174. [Google Scholar]
7. Asrani S, Zeimer R, Wilensky J, et al. Large diurnal fluctuations in intraocular pressure are an independent risk factor in patients with glaucoma. *J Glaucoma* 2000;9(2):134-2. Available from: <http://content.wkhealth.com/linkback/openurl?sid=WKPTLP:landingpage&an=00061198-200004000-00002> doi: 10.1097/00061198-200004000-00002. [Google Scholar]
8. Susanna R, Vessani RM, Sakata L, et al. The relation between intraocular pressure peak in the water drinking test and visual field progression in glaucoma. *Br J Ophthalmol* 2005;89(10):1298-1301. Available from: <http://bjo.bmj.com/cgi/pmidlookup?view=long&pmid=16170120> PubMed PMID: 16170120. doi: 10.1136/bjo.2005.070649. [Google Scholar]
9. Leydhecker W. The Water-Drinking Test. *British Journal of Ophthalmology* 1950 Aug;34(8):457-479. Available from: <http://bjo.bmj.com/cgi/doi/10.1136/bjo.34.8.457> doi: 10.1136/bjo.34.8.457. [Google Scholar]
10. De Moraes CGV, Furlanetto RL, Reis ASC, Vegini F, Cavalcanti NF, Susanna Jr R. Agreement between stress intraocular pressure and long-term intraocular pressure measurements in primary open

- angle glaucoma. *Clin Experiment Ophthalmol* 2009;37(3):270-274. Available from: <http://www.diseaseinfosearch.org/result/3065> PubMed PMID: 19472536. doi: 10.1111/j.1442-9071.2009.02003.x. [Google Scholar]
11. Costa VP, Jimenez-Roman J, Carrasco FG, et al. Twenty-four-hour ocular perfusion pressure in primary open-angle glaucoma. *Br J Ophthalmol* 2010 Oct;94(10):1291-1294. Available from: <http://bjo.bmj.com/cgi/doi/10.1136/bjo.2009.167569> doi: 10.1136/bjo.2009.167569. [Google Scholar]
 12. De_Moraes CGV, Susanna R, Ritch R. The water drinking test. *Am J Ophthalmol*. 2011 Mar;151(3):559-560 2011;151(3):559. [Google Scholar]
 13. Kumar RS, Guzman, M.H.P. de , Ong PY, et al. Does peak intraocular pressure measured by water drinking test reflect peak circadian levels? A pilot study. *Clin Experiment Ophthalmol* 2008;36(4):312-315. Available from: <http://doi.wiley.com/10.1111/j.1442-9071.2008.01765.x> doi: 10.1111/j.1442-9071.2008.01765.x. [Google Scholar]
 14. Caiado RR, Badaró E, Kasahara N. Intraocular pressure fluctuation in healthy and glaucomatous eyes: a comparative analysis between diurnal curves in supine and sitting positions and the water drinking test.. *Arq Bras Oftalmol* 2014 Sep;77(5):288-292. Available from: http://www.scielo.br/scielo.php?script=sci_arttext&pid=S0004-27492014000500288&lng=en&nrm=iso&tlng=en PubMed PMID: 25494373. [Google Scholar]
 15. Vasconcelos-Moraes CG, Susanna R. Correlation between the water drinking test and modified diurnal tension curve in untreated glaucomatous eyes. *Clin São Paulo Braz* 2008;63(4):433-436. Available from: http://www.scielo.br/scielo.php?script=sci_arttext&pid=S1807-59322008000400004&lng=en&nrm=iso&tlng=en PubMed PMID: 18719751. [Google Scholar]
 16. Kiuchi T, Motoyama Y, Oshika T. Postural response of intraocular pressure and visual field damage in patients with untreated normal-tension glaucoma.. *J Glaucoma* 2010;19(3):191-193. Available from: <http://www.diseaseinfosearch.org/result/3065> PubMed PMID: 19528820. doi: 10.1097/IJG.0b013e3181a98f30. [Google Scholar]
 17. Leonard TJ, Muir MGK, Kirkby GR, et al. Ocular hypertension and posture. *Br J Ophthalmol* 1983 Jun;67(6):362-366. Available from: <http://bjo.bmj.com/cgi/doi/10.1136/bjo.67.6.362> doi: 10.1136/bjo.67.6.362. [Google Scholar]
 18. Kothe AC. The effect of posture on intraocular pressure and pulsatile ocular blood flow in normal and glaucomatous eyes. *Surv Ophthalmol* 1994;38, Supplement. PubMed PMID: 7940143. [Google Scholar]
 19. Anderson DR, Patella VM. Automated static perimetry. Mosby Incorporated; 1999. [Google Scholar]
 20. Cohen J. Statistical power analysis for the behavioral sciences (rev. ed. Hillsdale, NJ, England: Lawrence Erlbaum Associates, Inc; 1977. [Google Scholar]
 21. Martin Bland J, , Altman D. STATISTICAL METHODS FOR ASSESSING AGREEMENT BETWEEN TWO METHODS OF CLINICAL MEASUREMENT. *The Lancet* 1986 Feb;327(8476):307-310. Available from: <http://linkinghub.elsevier.com/retrieve/pii/S0140673686908378> doi: 10.1016/S0140-6736(86)90837-8. [Google Scholar]
 22. Sudesh S, Moseley MJ, Thompson JR. Accuracy of Goldmann tonometry in clinical practice. *Acta Ophthalmol* (Copenh 1993;71(2):185-188. Available from: <http://doi.wiley.com/10.1111/j.1755-3768.1993.tb04988.x> doi: 10.1111/j.1755-3768.1993.tb04988.x. [Google Scholar]
 23. Cronemberger S, Silva, C.L.d. (Andréa) , Calixto N. Importance of intraocular pressure measurement at 6:00 a.m. in bed and in darkness in suspected and glaucomatous patients. *Arq. Bras. Oftalmol* 2010;73(4):346-349. Available from: http://www.scielo.br/scielo.php?script=sci_arttext&pid=S0004-27492010000400009&lng=en&nrm=iso&tlng=en doi: 10.1590/S0004-27492010000400009. [Google Scholar]
 24. Medina FMC, Rodrigues FKP, Pierre Filho, d.T.P. (Paulo) , Matsuo T, Vasconcellos, P.C.d. (José) , Costa VP. Reproducibility of water drinking test performed at different times of the day. *Arq. Bras. Oftalmol* 2009;72(3):283-290. Available from: http://www.scielo.br/scielo.php?script=sci_arttext&pid=S0004-27492009000300002&lng=en&nrm=iso&tlng=en doi: 10.1590/S0004-27492009000300002. [Google Scholar]

25. Arora R, Bellamy H, Austin M. Applanation tonometry: a comparison of the Perkins handheld and Goldmann slit lamp-mounted methods. *Clin Ophthalmol Auckl NZ* 2014;8:605-10. Available from: <http://dx.doi.org/10.2147/OPTH.S53544> PubMed PMID: 24707165. doi: 10.2147/OPTH.S53544. [Google Scholar]
26. Mansouri K, Shaarawy T. Continuous intraocular pressure monitoring with a wireless ocular telemetry sensor: initial clinical experience in patients with open angle glaucoma. *Br J Ophthalmol* 2011 May;95(5):627-629. Available from: <http://bjo.bmj.com/cgi/doi/10.1136/bjo.2010.192922> doi: 10.1136/bjo.2010.192922. [Google Scholar]



Blink characterization using curve fitting and clustering algorithms

Joseph K. Brosh¹, Ziwei Wu², Carolyn G. Begley², Tobin A. Driscoll¹, Richard J. Braun¹

¹Department of Mathematical Sciences, University of Delaware, Newark, USA, ²School of Optometry, Indiana University, Bloomington, USA

Abstract

Purpose: The motion of the upper eyelid during blinking can be important in diseases and syndromes that affect the eye; these include dry eye syndrome and blepharospasm, for example. We employ mathematical methods in this proof-of-concept study to classify blink motion.

Methods: Using data from a pilot study, hypothesized lid motion functions are fit to the dynamic position of the center of the upper lid under four experimentally controlled conditions. The coefficients of these non-linear fits are used with measured data to classify blinks. Agglomerative hierarchical and spectral clustering methods were used to attempt an automatic distinction between partial and full blinks as well as between normal and abnormal blinks.

Results: Results for both approaches are similar when the input data is suitably normalized. Clustering finds outlying blinks that do not fit the model functions for lid motion well and that differ from the majority of blinks in our sample of $N = 393$ blinks; however, those blinks may not be outliers based on easily observed data such as blink amplitude and duration.

Conclusion: This type of analysis has potential for classifying blink dynamics from normal and pathological conditions such as recovery from Bell's palsy or dry eye syndrome, but more work is needed with larger sets of data from blinks to put forth firm conclusions.

Keywords: hierarchical clustering, spectral clustering, blinking, blink classification, dry eye

Correspondence: R.J. Braun, Department of Mathematical Sciences, University of Delaware, Newark DE 19716, USA.

E-mail: rjbraun@udel.edu

1. Introduction

During a normal eye blink, the upper lid moves inferiorly during the down phase or downstroke, and during the subsequent up phase or upstroke a thin tear film is painted over the exposed corneal and conjunctival surfaces.^{1,2} The quality of the tear film left behind depends on many factors, including the speed of the lid,³ thickness of tears under the upper lid,⁴⁻⁶ total amount of tears present,⁷ lipid layer dynamics,⁸ and the motion of the lids themselves.^{1,9,10} The dynamics of the blink have a well-known connection to the visual demands, activity level, and mental state of the subject, and blink rate is known to be altered in pathological conditions such as dry eye syndrome (DES). Thus, there may be an interplay between the effectiveness of blinks and the development of DES.¹¹ Other conditions that are intimately related to blinking include blepharospasm.¹¹

Blinks have been categorized into three types: voluntary, reflex (*e.g.*, reactions) and spontaneous.^{2,12} In a classic paper on this topic, Evinger *et al.*¹² measured the kinetics of these types of blinks using a magnetic coil search technique and skin electrodes to record the activity of the muscles involved in the blink as the eyelid opened and closed. The two main muscles involved in blinking are the orbicularis oculi muscle, which acts to close the eyelid, and the levator palpebrae, which opens the eyelid during the blink. Evinger *et al.* suggested that these muscles were aided by their associated ligaments because they act in a spring-like fashion.¹² Kaminer *et al.*¹³ hypothesized that the spinal trigeminal complex plays an important role in modulating incoming neural signals to vary the blink pattern.

Blinks were also captured and analyzed by Doane¹ by filming subjects with a telephoto lens through a half-silvered mirror during the interval when the subjects believed they were relaxing before the test was to begin. He analyzed the motion of the upper lid margin by manually capturing the location in each frame and then collecting the results. He found that most blinks were partial, and that, typically, after a few partial blinks, there was a full blink. Though we often think of a full blink as when the upper and lower lids meet, it may be that most full blinks have the lids approaching each other but not necessarily touching.^{14,15} It has been found via mathematical models that the lids need not touch for the fluid motion to "reset" and for there to be what is effectively a complete blink.^{5,16}

A number of other studies have shown that the blink rate (BR) or interblink interval (IBI) can be affected by many factors. Reading, working on computer, or other visual tasks requiring concentration are known to decrease blink frequency,¹⁷⁻²⁰ whereas irritation or stimulation of the ocular surface increases the BR.²¹⁻²³ DES is associated with an increased BR^{19,23} presumably due to the ocular surface irritation and stress provided by surface drying or increased hyperosmolarity from an unstable tear film.^{24,25}

Other ocular conditions are related to blinking as well. Subjects recovering from Bell's palsy, a unilateral weakening (or sometimes paralysis) of the peripheral facial muscles, can strongly affect blinking and lead to inflammation and even functional

blindness; after one year of recovery, orbicularis oculi activity may normalize but blink amplitude may remain decreased.²⁶ Blepharospasm can cause rapid and involuntary blinking;² perhaps this and other eye dystonia could be detected in a developing or less severe state so that most severe states could be avoided or limited. Grave's upper eyelid retraction has been said to have a paucity of data,² and more data with improved quantitative processing could aid understanding of this condition as well. In all of these cases, basic understanding could be aided by further quantification of blink processes.

Blinks occurring when the subject knows that he or she is being observed are not unconscious, but may still provide useful information. Tasks may be assigned to occupy the subjects during experiments, and this is done in the clinic either as a distraction or to study the dependence of blinks on the performed task^{2,22} and stimulus type.^{9,19,21} We use data from a recent pilot study by Wu *et al.*²² in ten test subjects, including normal and DES subjects, whose blinks were recorded for one minute as part of a 2.5 minute interval. The blinks were recorded with and without a light flow from a fan blowing on the subject's eye, in each case while working on either a high- or low-concentration task. The data was taken after an initial 30 s start up phase, and the blinks were measured by monitoring the location of a centrally-located spot located near the superior lid margin. The recorded blinks were preprocessed in order to identify the start and end of blinks for each subject. The IBI was measured as the time from the maximum lid displacement of one blink to the subsequent blink. They found that even the mild stimulus from air flow used on the surface of the eye decreased the IBI and its variability regardless of whether it was a high- or low- concentration task. The high-concentration task increased IBI and its variability, and thus had an opposite effect to external stimulus. Blink amplitude, defined as the percentage of a full blink achieved at the end of the down phase of lid motion, had no significant effect from either the stimulus or task. However, they observed that the majority of blinks were partial, in accord with previous studies.^{1,2,19} They also observed a difference in correlation between blink amplitude and maximum speed during the down phase depending on whether the subject was previously diagnosed with DES.

In another study by Wu *et al.*,²⁷ using ten normal test subjects and similar conditions, it was found that IBI regularity increased with increased flow rate from the fan providing increased surface stimulus, most likely as a protective measure. It was found that there was a roughly linear relationship between ocular surface stimulation and decrease in IBI. Because only normal subjects were used, it is possible that a different response could be present for subjects that have moderate to severe DES.

The first quantitative mathematical model of blinking of which the authors are aware was developed by Berke and Müller.^{28,29} They designed a function that closely mimicked the position of the central lid margin during a blink. The function represents the displacement inferiorly, $x(t)$, from the rest position of the upper lid through the duration of the blink using:

$$x(t) = a_0 t^2 \exp(-bt^2). \quad (1)$$

There are two constants, a_0 and b , which were chosen appropriately to fit the blink amplitude and duration. This function has been modified to describe lid motion in theoretical work on tear film dynamics and blink cycles.^{5,6,16} Similar functions have been implemented in theoretical models for tear film deposition for the aqueous layer alone^{4,30} and including the action of polar lipids.^{31–33} We shall modify this function in order to improve the fit for a wider variety of blink data, and to use those fits to classify blinks. We note that the lid motion function is not periodic in general³⁴ and the IBI depends on task and conditions;^{2,22} in any case, we wish to study individual blinks and so Equation (1) suffices.

The purpose of this study is to develop methods to use the coefficients from a modified version of Equation (1) together with measured blink data such as amplitude and duration so that outlying blinks can be identified. If this can be done, then there is the potential to apply the method to clinical conditions like DES and Bell's palsy, among others, to quantitatively assess blinking and its relation to the condition in question. This is certain to lead to a better basic scientific understanding of conditions involving blinking, and thus has the potential to improve approaches in the clinic. We now go on to describe the methods used, then proceed to results, and finally, discussion.

2. Methods

The experimental data and methods used in this work are published elsewhere,^{22,27} but for convenience we provide a brief description of them here. Then, we proceed to the mathematical approach.

2.1 Experimental measurements

For this paper, we studied $N = 393$ blinks pooled from five subjects in a recent pilot study by Wu *et al.*²² The experimental method discussion here is closely based on that in Wu *et al.*²² Video recordings at 250 frames per second were made of ten subjects in four conditions based on combinations of two tasks with or without a gently blowing fan. Both healthy and dry eye subjects were included in the study based on their responses to the Dry Eye Questionnaire.³⁵ Five subjects were chosen because they had what was judged to be the best data for lid position across all of their blinks; one subject was normal with the remaining four self-reporting dry eye symptoms. The observations were made in two different visits (one visit with a fan, one visit without). The tasks were either listening to music (low-concentration state) or playing a video game (high-concentration state). Each task lasted 2.5 min with a 15-min break between tasks. When in use, a small electronic fan was located 50 cm from the eye, resulting in a measured air speed of 1.34 mph (0.6 m/s) at the eye. This air speed is very gentle and is insufficient to move, for example, tree leaves. Subjects were seated behind a Zeiss biomicroscope system (8× magnification) with a custom-fitted camera used to record upper lid movement (Basler piA640-210 gm, Basler AG, Germany,

250 Hz). In order to track eyelid positions during blinking, a 2 mm diameter reflective white dot was centered on the margin of the right upper lid. During the visit with a fan, the recording was started one minute after the onset of air stimulus to allow subjects to become familiar with the stimulus. Only the right eye was tested and the left was held shut by the subject to ensure that stimulus from the ocular surface arose from the tested eye. Other data was collected,²² but was not used in this work.

The observed upper lid positions were processed as follows. When the lid appeared to start moving downward from the highest vertical position, a blink was begun. When the lid returned to that position, the blink was ended. The largest blink position for that subject without any apparent squeezing was labeled as an amplitude of 100%. A blink that did not fully close would have a blink amplitude of less than 100%. This process was repeated for each blink in the 2.5 min interval per task. This process was automated with a custom Matlab program (The MathWorks, Natick, MA, USA). We used this processed blink data in this work.

2.2 Mathematical approach

We first fit a curve to the processed lid position data. Then, the coefficients from the fitting process are combined with measured data as well as error in the fit to form a set of combined data. Then, two types of clustering are performed on the combined data.

2.2.1 Fitting the blink data

When we attempted to use Equation (1), it did not fit a significant fraction of our data well. We modified the function in Equation (1) so that the fit could be improved to better describe a larger number of blinks:

$$f(\mathbf{a}, t) = (a_0 t^2 + a_1 t^3 + a_2 t^4) \exp(-bt^c). \quad (2)$$

The parameters determined from the a non-linear least squares fit are the five quantities a_0, a_1, a_2, b, c . The special case $a_1 = a_2 = 0$ and/or $c = 2$, which includes Equation (1), were also considered. The measurement of the lid position x_i is collected at m times t_i for blink i . The vector of lid positions and times are \mathbf{x} and \mathbf{t} , respectively; $\mathbf{f}(\mathbf{a}, \mathbf{t})$ is the vector of fitting function values at \mathbf{t} . m_i and varies from one blink to another, but we denote the number of time points in a particular blink as m for simplicity. For a representative case below, $m = 58$. Minimization of the sum of the square errors (SSE) over the fit parameters $\mathbf{a} = a_0, a_1, a_2, b, c$ was performed to establish the best fit for the given data via:

$$\min_{\mathbf{a}} \|\mathbf{f}(\mathbf{a}, \mathbf{t}) - \mathbf{x}\|_2^2 = \min_{\mathbf{a}} \sum_{i=1}^m [f(a, t_i) - x_i]^2 = \min_{\mathbf{a}} \text{SSE}. \quad (3)$$

The resulting fit yields: $\hat{a}_i = \{\hat{a}_{0i}, \hat{a}_{1i}, \hat{a}_{2i}, \hat{b}_i, \hat{c}_i\}$, which denotes the coefficients found during the fitting for blink i . MATLAB's `lsqcurvefit` function was used for the

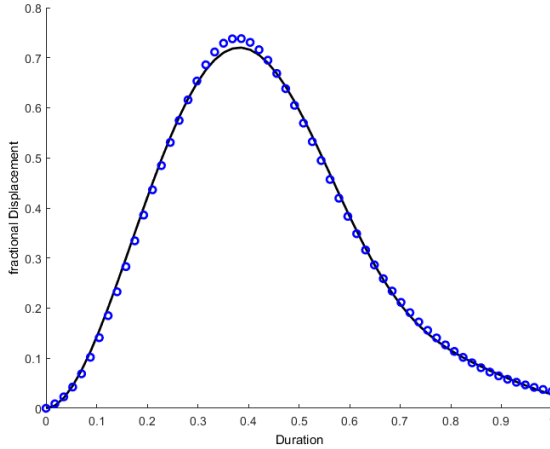


Fig. 1. An example fit of the displacement of the upper eyelid throughout the entire blink using Equation (2). The displacement fraction is relative to a representative full blink; see text for more details. The blink duration is normalized to unity for each blink for fitting.

minimization with all variables unconstrained except for c , which was limited to the interval $1 \leq c \leq 5$. The minimization and subsequent analysis was improved by normalizing the experimental data as follows. The duration of each blink was normalized to $0 \leq t \leq 1$ to allow for a more robust fit and to avoid any problems with small initial gradients in the iteration of the minimization. Furthermore, the lid displacements during the blink were renormalized by dividing by 100%, so that a fractional displacement was used rather than the percentage described in Wu *et al.*²² Thus, a half blink would have a blink amplitude of 0.5 in our renormalized form. Using these normalizations and Equation (2), our approach frequently captured the nature of the blinks very well, with an SSE of 0.0342 and standard deviation of 0.1008 for the example shown in Figure 1 which used $m = 58$ measured displacements. It was found that most blinks had $2 \leq c \leq 3$, and as shown in Figure 2, most of the blinks with a large c value were either full blinks or blinks that Equation (2) was not able to fit well. Numerical exploration did not yield any alternative fits for the data examined, and from this evidence we assume that the fits are unique for this choice of function.

2.2.2 Clustering of the combined data

We then hypothesized that combining parameters from the fit, namely:

$$\hat{\mathbf{a}}_i = \{\hat{a}_{0i}, \hat{a}_{1i}, \hat{a}_{2i}, \hat{b}_i, \hat{c}_i\}$$

together with the log of the residual ($\ln(\text{SSE})$), and directly observed data, such as blink amplitude and duration, would result in a better classification of blinks than

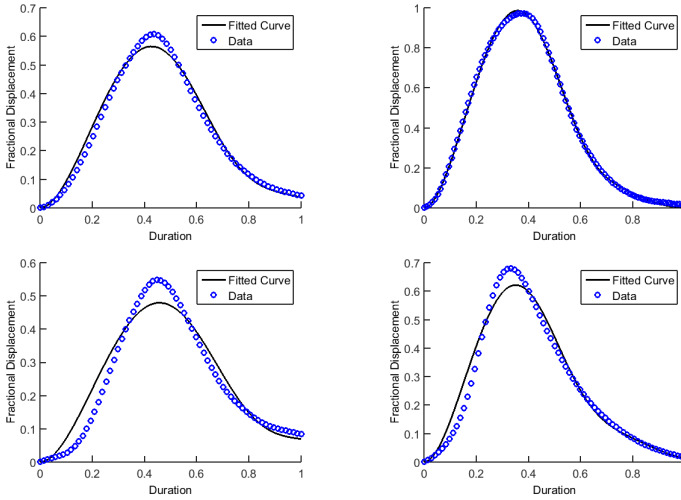


Fig. 2. Representative sample of blinks with $c \geq 3.5$.

could be obtained from using only the directly observed quantities of the blink (such as amplitude and duration). The coefficients of Equation (2) found from the fits contain some additional information about the shape of the lid displacement function compared to the blink amplitude and duration. For example, the larger positive values for c may mean faster decay back to zero displacement, but larger a_0 and a_2 could mean a steeper rise of the curve and slower decay back to zero displacement later in the blink. In what follows, we use the term "measured data" to refer to the blink amplitude (BA), blink duration (BD) and natural logarithm of the IBI (LIBI), which are recorded directly from the blinks. We use the term "fit data" to refer to the resulting coefficients from fitting Equation (2) to the observed blinks. The term "combined data" will refer to using fit data, the residual of the fit and measured data together for blinks, namely:

$$\hat{\mathbf{y}} = \left\{ \hat{a}_{0i}, \hat{a}_{1i}, \hat{a}_{2i}, \hat{b}_i, \hat{c}_i \ln(\text{SSE}), \text{BA}, \text{BD}, \text{LIBI} \right\}. \quad (4)$$

To the fit parameters, we added the logarithm of the minimum SSE, the BA, and BD (which were normalized before fitting), and the logarithm of the IBI. Altogether, we used nine quantities in $\hat{\mathbf{y}}_i$ to characterize each blink: $\{\hat{a}_{0i}, \hat{a}_{1i}, \hat{a}_{2i}, \hat{b}_i, \hat{c}_i\}$ (the fit data), the log of the residual $\ln(\text{SSE}_i)$, and the three physical parameters (the measured data $\text{BA}_i, \text{BD}_i, \text{LIBI}_i$).

We then applied hierarchical clustering methods^{36,37} and spectral clustering methods³⁸ on the combined data. These algorithms seek to combine or cluster like data into more homogeneous groups compared to the original data, as well as to find structure in the data. By structure, we mean the ability to associate like blink displacement functions into a group and to separate unlike blinks into different

groups. After testing a variety of possibilities, we have pinpointed some promising combinations for helping to identify structure in blink data.

All blink data from the five subjects was pooled for the clustering methods; this resulted in a total of $N = 393$ blinks. Two types of clustering methods were applied to the combined data in order to group like kinds of blinks and to identify normal and outlying blinks. We begin with hierarchical clustering, and then proceed to spectral clustering.

3. Results

3.1 Agglomerative hierarchical clustering

In order to better understand the blink parameters and how they may be grouped, agglomerative hierarchical clustering was used.^{37,39} In this method, the number of clusters is set in advance; we varied the number of clusters subjectively to get the best results. More details of this approach are given in Appendix A. The clustering was initially performed on only the three measured parameters that can be observed directly without using any curve fitting ($BA_i, BD_i, \ln(|B|_i)$); the results for the three clusters are shown in Figure 3. For this clustering, we employed a Scaled-Euclidean metric with a weighted average linkage, which normalizes the data and improves the results. Three clusters were readily identified, corresponding to short partial blinks with with approximately less than 40% closure; forced, fuller blinks with long duration and more than 70% closure; and "normal" blinks as shown in Figure 3. It was found that when using agglomerative hierarchical clustering on the combined set of all observed and fit parameters $\hat{\mathbf{y}}$ without prior normalization, no discernible groups emerged for any combination of metric or linkage discussed in the appendix. However, the results were improved when each component of the data was normalized with its z -scores; those results are shown together with the spectral clustering results below.

3.2 Spectral clustering

Some details of spectral clustering³⁸ are given in Appendix B. When we perform spectral clustering, we consider all of the combined data $\hat{\mathbf{y}}$. To facilitate a better clustering, all of the data of each factor x was normalized to its z -score via:

$$\mathbf{z}^{(k)} = \frac{\mathbf{x}^{(k)} - \bar{x}^{(k)}\mathbf{1}}{s^{(k)}\mathbf{1}}, \quad (5)$$

where $\mathbf{x}^{(k)}$ contains the set of the k -th variable of the combined data (e.g., the blink durations), $\mathbf{z}^{(k)}$ contains the corresponding z -scores, $\bar{x}^{(k)}$ is the mean of the k -th variable (a scalar), $\mathbf{1}$ is a vector with unit entries that is the same size as $\mathbf{x}^{(k)}$, and $s^{(k)}$ is the standard deviation of the k -th variable (a scalar).

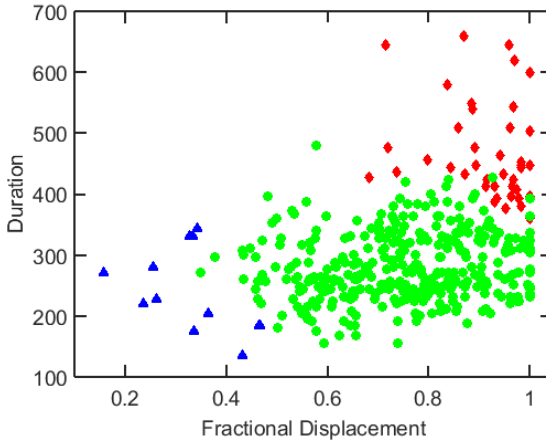


Fig. 3. Clustering performed using only the physical parameters: amplitude, duration, and $\ln(\text{IBI})$, with a Scaled-Euclidean distance and a weighted similarity metric. The clusters are shown using duration and fractional displacement axes only, although the remaining variable $\ln(\text{IBI})$ also affects the clustering.

Plotting a_0 , a_1 and a_2 from the fit data shows that most of the blinks appear to lie on a crescent-like curve after normalization to the z -scores (Fig. 4). We hypothesize from this result that we may call a blink "normal" if it lies close to this curve. We did not determine an analytical approximation to this curve. For smaller values of a_0 and a_2 , and larger values of a_1 , the blink fits are more scattered and lie relatively far from the curve; we hypothesize that these blinks are outliers. Spectral clustering shows that the blinks that are more scattered are clustered in terms of the nine clustering quantities. This is indicated by the lighter-colored circles where the circles are scattered from the curve.

Some of the blinks hypothesized as outliers are shown in Figure 5. Most of these outliers are either short, partial blinks, or blinks that have irregular positions as functions of time, or both. In addition, we also note that blinks from Subject 4, when performed without a fan blowing and while listening to music, had much larger blink amplitude and longer duration than the other subjects. This could be due to an underlying physiological problem, and would require further review; there is too little data to draw a conclusion here.

The values assigned to the nodes by the spectral clustering can be determined by the number of clusters given to the k -means clustering algorithm at the end of the spectral clustering algorithm.³⁸ The results for four different choices of cluster number are shown in Figure 6. From the figure, we see that as the requested number of clusters increases, we are able to capture more subsets of the scattered results that do not appear to lie on the crescent-shaped curve in the coefficient plot.

After normalizing all combined data to their z -scores, we see that similar results

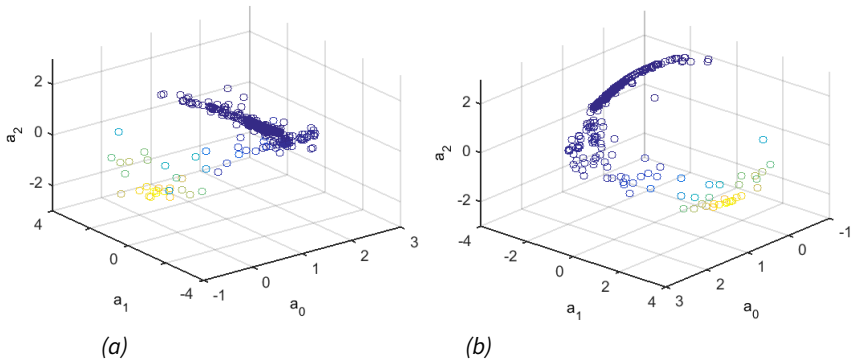


Fig. 4. Spectral clustering performed using all physical and fit parameters displayed using the three polynomial coefficients of the fit normalized to their z -scores. Plot (b) is the same as plot (a), except that the viewpoint has been rotated 180° about the a_2 axis. Note that even though Figure 4 is shown with only three of the blink features (from fit data), all nine of the combined data are used in the spectral clustering. The points are colored using the eigenvector corresponding to the second smallest eigenvalue.

are obtained when comparing the agglomerative clustering (right) to the spectral clustering (left) in Figure 7. This agglomerative clustering was performed using a cosine metric with a weighted average linkage and three clusters. In addition, we see that the spectral clustering is able to identify subgroups (when increasing the number of clusters given to k -means) that the agglomerative clustering cannot. In particular, the clearest results came from seeking three clusters from the agglomerative clustering, while more clusters appeared from spectral clustering (at least six clear ones) and some of the spectral clusters had very few members. In either case, the largest cluster had a_2 very close to zero or larger (roughly $a_2 \geq 0$), with the other clusters appearing largely for $a_2 < 0$. Because different approaches to clustering give a similar result for the biggest cluster, we believe that this supports our hypothesis about detection of normal blinks via our approach.

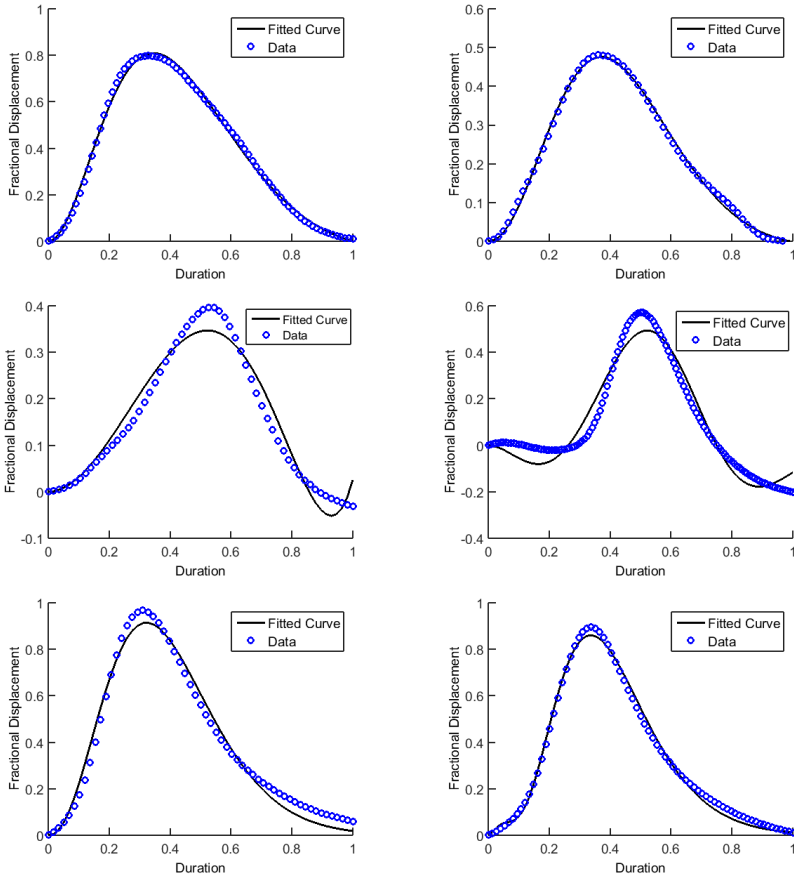


Fig. 5. A representative sample of the plots of the blinks that were outliers found from spectral clustering.

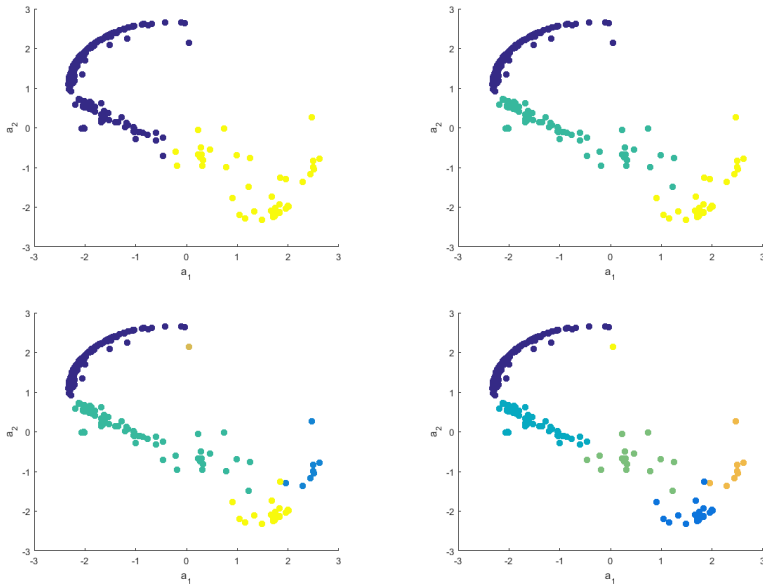


Fig. 6. Plots of the clusters found using spectral clustering with two (top left), three (top right), five (bottom left), and six (bottom right) clusters. The use of five and six clusters was shown instead of four and five because of the identified singleton cluster near the top of the bottom two figures.

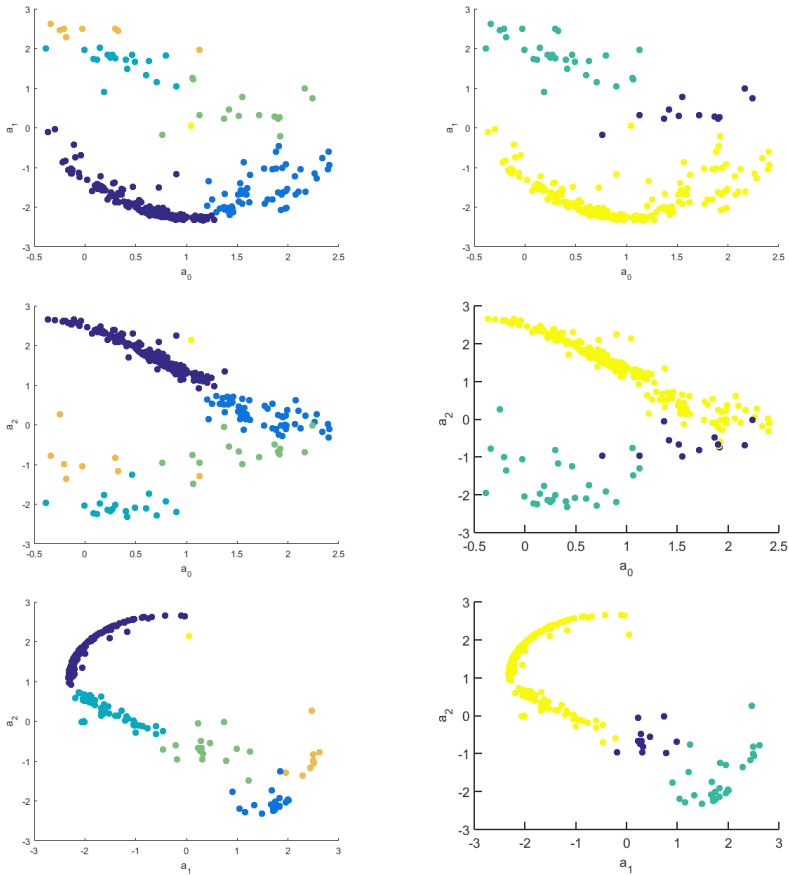


Fig. 7. Plots of the clustering comparing both the results from the spectral and agglomerative methods. The left column corresponds to spectral clustering; the right, to agglomerative clustering. Each row is a different view of the result; note the axis labels. All of the combined parameters were normalized to their z -scores prior to clustering.

Spectral clustering uses more features and produces more differentiation between the points, particularly among the outliers. If we select the blinks corresponding to the yellow cluster in the top right plot in Figure 6, a group starts to form around a blink amplitude of 0.6 and blink duration of 300 ms, one that is not easily distinguished using the clusters based on measured data alone (Fig. 8).

The number of outlying blinks from the pooled blink set are shown by subject and task in tabular form (Table 1). By subject, three of the subjects account for the vast majority of the outlying blinks from the spectral clustering method for either threshold value. The outliers are in the the green, brown, and bright blue clusters in the bottom right plot in Figure 6 and the yellow cluster in the top right plot in Figure 6. By task, outlying blinks appeared to be associated with the fan stimulus for either threshold value. For both cluster selections, it was found that the music tasks accounted for 75% and 76% of the total outliers, respectively. This finding agrees with previous results.^{19,22}

Table 1. (a) Table of the number of outliers according to the specific subject (Sub) and task for the yellow cluster in the top right plot in Figure 6. (b) Table of the number of outliers according to the specific subject and task for the yellow cluster in the top left plot in Figure 6. The total for each task and subject is given in the last column and row of each table, respectively.

	Sub 1	Sub 2	Sub 3	Sub 4	Sub 5	Total
Fan & Game	1	0	2	1	1	5
Fan & Music	1	1	3	2	0	7
No Fan & Game	0	0	2	0	0	2
No Fan & Music	0	4	7	3	0	14
Total	2	5	14	6	1	28

(a)

	Sub 1	Sub 2	Sub 3	Sub 4	Sub 5	Total
Fan & Game	2	2	2	1	1	8
Fan & Music	3	1	6	2	0	12
No Fan & Game	0	0	2	0	0	2
No Fan & Music	0	7	10	3	0	20
Total	5	10	20	6	1	42

(b)

We also see that Subjects 4 and 5 have the least number of outliers (six and one, respectively), and for both subjects, changing the thresholding eigenvalue does not add in any new outliers. We can also identify that the task where subjects do not listen to music and play a video game does not produce any new outliers between the thresholds. Additionally, using Table 1, we can see that Subject 3 has the most outliers for both eigenvalues used.

4. Discussion

After normalizing the blink duration to be $0 \leq t \leq 1$, we found that any blinks with a c value outside of the interval of roughly $1.5 < c < 3$ can be considered outliers in this dataset. From Figure 2, we see that blinks with a $c \gtrsim 3.5$ are normally very full blinks that reach their maximum displacement of the upper lid very quickly, and then take longer than normal to reopen. From Doane's study,¹ the average downstroke time was 82 ms and the average upstroke time was 176 ms, but Evinger *et al.*¹² found a range of blink amplitudes and durations with a non-linear relationship between them. The approach here includes both observed data like BA and BD as well as fit data \hat{a} , and thus, additional information about how the blink trace is shaped. For the same BA and BD, different functions can achieve those same observed quantities, but they may be separated if the fit data \hat{a} are included. Figure 8 shows that many of the outliers appear in what looks like normal blink amplitude and duration ranges. These outliers may have relatively slow and linear downstrokes, or other features that are unusual in the shape of the blink trace. Including this information has resulted in a more automatic identification of blink traces that fell outside the normal range for this dataset.

Spectral clustering may provide the best option for additional classification. It appears that most blinks lie on a crescent-like curve in the polynomial coefficient space (Fig. 4). The outliers in Figure 4 appear to consist mostly of blinks short, partial blinks, as well as a few with irregular shapes. By selecting a particular eigenvalue threshold, we are able to determine a cutoff as to what could be considered outliers in a given dataset.

Using this criteria for the cutoff, when we overlay the outliers from spectral clustering we are able to identify a potential grouping of blinks (Fig. 8) that differs from the majority. Spectral clustering using the parameters from curve fitting together with the measured physical values allowed for an additional classification not possible by the agglomerative clustering using only the physical values.

The number of subjects was small in this study, so general conclusions about blinking and task or disease are not advisable. However, given that the blink rate is known to vary widely with task, mental state, and disease, these methods show great potential for understanding the effects of these different conditions on blinking.

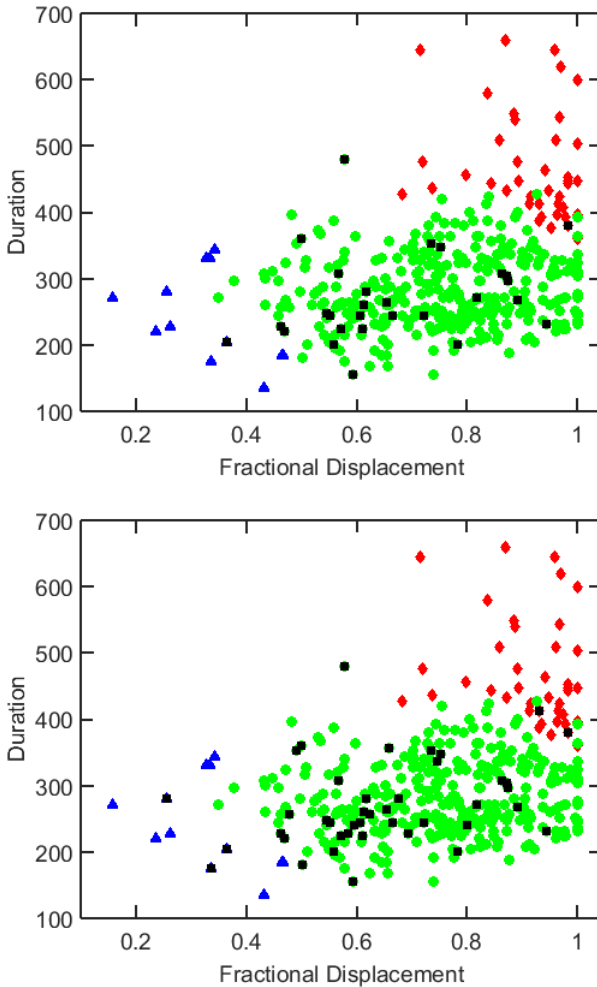


Fig. 8. Plot of the groups found from the agglomerative clustering (red, green, blue) with outliers as determined by spectral clustering (black) superimposed. The top figure corresponds to the yellow cluster in the top right plot in Figure 6, while the bottom one corresponds to the yellow cluster in the top left plot in Figure 6.

5. Conclusion and future directions

A refined classification of blinks was possible through the use of combined data that used both measured data and fit parameters indicates the possibility of identifying abnormal blinks and perhaps other conditions such as DES.²² Further work with a larger set of subjects and more blinks per subject could verify our conjecture about the possible classification of blinks using data from both measured and fit parameters. More data may allow the study of subject-specific classification, which can be desirable in some cases,²² but was not feasible here. More data in condition-specific contexts such as Bell's palsy or blepharospasm may also be aided by a more automated classification of blinks.

We note that clustering results depend on the techniques chosen and the judgment of the user.³⁶ We have been able to obtain similar results from distinct clustering methods provided that each component of the combined data is normalized to its z -scores. Using this normalization may make the results more robust between methods, but work with more data is needed.

Our approach is limited to some extent by our choice of blink displacement function. We showed some of the worst case fits in Figure 2, and thus other functions or approaches to the fits may work for some blinks.⁴⁰ Furthermore, we only used a summary of the curves by using the fit coefficients rather than the functions themselves; using clustering on the functions themselves may yield additional insights.⁴¹ Additionally, other clustering approaches such as those found in the statistical software R maybe be appropriate.

To summarize, blink frequency (or equivalently, IBI) is currently the most common parameter used to categorize blinking in normals and various disease states, but blink frequency does not directly describe the action of the blink itself. There are many blink parameters (blink amplitude, velocity, etc.) that have been studied, but examination of individual parameters are unlikely to adequately describe the blinking process due to the complex interactions among them. Therefore, the analytical method we suggest here has the advantage of taking into account a greater number of the many parameters and quickly identifying groups of similar blinks and outliers. This quantitative method has potential for identifying blinks that may be characteristic of various disease states, and possibly, quantifying the effect of treatments if the treatment is designed to restore normal blinking. In the field of dry eye, there is a current emphasis on neuropathic causes for the condition. Given that the blinking and tear response as well as the symptoms all arise from sensory neurons at the ocular surface, blinking may be a reasonable endpoint for testing the ocular surface neural response.⁴² Additional directions could involve combining blink motion observations with physiological measurements of muscle activity (such as orbicularis oculi or levator palpebrae superioris muscles)² may help clarify at least some causes of variations in blink activity. Similarly, including appropriate neural activity may also shed light on connections between abnormal blinks and neural control of blinking.^{9,12,21,26,43,44}

Acknowledgments

This project was supported by Grants 1412085 (R.J.B., T.A.D., J.K.B.) from the National Science Foundation (NSF) and R01EY021794 (C.G.B., Z.W., R.J.B.) from the National Institutes of Health (NIH). The content is solely the responsibility of the authors and does not necessarily represent the official views of the NSF, National Eye Institute (NEI), or the NIH. J.K.B. was partially supported by the University of Delaware. We thank the anonymous referees for helpful comments that improved the paper.

A. Agglomerative hierarchical clustering

Agglomerative clustering can be thought of as a method for starting with a binary tree of data that is merged into groups of similar points successively. To perform this type of clustering, we require two main inputs besides the data. One is a specified distance metric between any two data points and a measure of similarity between all the groups of data points. For clustering algorithms, some specific distance metrics are often employed, *i.e.*:

$$\text{Euclidean metric} \quad d(x, y) = \sqrt{\sum_{i=1}^n (x_i - y_i)^2}$$

$$\text{Scaled-Euclidean metric} \quad d(x, y) = \frac{1}{\max[d(x, y)]} \sqrt{\sum_{i=1}^n (x_i - y_i)^2}$$

$$\text{Chebyhev metric} \quad d(x, y) = \max_i (|x_i - y_i|)$$

$$\text{Cosine metric} \quad d(x, y) = 1 - \frac{\mathbf{x} \cdot \mathbf{y}}{\|\mathbf{x}\| \|\mathbf{y}\|}.$$

It should be noted that the cosine metric is not strictly a metric in the classical sense (the triangle inequality does not hold). Generally speaking, a Euclidean distance metric is most favorable for low-dimensional datasets where the range of distances only goes over a few orders of magnitude. For higher dimensional datasets, or ones with a wide range of distances, a Scaled-Euclidean metric is normally preferred. The Chebyhev distance is normally appropriate when the difference between any two points is better represented by the differences in individual dimensions rather than all of the dimensions together. The cosine metric works well when trying to capture the similarity between certain feature changes in multiple dimensions.

Once a distance metric is chosen, the next thing to determine is the linkage between each group. Linkage is, in a sense, a measure of how similar two groups are to one another. There are multiple kinds of linkages that are often used in this type of clustering method; let r be a cluster formed by combining two clusters p and q , and let $x_i^{(r)}$ be the i -th element in cluster r , and let $\text{dist}(x, y)$ be a specified distance metric.

Some common linkages are as follows:

$$\text{Single} \quad d(r, s) = \min_{i,j} [\text{dist}(x_i^{(r)}, x_j^{(s)})] \quad (6)$$

$$\text{Complete} \quad d(r, s) = \max_{i,j} [\text{dist}(x_i^{(r)}, x_j^{(s)})] \quad (7)$$

$$\text{Average} \quad d(r, s) = \frac{1}{n_r n_s} \sum_{i=1}^{n_r} \sum_{j=1}^{n_s} \text{dist}(x_i^{(r)}, x_j^{(s)}) \quad (8)$$

$$\text{Weighted Average} \quad d(r, s) = \frac{d(p, s) + d(q, s)}{2} \quad (9)$$

Here, the weighted average linkage is special, in that it is recursively defined by the average of linkages $d(p, s)$ and $d(q, s)$ between previously computed clusters p, q , and s .

It should be noted that agglomerative clustering is not a fully automatic clustering scheme; the distance metric, group linkage, and number of clusters must be specified.

For the agglomerative clustering used in this paper, after selecting a desired metric to use, the distances were computed using MATLAB's `pdist` function, which uses one of the metrics specified from the above list, where each column of the data matrix represents a different dimension. Then MATLAB's `linkage` function was used to determine the similarity between any two groups, using one of the specified methods above. Once the distances and linkage were computed, a predefined number of clusters was computed by MATLAB's `cluster` function. The number of desired clusters was varied until discernable groups emerged, with a recalculation of `cluster` performed at every step.

B. Spectral clustering

Unlike agglomerative clustering, where a distance metric, linkage weighting, and number of clusters must be specified, spectral clustering is, in a sense, completely automated, and one does not specify this parametric information.³⁸ (We include the latter reference as a particularly accessible treatment.) We suppose that there are n blinks. To perform spectral clustering, we first calculate the Euclidean distance matrix:

$$\mathbf{G} = (g_{ij}), \text{ with elements } g_{ij} = \|\mathbf{x}_i - \mathbf{x}_j\|_2^2 \quad (10)$$

where:

$$\|\mathbf{x}_i - \mathbf{x}_j\|_2 = \left[\sum_{m=1}^n (x_i^{(m)} - x_j^{(m)})^2 \right]^{1/2} \quad (11)$$

is the standard 2-norm for vectors \mathbf{x} with n components per blink. Here i and j denote different blinks with $i = 1, 2, \dots, N$ and $j = 1, 2, \dots, N$; the superscript (m) denotes the component of the vector of data for a specific blink with $m = 1, 2, \dots, n$. In our

case, we used a vector of $n = 9$ components corresponding to the measured and fit parameters for each blink.

We then exponentiate the elements of the distance matrix to obtain the similarity matrix \mathbf{W} with elements:

$$w_{ij} = e^{-2g_{ij}}. \quad (12)$$

The similarity matrix W represents a local distance distribution, *i.e.*, the points that are closest together will have a stronger influence on each other than points that are far away. We also define the diagonal degree matrix D whose diagonal elements are:

$$d_{ii} = \sum_{j=1}^N w_{ij}, \quad (13)$$

for N blinks. The degree matrix D represents how strongly connected each data point is to every other data point. We then form the normalized graph Laplacian:

$$L = I - D^{-\frac{1}{2}} W D^{-\frac{1}{2}}, \quad (14)$$

where I is the identity matrix. We now calculate the eigenvalues of L and sort them in increasing order. Zero is always an eigenvalue of L ; the geometric multiplicity of the zero eigenvalue indicates the number of connected components of the theoretical graph of the data (in the sense of graph theory).³⁸ The connected components are then taken to be the clusters. One then uses the associated eigenvectors to assign each point to a cluster. To do this, say that the zero eigenvalue is repeated and has k independent eigenvectors, *i.e.*, its geometric multiplicity is k . The k eigenvectors associated with the zero eigenvalue are assembled into a matrix with each row representing a data point, and each row of the matrix suitably normalized.³⁸ Then, K-means clustering³⁷ is applied to obtain k clusters from this normalized data. The resulting clusters are the output of the spectral clustering algorithm.

There are different interpretations of the spectral clustering approach that may help visualize what is happening. One is that this process can be thought of as an approximation to the certain minimization problems on graphs, which are variations of the mincut problem. The conversion of the clustering problem to the graph cut problem has the advantage of being automatic in the sense that the algorithm determines the number of clusters from the data. Another is to think of the probability of being at various points on a graph due to random hopping by a flea (*i.e.*, a random walk model for diffusion). If a flea jumps around the nodes of a network, with probabilities of jumps scaled to the distance between nodes, then spectral clustering simulates the diffusion of probability of being at every node. The idea is that the flea jumps between clusters rarely, so the clusters get separated in probability depending on where the flea starts. Mathematically, the uniform probability (a steady state in diffusion) is the constant function over the graph, which is always an eigenvector of eigenvalue zero. The initial position of the flea gets projected onto the eigenvectors. If there are k "natural" clusters, then there will be k eigenvectors with eigenvalues much closer to zero than all of the others.

References

1. Doane MG. Interaction of Eyelids and Tears in Corneal Wetting and the Dynamics of the Normal Human Eyeblink. *Am. J. Ophthalmol.* 1980;89, 507–516.
2. Cruz AAV, Garcia DM, Pinto CT, Cechetti SP. Spontaneous Eyeblink Activity. *Ocul. Surf.* 2011;9, 29–30.
3. Wong H, Fatt I, Radke C. Deposition and thinning of the human tear film. *J. Colloid Interface Sci.* 1996;184, 44–51.
4. Jones MB, Please CP, McElwain DLS, Fulford GR, Roberts AP, Collins MJ. Dynamics of tear film deposition and draining. *Math. Med. Biol.* 2005;22, 265–88.
5. Heryudono A, Braun R, Driscoll TA, Cook L, Maki KL, King-Smith PE. Single-Equation Models for the Tear Film in a Blink Cycle: Realistic Lid Motion. *Math. Med. Biol.* 2007;24, 347–77.
6. Deng Q, Braun RJ, Driscoll TA. Heat transfer and tear film dynamics over multiple blink cycles. *Physics of Fluids*, 2014;26(7): 071901.
7. Palakuru J, Wang J, Aquavella J. Effect of Blinking on Tear Dynamics. *Invest. Ophthalmol. Vis. Sci.* 2007;48, 3032–7.
8. Braun RJ, King-Smith PE, Begley CG, Li L, Gewecke NR. Dynamics and function of the tear film in relation to the blink cycle. *Prog. Retin. Eye Res.* 2015;45, 132–164.
9. Manning KA, Evinger C. Different Forms of Blinks and their Two-stage Control. *Exp. Brain Res.* 1986;64, 579–588.
10. Korb DR, Baron DF, Herman JP, Finnemore VM, Exford JM, Hermosa JL, et al. Tear Film Lipid Layer Thickness as a Function of Blinking. *Cornea*, 1994;13, 354–59.
11. Evinger C, Bao J, Powers A. Dry eye, blinking, and blepharospasm. *Mov. Disc.* 2002;17, 75–78.
12. Evinger C, Manning KA, Sibony PA. Eyelid Movements. Mechanisms and Normal Data. *Invest. Ophthalmol. Vis. Sci.* 1991;32, 387–400.
13. Kammer J, Powers A, Horn KG, Hui C, Evinger C. Characterizing the Spontaneous Blink Generator: An Animal Model. *J. Neurosci.* 2011;31, 11256–11267.
14. Korb DR, Blackie CA, McNally EN. Incomplete blinking: Exposure keratopathy, lid wiper epitheliopathy, dry eye, refractive surgery, and dry contact lenses. *Cont. Lens Ant. Eye*, 2007;30, 37–51.
15. Pult H, Korb DR, Murphy PJ, Riede-Pult BH, Blackie CA. A new model of central lid margin apposition and tear film mixing in spontaneous blinking. *Cont. Lens Ant. Eye*, 2015;38, 173–180.
16. Deng Q, Braun RJ, Driscoll TA, King-Smith P. A model for the tear film and ocular surface temperature for partial blinks. *Interfacial Phenom. Heat Transf.* 2013;1(4): 357–381.
17. Acosta MC, Gallar J, Belmonte C. The influence of eye solutions on blinking and ocular comfort at rest and during work at video display terminals. *Exp. Eye Res.* 1999;68, 663–669.
18. Cardona G, Garcia C, Seres C, Vilaseca M, Gispets J. Blink rate, blink amplitude, and tear film integrity during dynamic visual display terminal tasks. *Curr. Eye Res.* 2011;36, 1909–197.
19. Himebaugh N, Begley C, Bradley A, Wilkinson J. Blinking and tear break-up during four visual tasks. *Optom. Vis. Sci.* 2009;86(2): 106–114.
20. Schlote T, Kadner G, Freudenthaler N. Marked reduction and distinct patterns of eye blinking in patients with moderately dry eyes during video display terminal use. *Graefes Arch. Clin. Exp. Ophthalmol.* 2004;42, 306–312.
21. Nakamori K, Odawara M, Nakajima T, Mizutani T, Tsubota K. Blinking is controlled primarily by ocular surface conditions. *Am. J. Ophthalmol.* 1997;124, 24–30.
22. Wu Z, Begley CG, Situ P, Simpson T, Liu H. The Effects of Mild Ocular Surface Stimulation and Concentration on Spontaneous Blink Parameters. *Curr. Eye Res.* 2014;38(1): 9–20.
23. Tsubota K, Hata S, Okusawa Y, Egami F, Ohtsuki T, Nakamori K. Quantitative videographic analysis of blinking in normal subjects and patients with dry eye. *Arch. Ophthalmol.* 1996;114, 715–720.
24. Liu H, Begley C, Chen M, Bradley A, Bonanno J, McNamara NA, et al. A Link between Tear Instability and Hyperosmolarity in Dry Eye. *Invest. Ophthalmol. Vis. Sci.* 2009;50, 3671–79.

25. Begley CG, Simpson T, Liu H, Salvo E, Wu Z, Bradley A, et al. Quantitative analysis of tear film fluorescence and discomfort during tear film instability and thinning. *Invest. Ophthalmol. Vis. Sci.* 2013;54, 2645–2653.
26. Vanderwerf F, Reits D, Smit AE, Metselaar M. Blink Recovery in Patients with Bells Palsy: A Neurophysiological and Behavioral Longitudinal Study. *Invest. Ophthalmol. Vis. Sci.* 2007;48, 203–213.
27. Wu Z, Begley CG, Situ P, Simpson T. The Effects of Increasing Ocular Surface Stimulation on Blinking and Sensation. *Inv. Ophthalm. & Vis. Sci.* 2014;55(3): 1555–1563.
28. Berke A, Mueller S. Einfluss des lidschlages auf die Kontaktlinse und die zugrundeliegenden Kräfte. *die Kontaktlinse*, 1996;1, 17–26.
29. Berke A, Mueller S. The kinetics of lid motion and its effects on the tear film. *Lacrimal Gland, Tear Film, and Dry Eye Syndromes 2*. Ed. by DA Sullivan, DA Dartt, MA Meneray. New York: Plenum, 1998; 417–424.
30. Jossic L, Lefevre P, Loubens C de, Magnin A, Corre C. The Fluid Mechanics of Shear-thinning Tear Substitutes. *J. Non-Newtonian Fluid Mech.* 2009;61, 1–9.
31. Jones MB, McElwain DLS, Fulford GR, Collins MJ, Roberts AP. The effect of the lipid layer on tear film behavior. *Bull. Math. Biol.* 2006;68, 1355–81.
32. Aydemir E, Breward CJW, Witelski TP. The effect of polar lipids on tear film dynamics. *Bull. Math. Biol.* 2010; 1–31.
33. Zubkov V, Breward CJW, Gaffney EA. Coupling Fluid and Solute Dynamics Within the Ocular Surface Tear Film: A Modelling Study of Black Line Osmolarity. *Bull. Math. Biol.* 2012;74, 2062–2093.
34. Ponder E, Kennedy WP. On the Act of Blinking. *Quart. J. Exp. Physiol.* 1928;18, 89–110.
35. Begley CG, Chalmers RL, Abetz L, Venkataraman K, Mertzanis P, et al. The relationship between habitual patient-reported symptoms and clinical signs among patients with dry eye of varying severity. *Invest. Ophthalmol. Vis. Sci.* 2003;44, 4753–4761.
36. Estivill-Castro V. Why So Many Clustering Algorithms? A Position Paper. *ACM SIGKDD Explorations Newsletter*, 2002;4(1): 65–75.
37. Everitt B. *Cluster Analysis*. 5th. Chichester, West Sussex, UK. Wiley, 2011;
38. Luxburg U von. A Tutorial on Spectral Clustering. *Stat. Comput.* 2007;17, 395–416.
39. Johnson SC. Hierarchical Clustering Schemes. *Psychometrika*, 1967;32, 241–254.
40. Ramsay JO, Silverman BW. *Functional Data Analysis*. 2nd. Berlin. Springer, 2005;
41. Jacques J, Preda C. Functional Data Clustering: A Survey. *Adv. Data Anal. Class.* 2014;8, 231–255.
42. Rosenthal P, Borsook D. Ocular Neuropathic Pain. *Br. J. Ophthalmol.* 2016;100, 128–134.
43. Belmonte C, Gallar J. Cold Thermoreceptors, Unexpected Players in Tear Production and Ocular Dryness Sensations. *Invest. Ophthalmol. Vis. Sci.* 2011;52, 3888–3892.
44. Parra A, Gonzalez-Gonzalez O, Gallar J, Belmonte C. Tear fluid hyperosmolality increases nerve impulse activity of cold thermoreceptor endings of the cornea. *Pain*, 2014;155, 1481–1491.



Selective fusion of structural and functional data for improved glaucoma detection

Paul Y. Kim¹, Khan M. Iftexharuddin², Pinakin G. Davey³, Martha Tóth⁴, Anita Garas⁴, Gabor Holló⁴, Edward A. Essock⁵

¹Department of Computer and Mathematical Sciences, Lewis University, Romeoville, IL, USA; ²Department of Electrical and Computer Engineering, Old Dominion University, Norfolk, VA, USA; ³College of Optometry, Western University of Health Sciences, Pomona, CA, USA; ⁴Glaucoma Service, Department of Ophthalmology, Semmelweis University, Budapest, Hungary; ⁵Department of Psychology and Brain Sciences, University of Louisville, KY, USA

Abstract

This work proposes a novel selective feature fusion of structural and functional data for improved glaucoma detection. The structural data, such as retinal nerve fiber layer (RNFL) thickness measurement acquired by scanning laser polarimetry (SLP), is fused with the functional visual field (VF) measurement recorded from the standard automated perimetry (SAP) test. The proposed selective feature fusion exploits the correspondence between structural and functional data obtained over multiple sectors. The correlation coefficients for corresponding structural-function sector pairs are used as weights in subsequent feature selection. The sectors are ranked according to the correlation coefficients and the first four highly-ranked sectors are retained. Following our prior work, fractal analysis (FA) features for both structural and functional data are obtained and fused for each of the selected sectors, respectively. These fused FA features are then used for glaucoma detection. The novelty of this work stems from (1) locating structure-functional sectoral correspondence; (2) selecting only a few interesting sector pairs using correlation coefficient between structure-function data; (3) obtaining novel FA features from these pairs; and (4) fusing these features for glaucoma detection. Such a method is distinctively different from other existing methods that exploit structure-function models in

Correspondence: Pinakin Davey OD PhD, College of Optometry, Western University of Health Sciences, Pomona, CA 91766, USA
E-mail: contact@pinakin-gunvant.com

that structure-function sectoral correspondences have been weighted and, based on such weights, only portions of the sectors are retained for subsequent fusion and classification of structural and functional features. For statistical analysis of the glaucoma detection results, sensitivity, specificity, and area under receiver operating characteristic curve (AUROC) are calculated. Performance comparison is obtained with those of existing feature-based techniques such as wavelet-Fourier analysis (WFA) and fast-Fourier analysis (FFA). Comparisons of AUROC values show that our novel selective feature fusion method for discrimination of glaucomatous and ocular normal patients slightly outperforms other existing techniques with AUROCs of 0.98, 0.98, and 0.99 for WFA, FFA, and FA, respectively.

Keywords: scanning laser polarimetry (SLP), standard automated perimetry, fusion, glaucoma detection, selective fusion, sectoral topographic correspondence, retinal nerve fiber layer (RNFL), fractal analysis (FA)

1. Introduction

Glaucoma is a progressive optic neuropathy which causes both structural and functional damages on eyes and ultimately leads to blindness.¹ Structural damages are due to rapid retinal ganglion cell death in the retinal nerve fiber layer (RNFL).²⁻⁴ Functional damage is represented by visual field (VF) loss.^{5,6} For a complete and reliable assessment of glaucomatous damages, it may be useful to consider both structural and functional visual impairment. Such a complete assessment may be more effective when the relationship between structure and function is known. It has been reported that local damage in the optic nerve corresponds to the regions of visual loss.⁷ Such correspondences have been investigated, and models such as Hood-Kardon,⁸ Harwerth,⁹ Drasdo,¹⁰ and Hockey-Stick¹¹ have been proposed. The Hood-Kardon model assumes that structural and functional data are linearly related. However, this assumption is only true for the peripheral rather than central visual field regions. Likewise, different regions may require different slopes or strengths. The Harwerth model is based on comparisons of perimetric data with histological data in monkey eyes, and has been validated with human histological data. However, the structure-function correspondence in the Harwerth model shows an increasing linearity with eccentricities, and yet does not accurately predict unique sectoral correspondences. The Drasdo model is a combination of both a linear and a non-linear relationship. Visual field sensitivities follow a linear relationship, whereas higher sensitivities follow a non-linear relationship. However, the non-linear part of the model may not have been well defined for accurate prediction. The Hockey-Stick model is a linear model with two different slopes, such as a shallower slope for the locations closer to fixation and a steeper slope for all other areas. However, only two slopes may not adequately represent the different structure-function relationship

of the regions. Overall, improved glaucoma detection based on structure-function correspondence has yet to be proven and verified.¹²⁻¹⁴

Research combining structural and functional data has reported better diagnostic power for glaucoma detection compared to using structural or functional data alone.¹⁵⁻¹⁸ Horn *et al.* reported better glaucoma classification rates by simple addition of the scores from both structural and functional data.¹⁹ However, a simple summation of structural and functional data in terms of scores cannot be an optimal method due to the lack of consideration of the unique structural-function relationship. Bizios *et al.* claimed 95% accuracy in glaucoma diagnosis by multiplying the different sectors for both structural and functional data with specific factors.²⁰ The factors were acquired by averaging pattern deviation probability scores based on six sectors. However, the authors did not report the AUROC performance metric for discriminating glaucoma.

Recently, Yousefi *et al.* reported a correlation-based feature subset selection where an optimal subset of the features was obtained by ranking all the features after concatenating 7 RNFL data points and 54 VF data points.²¹ The correlation coefficients were measured between 61 individual points and the AUROC performance metric was obtained. However, the authors did not consider the unique correspondence between structural and functional data, which may provide an additional benefit for improved glaucoma detection.

In comparison, we propose a novel feature fusion method that exploits unique sectoral correspondence between structural and functional data in order to acquire better features. The proposed model selects multiple pair-wise sectors based on sectoral correspondences between structural and functional data, obtains correlation coefficients from pair-wise sectors, and selects the corresponding sector-pairs based on correlation coefficients, respectively. Finally, fractal analysis (FA) features are obtained from structural and functional data for selected sector-pairs and used in the subsequent feature fusion step. Our prior study shows the effectiveness of FA features in glaucoma detection.²²

For functional data assessment, the original VF data, which are recorded in a circular 2D space with 59 data points, are converted into a 1D vector. For this step, the 59 data points are re-arranged with a novel labeling methodology, as discussed in a subsequent section. FA features are then extracted from the acquired functional data. For structural data assessment, both 1D and 2D RNFL eye-scan data are analyzed. For 1D RNFL assessment, a 1D temporal, superior, nasal, inferior, and temporal (TSNIT) graph consisting of RNFL thickness measurement data acquired by scanning laser polarimetry (SLP) around the parapapillary retina area is used. The FA features are extracted from the 1D TSNIT RNFL data. For 2D RNFL assessment, we investigate 2D feature-based techniques on specific regions of interest (ROIs) to represent glaucomatous damage. These ROIs are obtained around the parapapillary retina area excluding the optic disc. The maximum optic disc size is selected to ensure elimination of the optic disc.

Finally, selective feature fusion of the results is obtained from joint structural and functional analyses. For this task, a novel mapping table is obtained which divides the corresponding structural and functional data into ten sectors. Utilizing this mapping table, as shall be discussed in a subsequent section, the sector-wise correlation coefficients between structural and functional data are obtained. Such coefficients indicate the relative strength of correspondence between structural and functional data for each sector-pair, and are subsequently used as the global coefficients to weigh corresponding structural and functional data to emphasize the areas of significance in the sector-pairs. Following this step, only the sector-pairs with greater emphasis are retained. Fractal analysis (FA) features are then extracted from the selected sector-pairs of both structural and functional data. The FA features from structural and functional data are fused and classification performance metrics are obtained using the fused FA features for improved glaucoma detection.

Section 2 discusses a brief background review for functional, structural, and fractal analyses, as well as structure-function relationship. The detailed methodologies for the proposed techniques are discussed in Section 3. Results and corresponding discussion are presented in Section 4, followed by the conclusions in Section 5.

2. Background review

2.1. Functional analysis: visual field (VF) test

The VF is the area of space visible to central and peripheral vision in immobile eyes.⁶ The VF test measures visual sensitivity in patients by evaluating their ability to detect points of light. Since patients may not recognize VF defects until the symptoms or signs of peripheral vision loss are obvious, the VF test can aid early detection of such defects. Standard automated perimetry has been widely used for testing VF. The VF test uses stationary white light stimuli at fixed locations on a white background, gradually increasing their intensity or size until the stimuli are perceived. The visibility at the fixed locations is measured using the threshold values of various intensities. The test is done one eye at a time and the patient is prompted to respond to light sensation. The threshold values are then recorded in the decibel (dB) scale, where zero dB denotes the brightest stimulus while the greatest dB is the dimmest stimulus.

2.1. Structural analysis: retinal nerve fiber layer (RNFL) assessment

Scanning laser polarimetry (SLP) is used for assessing RNFL data. SLP assesses ocular structure by estimating the thickness of the peripapillary RNFL based on its birefringent property.⁴ When a polarized light reaches the birefringent structure of the RNFL, a phase-shift, *i.e.*, light retardation, occurs. The amount of retardation is directly proportional to RNFL thickness. Since the retardation can occur at the

cornea and lens, not just at the RNFL, proper compensation is necessary. After patient-specific compensation is performed, the amount of retardation is calculated pixel-wise and displayed in a map of the scanned area.

2.2 Wavelet-Fourier analysis (WFA)

Complete details of the WFA analysis are available elsewhere.²³ Briefly, while fast-Fourier analysis (FFA) is a good candidate for analyzing non-stationary signals such as 1D TSNIT RNFL data, it has one drawback. In transforming to the frequency domain, the non-periodic local information is lost. Wavelet analysis (WFA) can overcome such a drawback by revealing the hidden aspects, such as breakdown points, discontinuities in higher derivatives, and self-similarity.²³ One major advantage of the WA is that it can perform local analysis, which analyzes a localized area of a larger signal using flexible wavelets. A wavelet is a waveform of effectively limited duration that has an average value of zero. Comparing wavelets in the WFA with the sinusoidal waves of the FFA, wavelets are more irregular and asymmetric with limited duration. For many signals, the low-frequency content is the most important part, providing the signal its identity. The high-frequency content, on the other hand, imparts unique characteristics. Hence, WFA has two filtering processes that obtain two different types of coefficients: approximation coefficients and detail coefficients. The approximation coefficients are the high-scale, low-frequency components of the signal. The detail coefficients are the low-scale, high-frequency components. These two processes constitute so-called wavelet decomposition. WFA is performed by applying a discrete-wavelet transform (DWT), resulting in the approximation and the detail coefficients.²³ A DWT is applied to the approximation coefficients to produce second-level results that are used in the subsequent analysis. The detail coefficients are processed using fast-Fourier transform (FFT) to obtain high-frequency information. The DWT and FFT are repeated on pre-determined scales using the amplitude to maximize performance.

2.3. Fast-Fourier analysis

The discrete Fourier transformation breaks down a statistically varying signal into the elements of sinusoids of different frequencies so that it may transform the input signal from time-domain to frequency-domain. FFA is useful when the valuable information of the signal frequency is intended to be obtained and utilized. Mathematically, the process of FFA is represented by the Fourier transform, which is the sum over all time of the input signal, multiplied by a complex exponential.²⁴ In actual computer simulation, the Fourier transform is done in a discrete manner, yielding discrete Fourier coefficients. The fast-Fourier transform (FFT) is a computationally efficient implementation of the DFT that achieves the same results more quickly. Using these fast-Fourier coefficients, the composite function is obtained, allowing the constituent sinusoidal components of the original signal to be traced. In this study, the FFA is applied to the RNFL thickness data obtained from SLP.

2.4. Fractal analysis (FA)

A fractal is a rough or fragmented geometric object with an infinite nesting of structure at all scales. Each fractal is a reduced-size copy of the whole, which accounts for localized variation. In fractal analysis, the non-integer fractal dimension (FD) represents the quantitative measurement of the fractal object. For estimating FD, we use a box-counting (BC) and a multi-fractional Brownian motion (mBm) method. The BC method calculates the FD features for each size of the boxes by dividing a 2D image into boxes of predetermined size, r , and counting the number of the occupied boxes, N , needed to capture the signal values. The resulting FD features are the ratios between the logarithmic values of N and $1/r$. The mBm method calculates the FD features by adopting a continuous Gaussian process that measures a Holder exponent.

2.5. Structure-function relationships

A quantitative model relating structure (RNFL thickness or retinal ganglion cell (RGC) counts) and function (visual field sensitivity) is helpful in utilizing both structural and functional data for the diagnosis of glaucoma. The Hood-Kardon model is based on the linear structure-function relationship and predicts structural data (*i.e.*, RNFL thickness) from functional data (*i.e.*, visual field sensitivity). This model has shown limited accuracy due to the fact that the linear relationship holds for the peripheral visual field, whereas the relationship for the central visual field is non-linear. In addition, it has been shown that this model does not perform well in subjects with normal eyes. The Hockey-Stick model adopts two different relationships in two different regions that best describes the structure-function relationship. The first region involves the area surrounding the macula with a slope of 0.16, while elsewhere with a slope of 1. This two-line or Hockey-Stick model has provided a reasonable fit for all regions with the sharp breakpoint being smoothed or avoided. Recently, Yousefi *et al.* employed the concatenation of structural and functional features without consideration of any inherent structure-function relationship for feature fusion.²¹ The structural features were obtained from ocular coherence tomography (OCT) RNFL thickness measurements, while functional features were the threshold values of the VF tests. Next, correlation-based feature subset selection (CFS) was used to select a subset of the best performing features out of a pool of features. The selected correlation coefficients were used to enhance the AUROC performance metric.

Unlike the models mentioned above, our proposed method considers the inherent structure-function relationship in multiple structural and functional regions. We obtain the relative importance of these structural-functional region pairs using correlation and retain only four pairs of regions for subsequent processing for glaucoma diagnosis.

3. Materials and methods

Figure 1 shows the overall flowchart of the proposed selective feature fusion method using fractal features from structural and functional test measurement data for improved glaucoma detection. In this study, we used 154 eyes (77 glaucomatous, 34 left-eyes, and 44 females; and 77 normal, 35 left eyes, and 51 females). Average age for these 154 patients was 57.06 with a standard deviation of 11.82. While approximately matched for age, the glaucomatous (mean age of 59.0) and normal (mean age of 55.1) patient groups showed a significant age difference (independent samples t-test $t = -2.13$, $P = 0.036$). We performed a statistical analysis by calculating sensitivity, specificity, and AUROC, and then compared the performance of the new method against that of existing feature-based techniques such as WFA and FFA. We briefly discuss each step in Figure 1.

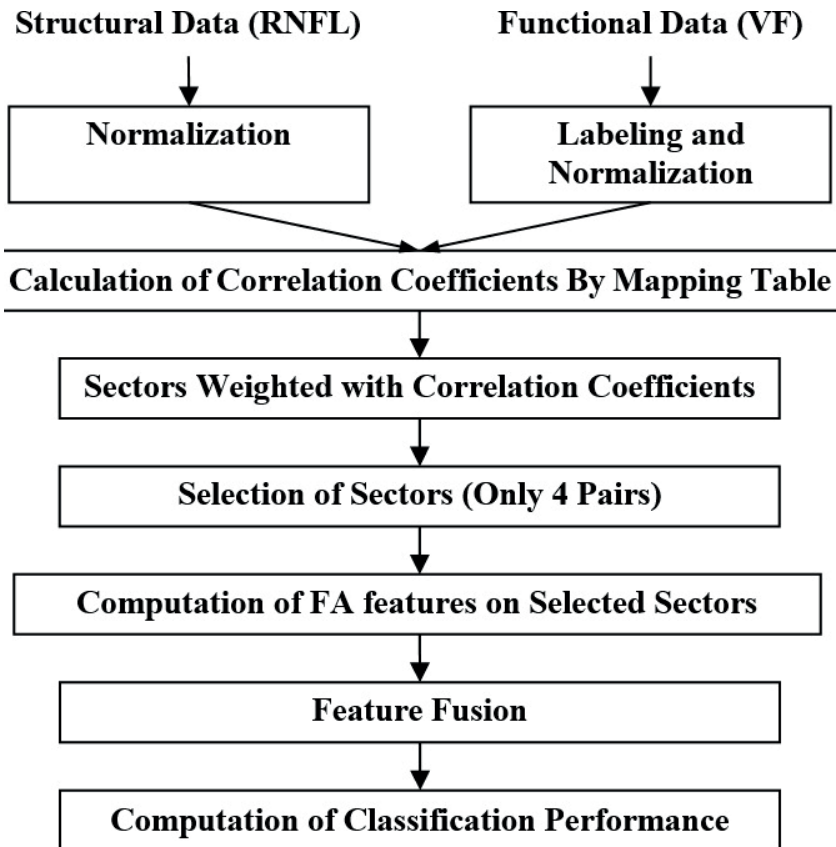


Fig. 1. Flowchart of a selective feature-based fusion method using fractal features from structural and functional test measurement data for glaucoma detection.

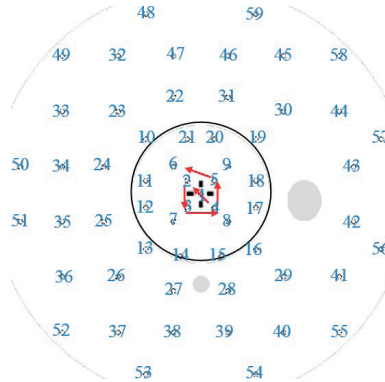


Fig. 2. The proposed labeling of visual field (VF) points in our work.

3.1. Functional analysis

The functional analysis begins by labeling the VF sensitivities at each of the 59 locations (Octopus Perimeter, Normal G2 program, Haag-Streit AG, Koeniz-Berne, Switzerland) using a novel labeling methodology. For the labeling methodology, all 59 VF points are arranged corresponding to the visual sensitivities into 1D data vectors by labeling and regrouping them using the following pre-determined labeling indices. Unlike other types of labeling, such as the raster scan method,²⁵ VF points are labeled clockwise for left eyes and counterclockwise for right eyes. This labeling is consistent with the one proposed by Holló *et al.*²⁶ Figure 2 shows the proposed labeling methodology of the 59 VF test points.

In Figure 2, the labeling starts from the center point and moves to the point that is located either at 45° for the left eye or 135° for the right eye. Subsequent points are followed clockwise for the left eye and counterclockwise for the right eye. Once the labeling is done, all the VF points of a specific patient are obtained in vector form. These VF data vectors are stacked together for all the patients.

3.2. Structural analysis

For 2D structural analysis, we obtain a region of interest (ROI) in a real 2D 256×128 RNFL image data as follows. To obtain the best ROIs, we first obtain the square-shaped boxes that include the areas surrounding the optic disc. The squares that include the optic disc are excluded since the features from the optic disc do not contain useful information. The resulting outer box size is 95×95 , while that for the inner box is 47×47 . An example ROIs for a patient is shown in Figure 3. We then use the piecewise triangular prism surface area (PTPSA) method for FD feature extraction.^{27,28}

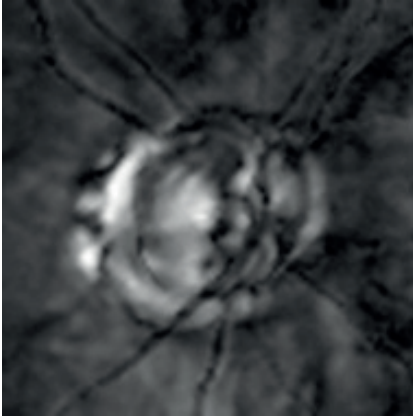


Fig. 3. An example of a patient (A) outer box (95×95) (B) inner box (47×47).

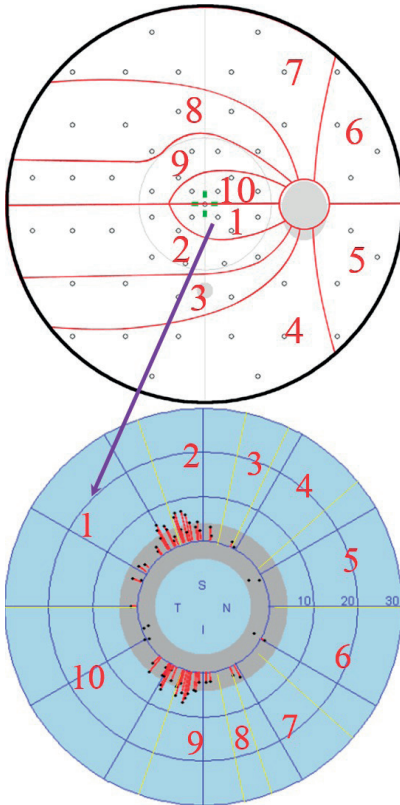


Fig. 4. VF sectors and their corresponding optic disc polar angle sectors.¹⁸

3.3. Selective feature-based fusion of structural and functional data

In this section, the sector-wise structural and functional relationship for selective feature fusion for improved glaucoma detection is discussed. Figure 4 shows a mapping between the 1D 64-point TSNIT RNFL data and 59 VF test points in ten sectors according to polar angle segmentation.²⁹ In order to show an example mapping, the 1st RNFL zone ($0-70^\circ$) is associated with the four VF points in the 1st VF sector, as shown in Figure 4. Note that while polar angle analysis is done in a clock-wise way, the sectors are labeled in a counter-clock-wise way due to the fact that RNFL defects and VF defects are vertically mirrored. To ascertain the degree of association between the sectors of the 1D TSNIT RNFL and VF data, we obtain the scatter plots between the 1D TSNIT RNFL vs VF data for all 154 patients. We show a few out of the ten corresponding sectors in Figure 5. On each sector scatter plot, linear regression analysis has been performed to analyze the association between the 1D TSNIT RNFL and VF data.

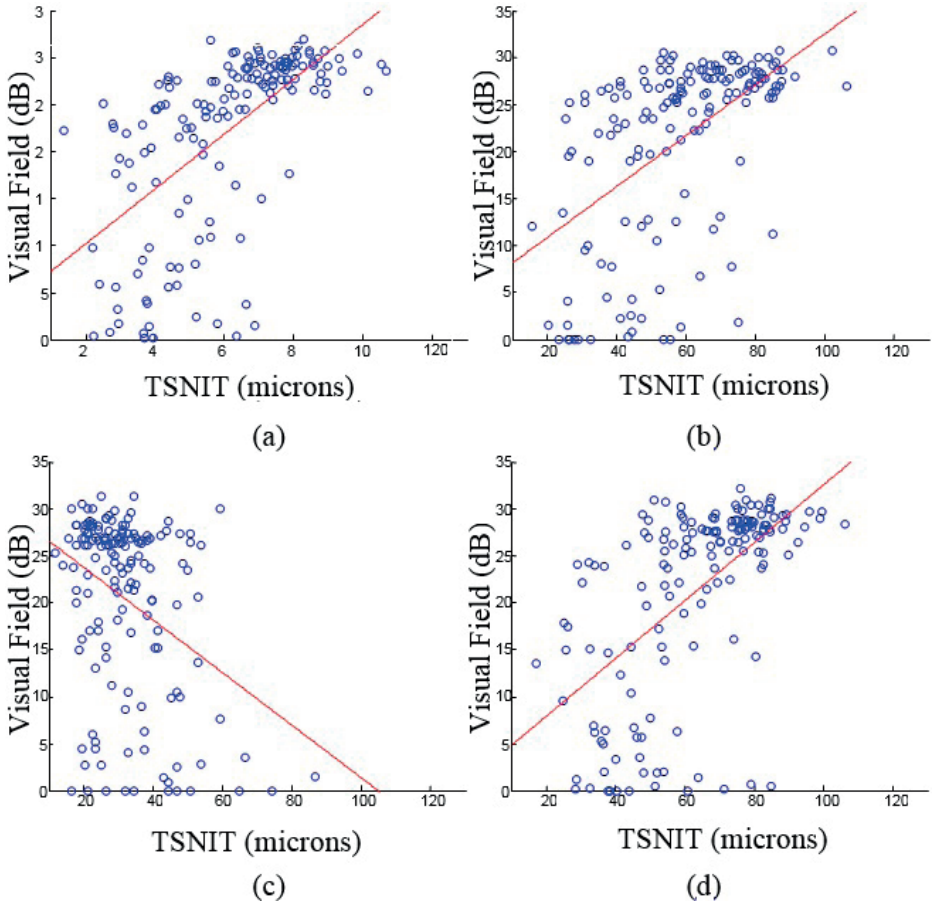


Fig. 5. Examples of scatter plots showing the association between the TSNIT measured by SLP and VF measured by SAP in each sector (2nd, 3rd, 8th, and 9th).

We then compute the degree of association for each sector using Pearson's correlation coefficients. Figure 6 shows the different degrees of association for the different sectors. The four sectors with the strongest associations based on Pearson's coefficients are selected. We then discard the information in the other sectors and utilize only the 2nd, 3rd, 8th, and 9th sectors that are weighted with the global coefficients, as shown in Figure 6. Therefore, we use 40% of the RNFL TSNIT and VF data for the rest of this study.

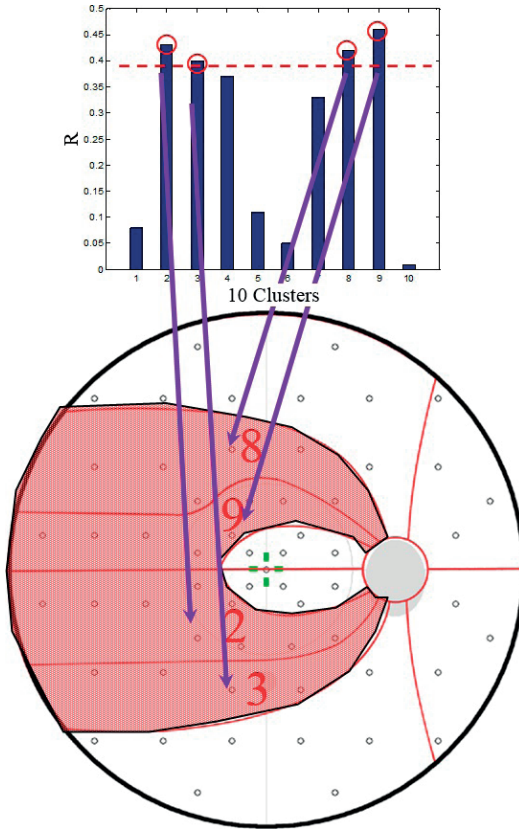


Fig. 6. Selected global coefficients for sectors and their corresponding VF sectors.

4. Results

4.1. Functional analysis

Figure 7 shows the VF data points from normal and glaucomatous eyes (right and left) for all 154 eyes. As discussed earlier, these VF data points have been labeled and plotted separately for comparison purposes.

Note in Figures 7b, 7d, 7f, and 7h that the right and left eyes in each group (*i.e.*, normal and glaucomatous eyes) have similar shapes, respectively. For normal eyes, as shown in Figures 7a and 7c, the plots show monotonically decreasing values without much variation. However, the shape of glaucomatous eyes has very different values than that of normal eyes, as shown in Figures 7(e) and (g), wherein there are considerable irregularities and abrupt changes. Such differences and changes in the shape of the VF data points between normal and glaucomatous eyes justify the use of feature-based techniques such as FFA, WFA, and FA.

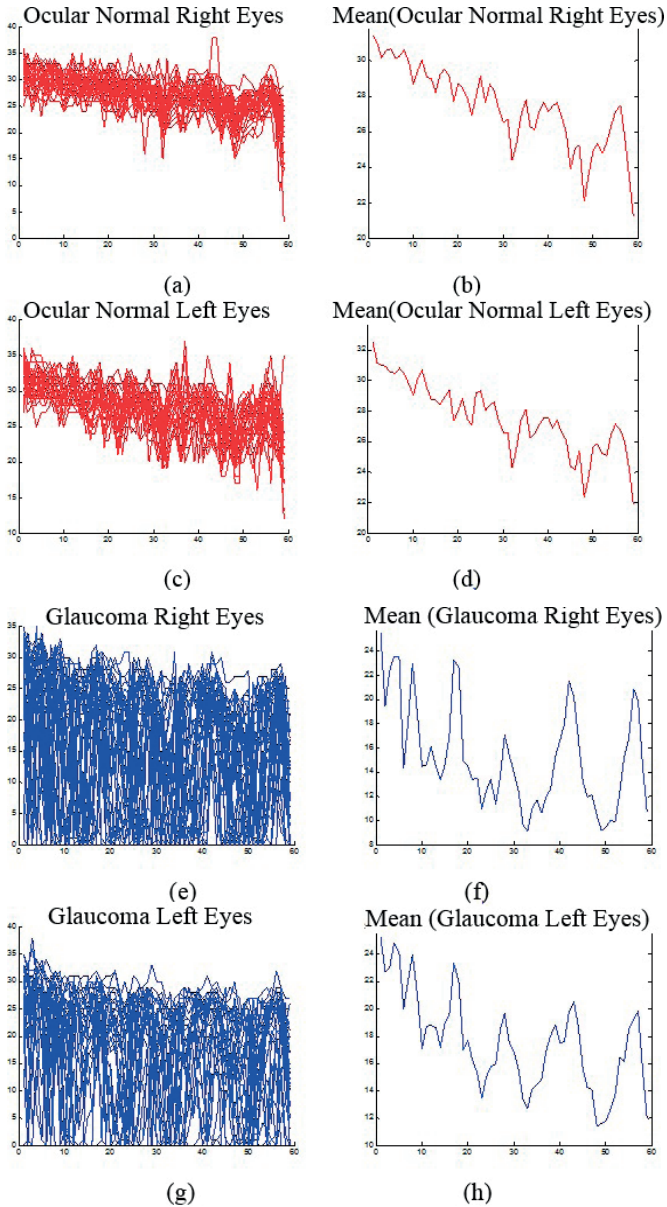


Fig. 7. 1D visual field (VF) raw threshold data in dB for normal and glaucoma eyes is plotted for the right and left eye separately: (a) normal right eyes; (b) mean value of normal right eyes; (c) normal left eyes; (d) mean value of normal left eyes; (e) glaucomatous right eyes; (f) mean value of glaucomatous right eyes; (g) glaucomatous left eyes; (h) mean value of glaucomatous left eyes.

Table 1. The comparison of sensitivity, specificity, and AUROC for functional analysis

Methods	(Sensitivity/Specificity/ AUROC) (Sensitivity at 80; Sensitivity at 90)
FFA	0.84/0.99/ 0.87 (0.84; 0.84)
WFA	0.84/0.99/ 0.87 (0.84; 0.84)
FA (BC + mBm)	0.92/0.99/ 0.95 (0.92; 0.92)

Table 2. Comparison of AUROC for 1D TSNIT RNFL analysis

Methods	(Sensitivity/Specificity/ AUROC) (Sensitivity at 80; Sensitivity at 90)
FFA	0.87/0.93/ 0.89 (0.87; 0.87)
WFA	0.87/0.93/ 0.91 (0.87; 0.87)
FA	0.90/0.92/ 0.91 (0.94; 0.73)

Table 3. AUROC comparison for real 2D RNFL analysis without optic disc

Methods	(Sensitivity/Specificity/ AUROC) (Sensitivity at 80; Sensitivity at 90)
FFA	0.92/0.92/ 0.91 (0.95; 0.92)
WFA	0.88/0.87/ 0.91 (0.90; 0.81)
FA	0.92/0.90/ 0.92 (0.95; 0.90)

Table 1 shows the comparison of sensitivity, specificity, and AUROC for FFA, WFA, and FA for VF data analysis for all 154 patients. In Table 1, our fractal analysis (FA) feature-based technique performs the best among all feature-based techniques with corresponding AUROCs for FFA, WFA, and FA being 0.87, 0.87, and 0.95, respectively (FFA vs FA, $P < 0.05$; WFA vs FA, $P < 0.05$; FFA vs WFA, $P < 0.05$). The best performance of fractal analysis features demonstrates that embedded irregularity in VF data has been well characterized.

Table 4. AUROC comparison of structural, functional data and their selective fusion for raw, FFA, WFA, and FA after the cluster-wise multiplication of Pearson's correlation coefficients

Methods	(Sensitivity/Specificity/AUROC) (Sensitivity at 80; Sensitivity at 90)			
	Structural (RNFL)	Functional (VF)	Fusion of all VF and RNFL data	Selective fusion of 40% VF and RNFL data
Raw	0.84/0.91/ 0.94 (0.92; 0.84)	0.78/0.99/ 0.92 (0.88; 0.79)	0.87/0.97/ 0.96 (0.92; 0.90)	0.96/0.90/ 0.98 (0.96; 0.95)
FFA	0.87/0.90/ 0.94 (0.90; 0.84)	0.78/0.96/ 0.92 (0.88; 0.79)	0.86/0.99/ 0.96 (0.96; 0.87)	0.96/0.94/ 0.98 (0.97; 0.96)
WFA	0.84/0.95/ 0.94 (0.88; 0.84)	0.84/0.99/ 0.94 (0.91; 0.86)	0.87/0.94/ 0.96 (0.94; 0.87)	0.94/0.94/ 0.98 (0.95; 0.94)
FA	0.81/0.91/ 0.90 (0.84; 0.81)	0.88/0.95/ 0.93 (0.88; 0.88)	0.92/0.94/ 0.98 (0.97; 0.92)	0.91/0.99/ 0.99 (1.00; 0.95)

The novel FA technique outperforms other feature-based techniques such as FFA and WFA by a margin of 8% in the functional analysis. However, comparison of our feature-based results with that of the mean deviation (MD) method suggests that the MD method shows an AUROC of 0.98 (does not differ significantly, $P > 0.5$).

4.2. Structural analysis

Using FA along with FFA and WFA features for 1D and 2D RNFL structural analyses yields the following results. Table 2 compares AUROC for 1D RNFL structural analysis, while Table 3 does the same for 2D RNFL structural analysis. We use the same PTPSA method for computing FD in this analysis. We then compute the AUROC that discriminates between glaucoma and normal patients with selected classifiers based on FFA, WFA, and FA features extracted from the ROIs of real 2D RNFL image data. Note that both 1D and 2D RNFL data analyses, even with our novel fractal features from real 2D RNFL image data, are not comparable to the 0.94 AUROC of the standard machine method known as the Nerve Fiber Index (NFI). There may be several reasons for this. First, literature review shows that real 2D RNFL images may not provide a better representation of glaucoma characteristics than 1D TSNIT RNFL. Second, we choose specific ROIs for real 2D analysis as square-shaped when the better representation may be circular-shaped. Since separate feature-based analyses of VF and RNFL data do not offer better glaucoma detection performance, we investigate fusion analysis for these data next.

4.3. Selective features-based fusion

For comparison, the AUROCs results for structural, functional, and selective feature fusion using raw data, FFA, WFA, and FA features are shown in Table 4, respectively. Table 4 shows that all simple fusion methods on raw data, FFA, WFA, and FA features enhance classification performance. The last column in Table 4 shows that the proposed selective fusion method using FA features slightly outperforms all feature-based and MD methods with an AUROC of 0.99. It should be noted that this improvement is obtained with only 40% of VF and RNFL data. It also outperforms the simple feature concatenation method (FA (BC + mBm)), whose accuracy is 95% ($P < 0.05$).

5. Discussion

This study indicates the potential efficacy of selective feature fusion of structural and functional data for improved glaucoma detection. A novel labeling methodology is applied to VF data to obtain the 1D VF data vectors. Sophisticated FA features are extracted from both SF and structural RNFL data for selective feature fusion. The results in this paper show that the FA feature-based technique effectively exploits the shape features from VF data to perform as well or better than other feature-based techniques with corresponding AUROCs.

The efficacy of selective feature fusion of structural and functional data for improved glaucoma detection is demonstrated next. The proposed novel selective feature fusion exploits the inherent correspondence between RNFL and VF data using a lookup-type method. It is shown that selectively choosing 40% of the combined RNFL and VF data can effectively capture the inherent correspondence for improved glaucoma detection. Statistical analyses show that the proposed selective feature fusion method of structural and functional data does as well or better than existing WFA and FFA, with AUROCs of 0.98, 0.98, and 0.99, respectively.

Examining the application of shape-based analysis on the visual field data we find that the FA analysis outperforms the WFA and FFA by 8%; however, it is not superior at discrimination when compared to the MD as measured by visual fields. There are several possible reasons as to why our proposed feature-based results may not be as good as using the MD method. First, the patient group we studied may not reflect enough local variation or randomness in their original VF data (this will be considered in a future report). Hence, a global index such as MD performs well, whereas local feature-based techniques such as FFA, WFA, or FA may not perform as well. Second, even with the novel labeling methodology, the VF data vectors may not reflect structural information in the case of the RNFL. Consequently, performance may not be comparable. To address this issue, we utilize the topographic correspondence between structural and functional test measurement data to fuse useful information from both domains for improved glaucoma detection.

Yousefi *et al.*²¹ has recently published a study combining structure and function results. They acquired a total of 61 features: 7 points (6 RNFL sectoral data points plus 1 global metric) from structural data and 54 points from functional SAP data. Different machine-learning classifiers, such as Bayesian network, are applied to the concatenated data. Unlike the simple concatenation of raw structural and functional data used as input features in Yousefi *et al.*,²¹ the features in this study are combined considering inherent structural-functional regional correspondence. Furthermore, the current study obtains sophisticated FD from both structural and functional data. The authors in Yousefi *et al.*²¹ focused on comparing the longitudinal progression of glaucoma by obtaining differentials of the time-relapsed data. In comparison, our focus in this work has been differentiating between glaucomatous and normal eyes by exploiting the inherent structural-functional relationship. Yousefi *et al.*²¹ have found the correlation coefficients against the discriminating power, thus ranking all 61 features from highest to lowest. They further conclude that retaining the ten best features offers the best AUROC (0.88) for discriminating progressive glaucoma from stable patients. In comparison, the proposed selective feature fusion method in this study retains four corresponding structure-functional sectors based on the highest correlation coefficients that reflect inherent correspondence. This structure-functional correspondence may best exploit the topographic sector-wise relationship of the structural and functional data, unlike the work reported in Yousefi *et al.*²¹

Glaucoma diagnosis and management are both facilitated and complicated by the various structural and functional methods available for ocular evaluation. Obtaining and unifying data and cross-confirmation of structural and functional results can indeed help to improve diagnostic ability and may have an application in detecting progression. In this study, we have developed techniques that can combine retinal nerve fiber layer data and visual field data to one unified classifier. It is relatively simple to use these shape-based techniques in devices that measure the nerve fiber layer. The results in the present and previous studies show that glaucoma diagnosis and progression detection can be improved using these methods. Manufacturers could consider applying these methods to the data and produce output that may benefit the clinical use of these devices. In our future work, patient-specific structure-functional relationship may be exploited for selective feature selection rather than group-wise processing, as has been done in this study. Now that these methods have been implemented and their potential demonstrated, future research will compare them more rigorously using cross-validation methods and distinct samples. Furthermore, for improved processing of real 2D structural image data, we plan to investigate circular-shaped ROIs that may provide better diagnostic capability for glaucoma detection.

References

1. Weinreb, R. N. and Khaw, P. T., Primary open angle glaucoma, *Lancet*, 363, 1711-1720 (2004).
2. Garway-Heath, D. F., Caprioli, J., Fitzke, F. W. and Hitchings, R. A., Scaling the hill of vision: the physiological relationship between light sensitivity and ganglion cell numbers, *Invest Ophthalmol Vis Sci.*, Vol. 41, pp. 1774-1782, (2000).
3. Quigley, H. A., Miller, N. R. and George, T., Clinical evaluation of nerve fiber layer atrophy as an indicator of glaucomatous optic nerve damage, *Arch Ophthalmol*, 98, 1564-1571 (1980).
4. Quigley, H. A. and Addicks, E. M., Quantitative studies of retinal nerve fiber layer defects," *Arch Ophthalmol*, 100, 807-814 (1982).
5. Lauande-Pimentel, R., Carvalho, R. A., Oliveira, H. C., Gonçalves, D. C., Silva, L. M., and Costa, V. P., Discrimination between normal and glaucomatous eyes with visual field and scanning laser polarimetry measurements, *Br. J. Ophthalmol*. 85, 586-591, (2001).
6. Dersu, I. and Wiggins, M. N., Understanding Visual Fields, Part II; Humphrey Visual Fields, *J. of Ophthalmic Medical Technology*, 2(3), (2006).
7. Hood, D. and Kardon, R. H., A framework for comparing structural and functional measures of glaucomatous damage," *Prog Retin Eye Res.*, 26(6), 688-710 Nov. (2007).
8. Hood, D., Anderson, S. C., Wall, M., Randy, H. and Kardon, R. H., Structure versus Function in Glaucoma: An Application of a Linear Model, *Invest. Ophthalmol. Vis. Sci.*, 48(8), 3662-3668 Aug. (2007).
9. Harwerth, R. S., Wheat, J. L., Fredette, M. J., Anderson, D. R., Linking structure and function in glaucoma, *Prog Retin Eye Res.*, 29(4), 249-71 (2010).
10. Drasdo, N., Mortlock, K. E., North, R. V., Ganglion cell loss and dysfunction: relationship to perimetric sensitivity, *Optom Vis Sci.* 85(11), 1036-1042 (2008).
11. Malik, R., Swanson, W. H., Garway-Heath, D. F., Structure-function relationship' in glaucoma: past thinking and current concepts, *Clin Experiment Ophthalmol*, 40(4), 369-80 (2012).
12. Garway-Heath, D. F., Holder, G. E., Fitzke, F. W., and Hitchings, R. A., Relationship between electrophysiological, psychophysical, and anatomical measurements in glaucoma. *Invest Ophthalmol Vis Sci.*, 43(7), 2213-20. (2002).
13. Reus, N. J. and Lemij, H. G., The relationship between standard automated perimetry and GDx VCC measurements, *Invest Ophthalmol Vis Sci.* 45(3), 840-5 (2004)
14. Sherman, J. Slotnick, S. and Boneta, J., Discordance between structure and function in glaucoma: Possible anatomical explanations, *Optometry*, 80, 487-501 (2009).
15. Horn, F. K., Mardin, C. Y., Laemmer, R., Baleanu, D., Juenemann, A. M., Kruse, F. E. and Tornow, R. P., Correlation between Local Glaucomatous Visual Field Defects and Loss of Nerve Fiber Layer Thickness Measured with Polarimetry and Spectral Domain OCT, *Invest Ophthalmol Vis Sci.*, 50(5), 1971-1977, May. (2009).
16. Strouthidis, N. G., Vinciotti, V., Tucker, A. J., Gardiner, S. K., Crabb, D. P., and Garway-Heath, D. F., Structure and Function in Glaucoma: The Relationship between a Functional Visual Field Map and an Anatomic Retinal Map, *Invest. Ophthalmol. Vis. Sci.*, Vol. 47(12), pp. 5356-5362, Dec., (2006).
17. Danesh-Meyer, H. V., Ku, J. Y. F., Papchenko, T. L., Jayasundera, T., Hsiang, J. C. and Gamble, G. D., Regional Correlation of Structure and Function in Glaucoma, Using the Disc Damage Likelihood Scale, Heidelberg Retina Tomograph, and Visual Fields, *Ophthalmology*, 113(4), 603-611, Apr. (2006).
18. Shah, N. N., Bowd, C., Medeiros, F. A., Weinreb, R. N., Sample, P. A., Hoffmann, E. M. and Zangwill, L. M., Combining Structural and Functional Testing for Detection of Glaucoma, *Ophthalmology*, 113, 1593-1602 (2006).
19. Horn, F. K., Mardin, C. Y., Bendschneider, D., Jünemann, A. G., Adler, W., and Tornow, R. P., Frequency doubling technique perimetry and spectral domain optical coherence tomography in patients with early glaucoma, *Eye (Lond)*. 25(1), pp. 17-29 (2011).

20. Bizios, D., Heijl, A., and Bengtsson, B., Integration and fusion of standard automated perimetry and optical coherence tomography data for improved automated glaucoma diagnostics, *BMC Ophthalmology*, 11(20) (2011).
21. Yousefi, S., Goldbaum, M. H., Balasubramanian, M., Jung, T. P., Weinreb, R. N., Medeiros, F. A., Zangwill, L. M., Liebmann, J. M., Girkin, C. A. and Bowd, C., Glaucoma Progression Detection Using Structural Retinal Nerve Fiber Layer Measurements and Functional Visual Field Points, *IEEE Trans. On Biomedical Engineering*, 61(4), 1143-1154 (2014)
22. Kim, P. Y., Iftekharuddin, K. M., Davey, P. G., Tóth, M., Garas, A., Holló, G. and Essock, E. A., Novel Fractal Feature-Based Multiclass Glaucoma Detection and Progression Prediction, *IEEE Jour. of Biomedical and Health Informatics*, 17(2), 269-276 (2013)
23. Essock, E. A., Zheng, Y. and Gunvant, P., Analysis of GDx-VCC Polarimetry Data by Wavelet-Fourier Analysis across Glaucoma Stages, *Invest Ophthalmol Vis Sci*, 46(8) Aug. (2005).
24. Essock, E. A., Sinai, M. J., Fechtner, R. D., Srinivasan, N. and Bryant, F. D., Fourier Analysis of nerve fiber layer measurements from scanning laser polarimetry in glaucoma: emphasizing shape characteristics of the 'doublehump' pattern, *J Glaucoma* 9, 444-452 (2000).
25. Ferreras, A., Pablo, L. E., Garway-Heath, D. F., Fogagnolo, P., and Garcia-Feijoo, J., Mapping Standard Automated Perimetry to the Peripapillary Retinal Nerve Fiber Layer in Glaucoma, *Invest. Ophthalmol. Vis. Sci.*, Vol. 49 (7), pp. 3018-3025, Jul., (2008).
26. Holló, G, Naghizadeh, F., Evaluation of Octopus Polar Trend Analysis for detection of glaucomatous progression, *Eur J Ophthalmol* (2014), DOI: 10.5301/ejo.5000504.
27. Ahmed, S. and Iftekharuddin, K. M., Discrimination of medulloblastoma and low grade astrocytoma PF tumors using selected MR image features, *MemBis 2008*, (2008).
28. Zook, J. M. and Iftekharuddin, K. M., Statistical analysis of fractal-based brain tumor detection algorithms, *Magnetic Resonance Imaging*, 23, 671-678 (2005).
29. EyeSuite Application Note, Follow up from HFA with Octopus <https://www.haag-streit.com/haag-streit-diagnostics/products/perimetry/> accessed 08/08/2016



An imaged-based inverse finite element method to determine *in-vivo* mechanical properties of the human trabecular meshwork

Anup D. Pant¹, Larry Kagemann^{2,3,*}, Joel S. Schuman³, Ian A. Sigal⁴, Rouzbeh Amini¹

¹Department of Biomedical Engineering, The University of Akron, Akron, OH, USA; ²Lead Reviewer and Biomedical Engineer, Division of Ophthalmic and ENT Devices, Office of Device Evaluation, Center for Devices and Radiological Health, Food and Drug Administration, Silver Spring, MD, USA; ³Department of Ophthalmology, NYU School of Medicine and Langone Medical Center, New York, NY, USA; ⁴Department of Ophthalmology, The University of Pittsburgh, Pittsburgh, PA, USA

Abstract

Aim: Previous studies have shown that the trabecular meshwork (TM) is mechanically stiffer in glaucomatous eyes as compared to normal eyes. It is believed that elevated TM stiffness increases resistance to the aqueous humor outflow, producing increased intraocular pressure (IOP). It would be advantageous to measure TM mechanical properties *in vivo*, as these properties are believed to play an important role in the pathophysiology of glaucoma and could be useful for identifying potential risk factors. The purpose of this study was to develop a method to estimate *in-vivo* TM mechanical properties using clinically available exams and computer simulations.

Design: Inverse finite element simulation

Methods: A finite element model of the TM was constructed from optical coherence tomography (OCT) images of a healthy volunteer before and during IOP elevation. An axisymmetric model of the TM was then constructed. Images of the TM at a baseline IOP level of 11, and elevated level of 23 mmHg were treated as the undeformed and deformed configurations, respectively. An inverse modeling technique was subsequently used to estimate the TM shear modulus (G). An optimization technique was

*Dr. Kagemann's contributions are independent of his work with the FDA. The data and opinions expressed herein do not represent those of any regulatory agency.

Correspondence: Rouzbeh Amini, Olson Research Center Room 301F, 260 S Forge St., Akron, Ohio 44325, USA.

E-mail: ramini@uakron.edu

used to find the shear modulus that minimized the difference between Schlemm's canal area in the *in-vivo* images and simulations.

Results: Upon completion of inverse finite element modeling, the simulated area of the Schlemm's canal changed from 8,889 μm^2 to 2,088 μm^2 , similar to the experimentally measured areal change of the canal (from 8,889 μm^2 to 2,100 μm^2). The calculated value of shear modulus was found to be 1.93 kPa, (implying an approximate Young's modulus of 5.75 kPa), which is consistent with previous *ex-vivo* measurements.

Conclusion: The combined imaging and computational simulation technique provides a unique approach to calculate the mechanical properties of the TM *in vivo* without any surgical intervention. Quantification of such mechanical properties will help us examine the mechanistic role of TM biomechanics in the regulation of IOP in healthy and glaucomatous eyes.

Keywords: Inverse algorithm, glaucoma, intraocular pressure (IOP), Schlemm's canal, trabecular meshwork

1. Introduction

Glaucoma is a major health concern and a leading cause of blindness, affecting more than 3 million people in the US and 63 million people worldwide.^{1,2} Globally, the number of glaucomatous bilateral blindness cases is expected to exceed 11 million by 2020;³ it has been estimated that, by 2040, 111.8 million people will have glaucoma worldwide.¹ Glaucoma is the cause of blindness for 120,000 people in the US, accounting for 9–12% of all cases of blindness.^{3,4} Elevated intraocular pressure (IOP), a risk factor for glaucoma, could be caused by increased resistance to the outflow of aqueous humor. Aqueous humor exits the anterior eye through two pathways: the trabecular meshwork (TM) pathway, accounting for ~60% of the outflow, and the uveoscleral pathway.⁵ The TM pathway begins at the apex of the iridocorneal angle. It continues through the trabecular tissue, across the inner wall of Schlemm's canal, into the canal's lumen, and into the collector channels. This pathway ultimately leads the aqueous humor to the episcleral venous circulation.⁶ IOP increases with respect to normal conditions both if the resistance to aqueous outflow or the aqueous production rate increases.

The TM comprises three different layers: the innermost portion of the TM (the iridic and uveal areas), the central corneoscleral part (which lies between the cornea and scleral spur), and the outermost juxtacanalicular (JXT) part or cribriform layer (which lies between the corneoscleral layer and the inner wall of Schlemm's canal).⁷ Different studies have attributed the outermost JXT layer as the site of the outflow resistance.^{8,9} The endothelial cells contained in the JXT tissue outer region lines the inner wall of Schlemm's canal, an oval shaped structure that collects aqueous humor.

The extracellular matrix (ECM) of the various layers of the TM consists of a number of components such as collagen fibrils, elastic fibers, microfibril, and sheath-derived materials along with basement membrane proteins, type IV collagen, laminin, proteoglycans, and glycosaminoglycans.¹⁰ In glaucomatous eyes, significant changes in the components comprising the ECM and in TM cells have been identified. Three examples of such changes in the TM at the cellular/ECM level are listed below:

1. Primary open-angle glaucoma (POAG) is associated with an excessive accumulation of sheath-derived plaques in the TM in comparison to the normal eye.¹¹
2. In steroid-induced glaucoma, the accumulation of the extra cellular materials has shown to be present; however, unlike POAG, the material was found to be in a fingerprint-like morphology that resembled basement membranes throughout all layers of the TM.¹²
3. In pigmentary glaucoma, TM cell loss has been found to be prominent.^{13,14} In addition to the trabecular cells loss, Gottanka *et al.* found other distinctive changes including trabecular lamellae fusion, collapse of the intertrabecular space, increase in extracellular material, and canal obliteration in eyes suffering from pigmentary glaucoma.¹³

It is also noteworthy that the cellularity of the TM decreases with age, a known risk factor for glaucoma.^{15,16} These changes in the TM at the cellular/ECM level may affect its tissue-level mechanical properties. Since tissue-level mechanical properties are parameters that can be quantified using standard bench-top methods, they are a good candidate for comparative studies between normal and glaucomatous tissues. In particular, previous studies have attributed the stiffness of the TM as an indicator for glaucoma. For instance, Last *et al.*¹⁷ found TM stiffness to be considerably higher in POAG eyes compared to that of normal eyes. They hypothesized that the underlying cause for the higher stiffness value in glaucomatous eyes, *i.e.*, the TM changes at the cellular/ECM level, contributed to the decreased permeability of the TM to the aqueous humor outflow. Similarly, Russel *et al.*¹⁸ observed that glaucomatous TM cells were significantly stiffer than those in a normal TM.

The above studies clearly show an important correlation between glaucoma and increased TM stiffness. All these studies, however, are limited in application, as they have been conducted using isolated tissue samples. Specifically, previous studies in other tissues have shown that mechanical loading and calculated mechanical properties could be significantly different in the *in-vivo* and *ex-vivo* environments.¹⁹ In addition, using *ex-vivo* samples significantly limits the applicability of the measurement as a diagnostic tool in the future. To bridge this knowledge gap, we propose a new method to determine the mechanical properties of the TM *in vivo* without the need for any surgical intervention by employing computer simulations and clinically available non-invasive TM imaging techniques.

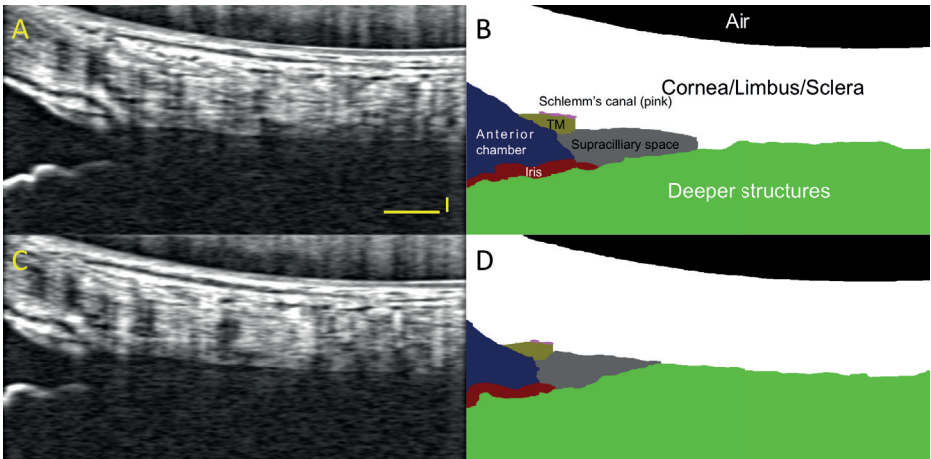


Fig 1. (A) B-scan and (B) segmented images of the TM at baseline IOP, and (C) B-scan and (D) segmented images of the TM at elevated IOP. Scale bars are 250 μm (horizontal and vertical scale bars are of different length as the scans have a different aspect ratio).

2. Methods

2.1. Imaging and segmentation

The temporal limbus of a healthy subject (female, age 26 years) was imaged using optical coherence tomography (OCT, Cirrus, Zeiss, Dublin, CA) at baseline and during IOP elevation. IOP was elevated using an ophthalmodynamometer (Bailliart ophthalmodynamometer, W. Koch Optik, Zurich, Switzerland) applying a 10-g force to the sclera. IOP was also measured at baseline and during IOP elevation by Goldmann applanation tonometry. The tip of the ophthalmodynamometer was placed temporal to the cornea, midway between the limbus and lateral canthus. A team of three researchers, one operating the OCT or Goldmann applanation tonometer, one applying pressure to the sclera, and one assisting the patient with head placement in the headrest, was used. The corresponding locations on the Schlemm's canal were identified in radial OCT cross-sectional B-scans based on the pattern of the limbal vessel crossings.²⁰ The images were segmented manually using the GNU Image Manipulation Program (GIMP 2.8.14) into air, cornea/limbus/sclera complex, Schlemm's canal, TM, anterior chamber, iris, supraciliary space, and "deeper structures" (those beyond the limit of penetration of the OCT scan) (Fig. 1).

2.2. Governing equation

An axisymmetric model of the TM was constructed, similar to our previous finite element models of the anterior eye.²¹⁻²⁴ The TM was modeled as a neo-Hookean solid material. The governing stress balance equation is given by:

$$\nabla \cdot \boldsymbol{\sigma} = 0 \quad (1)$$

where $\boldsymbol{\sigma}$ represented the Cauchy stress tensor:

$$\boldsymbol{\sigma} = \frac{G}{\det \mathbf{F}} (\mathbf{B} - \mathbf{I}) + \frac{2G\nu}{(1-2\nu)\det \mathbf{F}} \ln(\det \mathbf{F}) \mathbf{I} \quad (2)$$

where G was the shear modulus, ν was the Poisson's ratio, \mathbf{I} was the identity tensor, \mathbf{F} was the deformation gradient tensor, and \mathbf{B} was the left Cauchy–Green deformation tensor. The tensors \mathbf{F} and \mathbf{B} were defined as:

$$\mathbf{F} = \frac{d\mathbf{x}}{d\mathbf{X}} \quad (3)$$

$$\mathbf{B} = \mathbf{F}\mathbf{F}^T, \quad (4)$$

where \mathbf{x} was the current position of a material point and \mathbf{X} was its resting position.

2.3. Meshing

The finite element meshes were generated based on TM geometry segmented from *in-vivo* images according to the following steps:

1. The segmented TM images with the appropriate aspect ratio (Fig. 2A) were imported in SolidWorks (Dassault Systèmes, Velizy-Villacoublay, France) and the boundaries of the TM section were manually tracked and obtained (Fig. 2B).
2. The SolidWorks output file was then imported into Abaqus (Dassault Systèmes, Velizy-Villacoublay, France) and meshed using a paving approach (Fig. 2C).
3. As Abaqus was capable of generating only 8-node quadrilateral elements, the output of the Abaqus mesh was subsequently imported into an internally developed C code, which was used to add an extra node to the elements to generate 9-node bi-quadratic quadrilateral finite elements.

The 9-node bi-quadratic quadrilateral elements were subsequently used in our internally developed inverse finite element code, as described in the next section.

2.4. Inverse finite element modeling

A pressure boundary condition with the constant value of IOP was applied along the boundary elements of the TM domain facing the iridocorneal angle (shown by solid arrows in Fig. 3C). The pressure boundary condition was applied to mimic the changes in the IOP *in-vivo*. In particular, since the IOP of the undeformed configuration was 11 mmHg and the IOP of the deformed configuration was 23 mmHg, the difference of 12 mmHg was applied as the pressure boundary condition. The TM boundaries that connect it to the much stiffer surrounding tissues (Fig. 3C) were

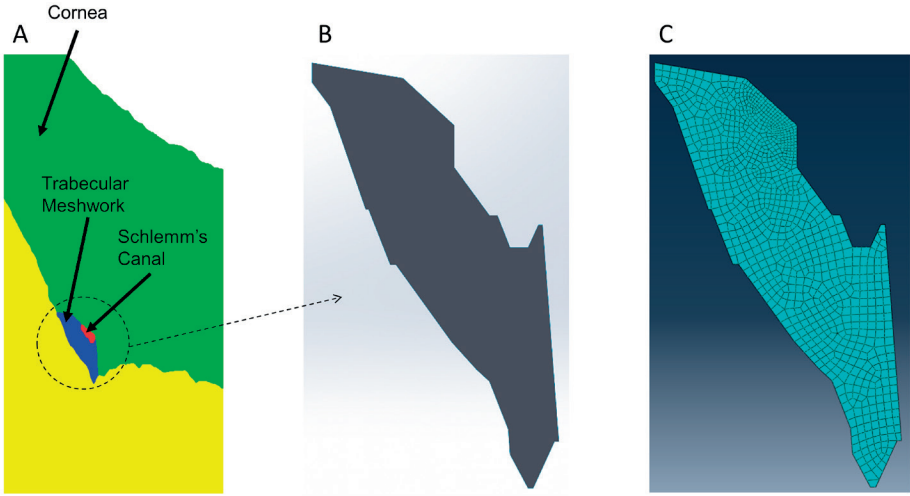


Fig 2. (A) A segmented image of the TM. (B) TM image imported to SolidWorks (Dassault Systèmes, Velizy-Villacoublay, France) to generate the coordinates of the TM boundaries. (C) Finite element meshes generated using Abaqus (Dassault Systèmes, Velizy-Villacoublay, France).

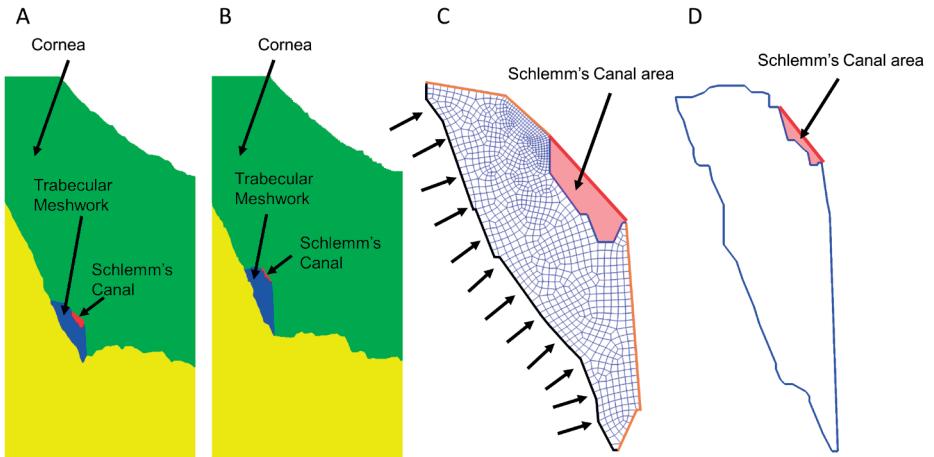


Fig 3. Segmented images of the trabecular meshwork in (A) undeformed and (B) deformed configuration. Finite element mesh and boundary of the trabecular meshwork in (C) undeformed and in (D) deformed configuration, respectively. The boundary of the deformed configuration is provided only for identifying the Schlemm's canal area. In (C) the orange lines represent the fixed boundary condition, whereas the black edge represents the region where the pressure was applied.

assumed to have negligible deformation in comparison to the rest of the tissue. Thus, a fixed boundary condition was chosen for these regions. An additional contact stress, σ_{contact} , was applied along the boundary of Schlemm's canal to prevent tissue penetration into the stiffer scleral tissue:

$$\sigma_{\text{contact}} = A e^{\frac{d}{E}} \mathbf{n} \otimes \mathbf{n} \quad (5)$$

where d is the shortest distance between the TM and the sclera, A and E are adjustable coefficients, \mathbf{n} is the normal vector to the boundary, and \otimes is the dyadic operator.

We then used an inverse modeling approach²⁵ to calculate the shear modulus G from the experimental deformation data using a differential algorithm. The material was assumed to be nearly incompressible, so a Poisson's ratio (ν) of 0.49 was used. The basic overview of the process is given in the flowchart shown in Figure 4. The objective function was defined as absolute value of the difference between the Schlemm's canal area of the experimental measurements SC_{exp} (the shaded area in Fig. 3D) and the genetically driven finite element solution SC_{sim} (the shaded area in Fig. 3C after the deformation is applied):

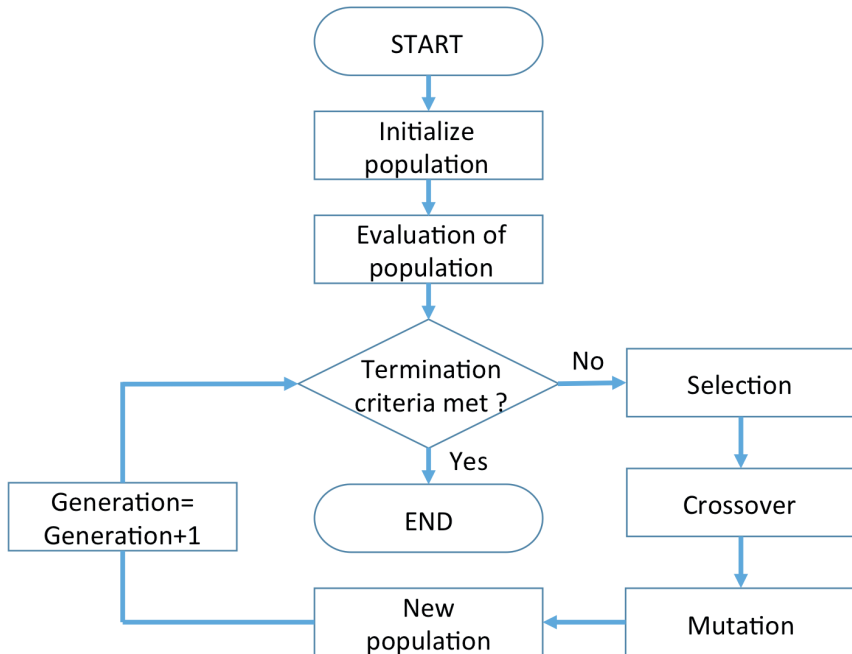


Fig 4. Inverse algorithm flowchart.

$$\text{Error} = |\text{SC}_{\text{exp}} - \text{SC}_{\text{sim}}| \quad (6)$$

The initial guesses for G were chosen between 10 kPa and 90 kPa. The simulations were performed using an HP Intel Xeon machine at the Ohio Supercomputer Center (Columbus, OH, USA).²⁶ The inverse algorithm ran for 50 generations to ensure the convergence of the solution.

3. Results

From the optimization technique, a value of 1.93 kPa was obtained for the TM shear modulus, G . The simulated area of the Schlemm's canal was found to be $\sim 2,088 \mu\text{m}^2$ (the area of the undeformed configuration was $\sim 8,889 \mu\text{m}^2$) whereas the area of the experimental image was found to be $\sim 2,100 \mu\text{m}^2$. Figure 5 shows the simulated result of TM using a shear modulus of 1.93 kPa (a) without and (b) with the application of a contact force. The optimization convergence was independent of our initial guesses, and the broader ranges of initial guesses only increased the computational time. On average, the solution process took approximately 300 minutes (for 50 generations, the number of iterations for optimizing G).

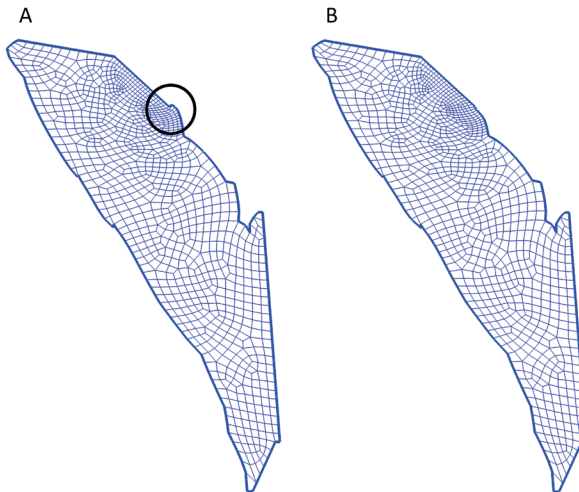


Fig 5. Simulated results of the deformation of the TM (A) without the application of contact force (the marked circle denotes the penetration of the TM into the stiffer scleral tissue) and (B) with the application of contact force.

4. Discussion

The best estimation of compressive Young's modulus of elasticity (E) was obtained in a study by Last *et al.*, with an atomic force microscopy measurement of dissected TM tissues.¹⁸ They found that TM tissue from a non-glaucomatous donor eye had a modulus of elasticity of approximately 4 kPa. In our study in a living eye, we found a shear modulus value of 1.93 kPa, which is approximately equivalent to an elastic modulus of 5.75 kPa. Similarly, the use of the additional contact force did not have a dramatic effect on the optimized value of the shear modulus, and G was found to be 2.0 kPa (~4% different from 1.93 kPa) when the contact force was not applied. Our measurement in the living eye was only slightly larger than that of excised tissues.

Using simplified beam theory, Johnson *et al.* estimated the TM elastic modulus to be 128 kPa (approximately equivalent to a shear modulus value of 43 kPa), which is substantially higher than our estimated value.²⁷ The simplified geometry and material models used in the study of Johnson and colleagues could have contributed to the different outcomes: we used a nearly incompressible neo-Hookean solid as our material model, whereas they employed a linear elastic material model. In addition, we did not simplify the TM deformation to a beam bending model. Camras *et al.*, using uniaxial stretching experiments, found the circumferential elastic modulus of a normal TM to be 51.5 ± 13.6 MPa²⁸ and that of a glaucomatous TM to be 17.5 ± 5.8 MPa.¹⁵ Clearly, the reported modulus values in the literature span a large spectrum, with a difference of nearly three orders of magnitude. One reason for such discrepancy could be the way of measuring the stiffness. Camras *et al.* measured the axial stiffness using larger tissue strips, whereas Last *et al.* only measured the local compressive stiffness on a cellular level. It is noteworthy that, none of these *ex-vivo* methods accurately encompass the mechanical response of the TM *in vivo*. In this study, we attempted to capture the *in-vivo* response of the TM at a tissue level. Another reason could be the difference between cadaveric eyes used in the conventional testing methods and our measurements *in vivo*. Nonetheless, more research is needed to increase the number of experimental fittings both in multiple levels of IOP measurements and among additional volunteers using our technique. Using a wider range of samples will help us discern the interplay of the mechanical properties of the TM and regulation of IOP in healthy and glaucomatous eyes. More detailed studies to identify the differences between the TM of normal and glaucoma subjects by testing a sufficient number of cases so as to allow a suitable statistical analysis are necessary.

In the realm of biomechanics, most soft tissues are treated as incompressible (or nearly incompressible) materials since they consist largely of water.²⁹ However, when there is a fluid motion within the tissue, more complex constitutive models, involving mixture or poroelasticity theory, are available to account for the fluid-solid interaction.³⁰⁻³² Implementation of such complex models in the inverse finite element analysis of TM deformation requires more than one fitting parameter.

Increasing the number of fitting parameters could jeopardize the uniqueness of the solution. As such, in the current study, we opted to use a more generalized nearly incompressible model to simulate the deformation of the TM, and we employed only the shear modulus as our fitting parameter. We have previously used smaller values of Poisson's ratio as an indicator of compressibility in the simulation of iris deformation.²⁴ In our future studies, we aim to perform parametric studies using our finite element model and examine the influence of TM compressibility on the calculated value of the shear modulus. In addition, inverse finite element modeling using both the shear modulus and Poisson's ratio as the fitting parameters can be performed, if necessary.

In inverse modeling of complex geometries, the choice of objective functions can affect the quality of the fitting process.³³ In our study, the Schlemm's canal boundary was detected with a high level of confidence. As such, the experimental errors due to segmentation were minimized with the choice of Schlemm's canal area as the objective function. In addition, changes in the Schlemm's canal area corresponded to lateral deformation of the TM. Segmentation of the TM from the surrounding tissues is not as trivial; consequently, change in the cross-sectional area of the TM was not used as an objective function in our current study. If future advances in medical imaging provide more reliable methods for detecting the boundary between the TM and the surrounding tissues, the fidelity of Schlemm's canal as the objective function in comparison to the other possible alternatives should be examined.

5. Conclusion

Our proposed technique provides a new approach to quantify the mechanical properties of the TM *in vivo* by using only clinical imaging and computer simulations without the need for any surgical intervention. Our technique could provide a framework for the development of future diagnostic techniques to detect glaucoma at its earlier stages and for assessment of treatment methods that could bring TM stiffness to its normal values.

Acknowledgement

We would like to acknowledge the Ohio Supercomputer Center (Columbus, OH, USA) for the resource grant to facilitate the computational aspect of our study. This project was supported in part by grants EY023966, EY025011, and EY013178 from the National Institutes of Health, USA.

References

1. Tham Y, Li X, Wong TY, Quigley HA, Aung T, Cheng C. Global Prevalence of Glaucoma and Projections of Glaucoma Burden through 2040: A Systematic Review and Meta-Analysis. *Ophthalmology* 2014;121(11):2081-2090. Available from: <http://linkinghub.elsevier.com/retrieve/pii/S0161642014004333> doi: 10.1016/j.ophtha.2014.05.013.
2. Grant WM, Burke JF. Why do some people go blind from glaucoma. *Ophthalmology* 1982;89(9):991-998. Available from: <http://linkinghub.elsevier.com/retrieve/pii/S0161642082346758> doi: 10.1016/S0161-6420(82)34675-8.
3. Quigley HA, Broman AT. The number of people with glaucoma worldwide in 2010 and 2020. *Br J Ophthalmol* 2006;90(3):262-267. Available from: <http://bjo.bmj.com/cgi/doi/10.1136/bjo.2005.081224> doi: 10.1136/bjo.2005.081224.
4. Congdon N, O'Colmain B, Klaver CC, Klein R, Munoz B, Friedman DS, et al. Causes and prevalence of visual impairment among adults in the United States. *Arch Ophthalmol* 2004;122(4):477-485. Available from: <http://archophth.jamanetwork.com/article.aspx?doi=10.1001/archophth.122.4.477> doi: 10.1001/archophth.122.4.477.
5. Alm A, Nilsson SF. Uveoscleral outflow—a review. *Exp Eye Res* 2009;88(4):760-768. Available from: <http://linkinghub.elsevier.com/retrieve/pii/S0014483508004351> doi: 10.1016/j.exer.2008.12.012.
6. Kaufman PL, Adler FH, Levin LA, Alm A. *Adler's Physiology of the Eye*. New York: Elsevier Health Sciences; 2011.
7. Kahook MY, Schuman JS, Epstein DL. *Chandler and Grant's Glaucoma*. Thorofare, N.J. SLACK Incorporated; 2013.
8. Rohen J, Witmer R. Electron microscopic studies on the trabecular meshwork in glaucoma simplex. *Albrecht von Graefes Archiv für klinische und experimentelle Ophthalmologie* 1972;183(4):251-266. Available from: <http://link.springer.com/10.1007/BF00496153> doi: 10.1007/BF00496153.
9. Mäepea O, Bill A. The pressures in the episcleral veins, Schlemm's canal and the trabecular meshwork in monkeys: effects of changes in intraocular pressure. *Exp Eye Res* 1989;49(4):645-663. Available from: <http://linkinghub.elsevier.com/retrieve/pii/S0014483589006000> doi: 10.1016/S0014-4835(89)80060-0.
10. Acott TS, Kelley MJ. Extracellular matrix in the trabecular meshwork. *Experimental Eye Research* 2008;86(4):543-561. Available from: <http://linkinghub.elsevier.com/retrieve/pii/S0014483508000171> doi: 10.1016/j.exer.2008.01.013.
11. Gottanka J, Johnson DH, Martus P, Lütjen-Drecoll E. Severity of optic nerve damage in eyes with POAG is correlated with changes in the trabecular meshwork. *J Glaucoma* 1997;6(2):123-132.
12. Johnson D, Flügel C, Hoffmann F, Futa R, Lütjen-Drecoll E. Ultrastructural changes in the trabecular meshwork of human eyes treated with corticosteroids. *Arch Ophthalmol* 1997;115(3):375-383. Available from: <http://archophth.jamanetwork.com/article.aspx?doi=10.1001/archophth.1997.01100150377011> doi: 10.1001/archophth.1997.01100150377011. [Google Scholar]
13. Gottanka J, Johnson DH, Grehn F, Lütjen-Drecoll E. Histologic findings in pigment dispersion syndrome and pigmentary glaucoma. *J Glaucoma* 2006;15(2):142-151. Available from: <http://content.wkhealth.com/linkback/openurl?sid=WKPTLP:landingpage&an=00061198-200604000-00011> doi: 10.1097/00061198-200604000-00011. [Google Scholar]
14. Murphy CG, Johnson M, Alvarado JA. Juxtacanalicular tissue in pigmentary and primary open angle glaucoma the hydrodynamic role of pigment and other constituents. *Arch Ophthalmol* 1992;110(12):1779-1785. Available from: <http://archophth.jamanetwork.com/article.aspx?doi=10.1001/archophth.1992.01080240119043> doi: 10.1001/archophth.1992.01080240119043.
15. Camras LJ, Stamer WD, Epstein D, Gonzalez P, Yuan F. Circumferential tensile stiffness of glaucomatous trabecular meshwork. *Invest Ophthalmol Vis Sci* 2014;55(2):814-823. Available from: <http://iovs.arvojournals.org/article.aspx?doi=10.1167/iovs.13-13091> doi: 10.1167/iovs.13-13091.
16. Alvarado J, Murphy C, Polansky J, Juster R. Age-related changes in trabecular meshwork cellularity. *Invest Ophthalmol Vis Sci* 1981;21(5):714-727.

17. Last JA, Pan T, Ding Y, Reilly CM, Keller K, Acott TS, et al. Elastic modulus determination of normal and glaucomatous human trabecular meshwork. *Invest Ophthalmol Vis Sci* 2011;52(5):2147-2152. Available from: <http://iovs.arvojournals.org/article.aspx?doi=10.1167/iovs.10-6342> doi: 10.1167/iovs.10-6342.
18. Russell P, Last J, Ding Y, Pan T, Acott T, Keller K, et al. Compliance and the human trabecular meshwork: implications about glaucoma. *Invest Ophthalmol Vis Sci* 2010;51(13):3205-3205.
19. Brouwer I, Ustin J, Bentley L, Sherman A, Dhruv N, Tendick . Measuring in vivo animal soft tissue properties for haptic modeling in surgical. *Medicine meets virtual reality*.;2001:69-74.
20. Kagemann L, Wang B, Wollstein G, Ishikawa H, Nevins JE, Nadler Z, et al. IOP elevation reduces Schlemm's canal cross-sectional area. *Invest Ophthalmol Vis Sci* 2014;55(3):1805-1809. Available from: <http://iovs.arvojournals.org/article.aspx?doi=10.1167/iovs.13-13264> doi: 10.1167/iovs.13-13264.
21. Amini R, Whitcomb JE, Al-Qaisi MK, Akkin T, Jouzdani S, Dorairaj S, et al. The posterior location of the dilator muscle induces anterior iris bowing during dilation, even in the absence of pupillary block. *Invest Ophthalmol Vis Sci* 2012;53(3):1188-1194. Available from: <http://iovs.arvojournals.org/article.aspx?doi=10.1167/iovs.11-8408> doi: 10.1167/iovs.11-8408.
22. Amini R, Jouzdani S, Barocas VH. Increased iris–lens contact following spontaneous blinking: Mathematical modeling. *Journal of Biomechanics* 2012;45(13):2293-2296. Available from: <http://linking-hub.elsevier.com/retrieve/pii/S0021929012003508> doi: 10.1016/j.jbiomech.2012.06.018.
23. Amini R, Barocas VH. Reverse pupillary block slows iris contour recovery from corneoscleral indentation. *J Biomech Eng* 2010;132(7):71010. Available from: <http://Biomechanical.asmedigitalcollection.asme.org/article.aspx?articleid=1429231> doi: 10.1115/1.4001256.
24. Jouzdani S, Amini R, Barocas VH. Contribution of different anatomical and physiologic factors to iris contour and anterior chamber angle changes during pupil dilation: theoretical analysis. *Invest Ophthalmol Vis Sci* 2013;54(4):2977-2984. Available from: <http://iovs.arvojournals.org/article.aspx?doi=10.1167/iovs.12-10748> doi: 10.1167/iovs.12-10748.
25. Storn R, Price K. Differential evolution—a simple and efficient heuristic for global optimization over continuous spaces. *J Global Optimiz* 1997;11(4):341-359.
26. Ohio Supercomputer Center. Oakley supercomputer (Columbus, OH). 2012.
27. Johnson M, Schuman JS, Kagemann L. Trabecular meshwork stiffness in the living human eye. *Invest Ophthalmol Vis Sci* 2015;56(7):3541-3541.
28. Camras LJ, Stamer WD, Epstein D, Gonzalez P, Yuan F. Effects of trabecular meshwork stiffness on outflow. *Invest Ophthalmol Vis Sci* 2012;53(9):5242-5250. Available from: <http://iovs.arvojournals.org/article.aspx?doi=10.1167/iovs.12-9825> doi: 10.1167/iovs.12-9825.
29. Wang K, Read AT, Sulchek T, Ethier CR. Trabecular meshwork stiffness in glaucoma. *Exp Eye Res*. May 2017;158: 3-12. <https://doi.org/10.1016/j.exer.2016.07.011>
30. Simon B, Kaufmann M, McAfee M, Baldwin A. Finite element models for arterial wall mechanics. *J Biomech Eng-T ASME* 1993;115(4B):489-489. Available from: <http://Biomechanical.asmedigitalcollection.asme.org/article.aspx?articleid=1399604> doi: 10.1115/1.2895529.
31. Soltz MA, Ateshian GA. A conewise linear elasticity mixture model for the analysis of tension-compression nonlinearity in articular cartilage. *J Biomech Eng-T ASME* 2000;122(6):576-586.
32. Powell TA, Amini R, Oltean A, Barnett VA, Dorfman KD, Segal Y, et al. Elasticity of the porcine lens capsule as measured by osmotic swelling. *J Biomech Eng* 2010;132(9):91008. Available from: <http://Biomechanical.asmedigitalcollection.asme.org/article.aspx?articleid=1426860> doi: 10.1115/1.4002024.
33. Nagel TM, Hadi MF, Claeson AA, Nuckley DJ, Barocas VH. Combining displacement field and grip force information to determine mechanical properties of planar tissue with complicated geometry. *J Biomech Eng* 2014;136(11):114501. Available from: <http://biomechanical.asmedigitalcollection.asme.org/article.aspx?doi=10.1115/1.4028193> doi: 10.1115/1.4028193.



Journal for Modeling in Ophthalmology

Focus and Scope

While the rapid advance of imaging technologies in ophthalmology is making available a continually increasing number of data, the interpretation of such data is still very challenging and this hinders the advance in the understanding of ocular diseases and their treatment. Interdisciplinary approaches encompassing ophthalmology, physiology, mathematics and engineering have shown great capabilities in data analysis and interpretation for advancing basic and applied clinical sciences.

The Journal for Modeling in Ophthalmology (JMO) was created in 2014 with the aim of providing a forum for interdisciplinary approaches integrating mathematical and computational modeling techniques to address open problems in ophthalmology. JMO welcomes articles that use modeling techniques to investigate questions related to the anatomy, physiology and function of the eye in health and disease.



www.modeling-ophthalmology.com

Published by Kugler Publications

www.kuglerpublications.com